Search for Dark Matter in Association with Top Quarks with the CMS Detector

---

Dissertation

zur

Erlangung der naturwissenschaftlichen Doktorwürde
(Dr. sc. nat.)

vorgelegt der

Mathematisch-naturwissenschaftlichen Fakultät

der

Universität Zürich

von

Deborah Pinna

aus

Italien

Promotionskomitee

Prof. Dr. Florencia Canelli (Vorsitz und Leitung der Dissertation)

Prof. Dr. Benjamin Kilminster

Prof. Dr. Thomas Gehrmann

Prof. Dr. Marc Schumann

Zürich, 2017

Abstract

The evidence of the existence of dark matter is provided by astrophysical observations at different scales. Nevertheless, information about its nature or non gravitational interactions is not yet available. Assuming interactions between dark matter and standard model particles, dark matter can be produced in high energy collisions and the interaction studied in detail.

In this thesis, a search for dark matter produced in association with a top quark pair is performed using the data recorded by the CMS detector at two different center-of-mass energies of 8 and 13 TeV. The datasets correspond to integrated luminosities of 19.7 fb^{-1} and 2.2 fb^{-1}, respectively. The analysis performed at 8 TeV considers only the single-lepton decay of top quark pairs. It represented the first search of its kind in CMS and the results provide important insight on possible scalar interactions between dark matter and standard model particles. The results are interpreted using a dedicated effective field theory. Similar search is performed using the data collected in 2015 at a center of mass energy of 13 TeV. This work contains important improvements, as for example the increase of signal acceptance by considering in addition the final state where both top quarks decay hadronically. The higher energies reached by the LHC in the run started in 2015 reduce the region of validity for the effective field theory interpretation and simplified models are used instead to interpret the results. In both analyses, the observed data is compared with the predicted standard model background, showing good agreement with the expectation.

The same simplified model also predicts processes in which the dark matter particles are produced in association with a single top quark. The prospects of an increased sensitivity for dark matter scalar interactions due to this processes is firstly developed as part of this thesis.

The associated production of dark matter particle with top quarks has been firstly investigated with the data collected by the CMS detector in this thesis. The results have been interpreted employing the latest theoretical descriptions of dark matter interactions. While, no evidence of the production of dark matter matter in proton-proton collisions have been found, important constraints have been set on the property of this mysterious component of the universe. New prospects to improve the dark matter discovery potential in interactions with top quark couplings have also been presented.

Zusammenfassung

Astrophysikalische Beobachtungen auf verschiedenen Skalen beweisen die Existenz dunkler Materie in unserem Universum. Allerdings sind bislang keine weiteren Informationen über ihren Ursprung oder ihre nicht gravitationsbedingten Wechselwirkungen verfügbar. Unter der Annahme von Wechselwirkungen zwischen dunkler Materie und Teilchen aus dem Standardmodell könnte diese bei hochenergetischen Kollisionen in einem Teilchenbeschleuniger erzeugt und im Detail untersucht werden.

In dieser Doktorarbeit wird die mögliche Produktion von dunkler Materie in Begleitung eines Top Quark Paares erforscht, indem die Daten des CMS Detektors bei Schwerpunktsenergien von 8 TeV und 13 TeV und den entsprechenden integrierten Luminositäten von 19.7 fb^{-1} und 2.2 fb^{-1} analysiert werden. In der ersten Analyse wird hauptsächlich der semileptonische Zerfallskanal des Top Quark Paares untersucht, bei welchem ein Top Quark leptonisch und das andere hadronisch zerfällt. Diese Analyse war die erste ihrer Art in CMS und erlaubt einen ersten Blick auf die mögliche skalare Wechselwirkung zwischen dunkler Materie und Teilchen des Standardmodells. Die Resultate werden mithilfe eines effektiven Feldtheorieansatzes interpretiert. Eine ähnliche Analyse wurde ebenfalls mit den in 2015 gesammelten Daten bei einer Schwerpunktsenergie von 13 TeV durchgeführt. Dieses mal werden jedoch weitere Zerfallskanäle, bei dem beide Top Quarks hadronisch zerfallen, mit einbezogen. Da durch die höhere Schwerpunktsenergie die Gültigkeit der effektiven Feldtheorie eingeschränkt ist, werden vereinfachte Modelle benutzt um die Resultate zu interpretieren. In beiden Analysen werden die Daten mit den Erwartungen des Standardmodells verglichen, wobei eine gute Übereinstimmung mit der Vorhersage zu beobachten ist.

Das vereinfachte Modell, welches in der Analyse die Produktion von dunkler Materie mit einem Top Quark Paar beschreibt, sagt zusätzliche Prozesse voraus, in welchen die dunkle Materie in Verbindung mit einem einzelnen Top Quark erzeugt wird. Diese neuen Prozesse erhöhen die Empfindlichkeit von Beschleuniger basierten Experimenten bezüglich skalarer Wechselwirkungen von dunkler Materie und werden im Detail in dieser Arbeit ebenfalls untersucht.

Contents

Chapter 1

Introduction

One of the fundamental open questions in particle physics is related to the nature of dark matter (DM) and its interactions. Proof of the existence of this component is provided by observations at various astronomical scales [1–3], which are based on the gravitational interactions of DM. Cosmological analyses have also measured the abundance of DM to be 26% of the mass of the universe [4], which is five times that of visible matter. Nevertheless, cosmological and astrophysical observations do not provide information about the nature of DM, but they still provide constraints on its properties. For example, DM particles are expected to not have electromagnetic nor strong interactions, and their lifetime is required to be on the same scale of the age of the universe (10^{17} seconds) to explain their current presence.

The standard model (SM) [5–8] is a gauge theory able to describe accurately almost all the known experimental observations in particle physics with high precision. The SM has also predicted particles that where then discovered in high energy experiments (ex. the W, Z bosons, the top quark and recently the Brout-Englert-Higgs boson). Despite the accuracy of the SM and its predicting power, it is believed to be an approximation at lower energies of a more general theory. In fact, some phenomena are not naturally embedded in this theoretical framework. In particular, the SM does not provide any feasible DM candidate or a description of the gravitational force. Experimental tests of the SM are then made to validate the theory at higher energies or to have information about new physics that can be observed by deviations from predictions.

The Large Hadron Collider (LHC) [9] has been built at the European Organization for Nuclear Research near Geneva. It is designed for proton-proton collisions at a center of mass energy of 14 TeV and an instantaneous luminosity of 10^{34} s^{-1} cm^{-2}. The Compact Muon Solenoid (CMS) [10] is a general purpose detector located in one of the several interaction points of LHC. CMS aims at answering fundamental open questions in particle physics, such as the nature of DM.

If interactions between DM and SM particles take place, DM particles can be produced in proton-proton collisions and their interactions studied in detail. This type of event is rather challenging because the DM does not interact with the detector components. At hadron colliders, the presence of DM particle is therefore inferred as missing momentum balanced by a visible particle that is produced in association with the DM.

A search for a pair of top quarks produced in association with two DM particles is presented in this thesis. Using a dataset of 19.7 fb^{-1} collected by the CMS detector during the year 2012, the analysis is performed in final states with one lepton from the decay of the top quarks. This search has been performed for the first time in CMS and the results have been published in JHEP [11]. A similar analysis was performed with a dataset of 2.2 fb^{-1} collected during 2015. This analysis included also the final state with no leptons from the top quarks decay. This channel added more signal event candidates resulting in an increased sensitivity of about 40% with respect to the single-lepton channel only. Publication of this result is expected in early 2017 [12].

The thesis presenting the search for DM produced in association with a top quark pair is organized as follow. In Chapter 2 the cosmological and astrophysical proof of the existence of DM is presented together with the measurement of its actual abundance. The SM is also introduced and possible DM candidates are discussed. In the same chapter, the experiments searching for non-gravitational interactions of DM particles are explained.

Chapters 3 and 4 focus on the experimental framework, introducing the LHC accelerator and the CMS experiment. In addition, the reconstruction and identification techniques employed for the particles used in this work are presented.

The analysis strategy and the variables used to distinguish DM events from SM processes are described in Chapter 5. The selection is based on the background and DM expected signatures, which are also described. The techniques used to improve the background predictions are included in this Section, as well as the sources of uncertainties considered in the analysis.

In Chapter 6, the statistical techniques to extract confidence limits for different DM particle hypotheses are introduced. The obtained results are found to be consistent with the SM expectation. Therefore, the findings are interpreted in terms of upper limits on the DM production cross section. For such interpretation the models used to describe the associated production of DM particles with a pair of top quarks are described in detail. The interpretation of the analysis of the 8 TeV data is based on an Effective Field Theory (EFT), while the 13 TeV analysis relies on the use of a simplified model. Both approaches will be described in Section 6.3. The motivation for the discussed analysis is also introduced, showing that the discovery potential for interactions mediated by a spin-0 particle, one of the possibilities assumed, improves when the DM couples to top quarks.

In Chapter 7 are discussed additional processes, so far neglected, that should be considered in the future in order to improve the discovery reach for DM production at the LHC. The thesis concludes in Chapter 8 with a short summary.

Chapter 2

The dark matter mystery

One of the main goals of the LHC is to answer fundamental open questions in particle physics such as the nature of dark matter (DM). The data collected from proton-proton (*pp*) collisions at the LHC are essential on shedding light on its nature.

Evidence of the existence of DM in our universe as well as the relative amount of DM in the universe is presented in Section 2.1.

The Standard Model (SM) of particle physics is a theory that describes the basic components of matter and their interactions, a brief introduction is included in Section 2.2. A more detailed and formal approach can be found in [13], whereas here only a short overview of the concepts used in this work is presented. So far no large deviations from the SM framework have been observed. Nevertheless, this theoretical model has some limitations, as discussed later in Section 6.3.1. For example it does not provide particle candidates explaining the observational evidence for DM, Section 2.3.

From the measurements bringing evidence of the existence of DM and its abundance, no information about its properties or non gravitational interactions is provided. Our limited knowledge of DM suggests that if DM is a particle it should interact at most weakly with SM particles. If these interactions take place, DM particles should be produced in *pp* collisions at the LHC, Section 2.4. This chapter includes descriptions of the different approaches currently used to find DM particles, such as direct, indirect, and colliders searches.

2.1 Observational evidence for dark matter

2.1.1 Dynamic in gravitational potential

At cosmological scales, the first indication of the existence of DM is from Zwicky's measurements of the dispersion velocity of galaxies in the Coma cluster [1]. From such measurements, the gravitational potential in the cluster is inferred using the virial theorem that relates the kinetic energy of the system to its total potential energy. The resulting mass of the galaxy cluster is two orders of magnitude larger than what is expected from its luminosity. This implies the existence of non-luminous (dark) matter. In fact, if the only source of gravitational force comes from the luminous matter then the measured orbital velocities are too high to hold galaxies together inside the cluster.

The existence of DM was confirmed by subsequent measurements of stars and gas circular velocities within a galaxy. From Newtonian dynamics the velocity $v(r)$ of these objects is expected to behave as:

$$v(r) = \sqrt{\frac{GM(r)}{r}} \tag{2.1}$$

where G is the Newton's constant and $M(r)$ the visible mass of the galaxy within a radius r. The rotational velocity is therefore expected to behave as $1/\sqrt{r}$ while moving away from the galactic center, where the majority of the visible mass is concentrated. In contrast to such expectations, Ford and Rubin found that the rotational velocity remains constant up to considerably large radii [2]. The simpler explanation for such behaviour is the presence of a non-luminous matter halo in which the galaxy is embedded. From this observation, the distribution of DM in the galaxy is also inferred. From Equation 2.1, if $v \approx \textit{constant}$ then $M(r) \propto r$ implying that the DM distribution in the outer part of the galaxy has to be spherical. The same reasoning cannot be applied close to the galactic center because the star density is too high to allow velocity measurements.

Similar behaviours have been observed from the rotational curves of other galaxies, such as NGC 6503 [14], as shown in Fig. 2.1.

2.1.2 Gravitational lensing and the bullet cluster

Light emitted from distant objects is bended or focused by the matter intervening between the source and the observer. As a consequence, a single brighter image or

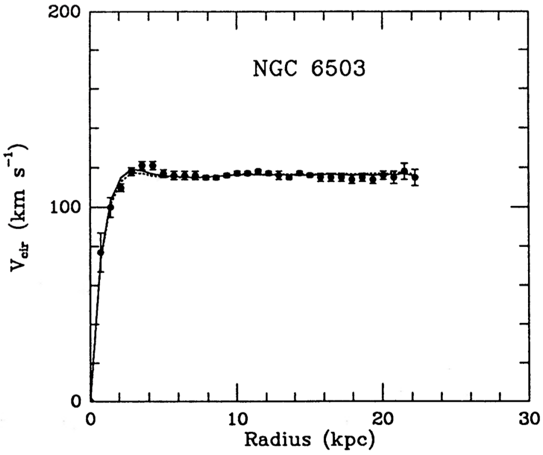

Figure 2.1: NGC 6503 galaxy rotation curve. The observed circular velocity is presented as a function of radial distance from the galactic center. The rotation curves of visible component (dashed) and gas (dotted) are also shown. A third component, a dark halo (dash-dot), is necessary to reconcile the difference between expectations and data [14].

multiple images of the light source are observed [15]. Measurements of this effect, known as gravitational lensing, confirm the presence of non-luminous matter in galaxies and in clusters of galaxies [16]. In Figure 2.2 is shown an image of the 1E 0657-56 galaxy cluster obtained with lensing and X-ray techniques.

During the merging of the two clusters, the galaxies are minimally affected and behave as collisionless particles. In Figure 2.2, the galaxies are shown in orange and white as obtained by optical images.

On the contrary, the intracluster hot gas experiences ram pressure during the cluster merging and as a result is distributed toward the center of the system after the collision. This distribution is shown in Figure 2.2 by the pink clumps as obtained from X-rays measurements.

From lensing measurements the highest mass density regions are inferred and are shown by the blue regions in Figure 2.2. The highest concentration of mass in the system would coincide with the hot gas distribution if the cluster is formed by visible matter only. The observed separation, with respect to the hot gas distribution, is therefore explained by the presence of collisionless DM. This result indicates the existence of DM without assumptions on the description of the gravitational force law [3].

2.1.3 The Cosmic Microwave Background

The measurements presented so far provide evidence of the existence of DM but no information on its total amount in the universe. This quantity is obtained from the

Figure 2.2: This composite image shows the galaxy cluster 1E 0657-56, also known as the "bullet cluster". This cluster was formed after the collision of two large clusters of galaxies, the most energetic event known in the universe since the Big Bang. In the image, the baryonic matter is shown by the pink clumps and the distribution of dark matter by the blue shading as deduced from gravitational lensing [17].

analysis of the Cosmic Microwave Background (CMB) [18, 19]. In the recombination epoch [20], when neutral hadrons are formed, the photons become free to propagate through the universe (photon decoupling). This happens when the energy scale of the universe is of the order of 1 eV. The CMB is the radiation left from the decoupled photons in the early universe.

The CMB has an almost perfectly uniform temperature $T \simeq 2.72$ K, except for local fluctuations of the order of 10^{-5} K. This is shown from the observations of the Plank collaboration presented in Figure 2.3. As an example, at small scales the fluctuations are attributed to photons and protons behaving as a photon-baryon fluid before the recombination epoch. The gravitational force compresses the fluid, causing at the same time an increase of its pressure. A subsequent expansion starts when the effect of the pressure wins over the gravitational force. In the expansion process, the pressure decreases and the gravitational force takes over compressing again the fluid. Depending on the processes taking place in the fluid portion, the decoupled photons will emerge with different temperatures [22].

Studying these temperature anisotropies allows an estimation of cosmological parameters such as the DM abundance. The observed anisotropies are expressed in terms of spherical harmonics when projected in a bi-dimensional spherical surface sky:

$$\frac{\delta T}{T}(\theta, \phi) = \sum_{l=2}^{+\infty} \sum_{m=-l}^{+l} a_{lm} Y_{lm}(\theta, \phi)$$

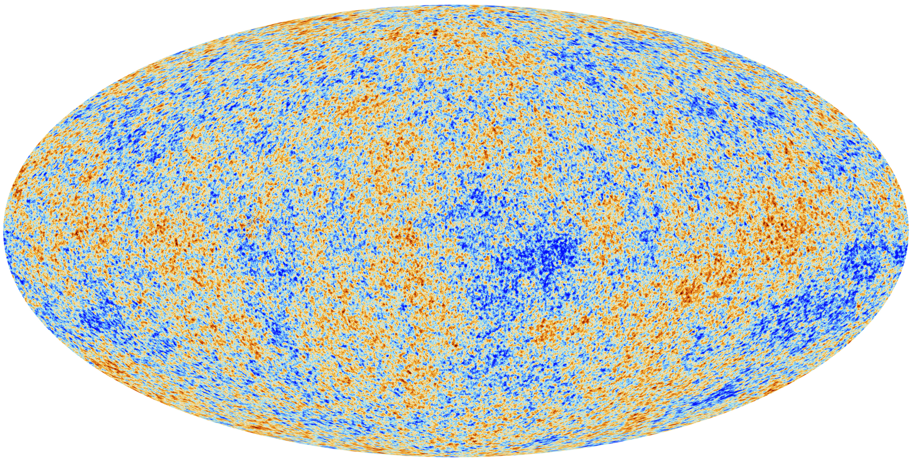

Figure 2.3: The CMB anisotropies as observed by the Planck collaboration. The CMB is an image of the remnant light from the photon decoupling. The observed temperature varies from -300μK (blue color) to $+300\mu$K (red color) [21].

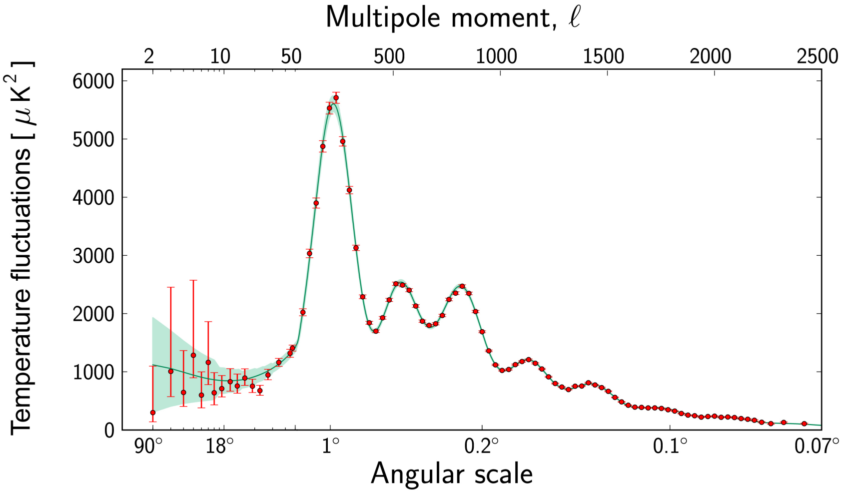

Figure 2.4: The CMB temperature fluctuations are measured by the Plank collaboration at different angular scales on the sky. The multipole moments corresponding to the various angular scales are indicated at the top of the graph. The red dots correspond to measurements made with the Planck satellite and the error bars account for measurement errors. The green curve shown in the graph represents the best fit of the standard model of cosmology to the Planck data. The pale green area around the curve shows the predictions of all the variations of the standard model that best agree with the data [23].

where θ and ϕ are the angular coordinates, a_{lm} the multipole moments and l the multipole order. Under the common assumption that the temperature fluctuations are Gaussian, the harmonic coefficients a_{lm} have zero mean value and variance C_l:

$$C_l \equiv \left\langle |a_{lm}|^2 \right\rangle \equiv \frac{1}{2l+1} \sum_{m=-l}^{+l} |a_{lm}|^2$$

that corresponds to the power spectrum. Measurements are usually presented in terms of the function $l(l+1)C_l/2\pi$ for various l values, as shown in Figure 2.4. A fit to the spectrum is used to constrain the parameters of the standard model of cosmology, which is the most widely accepted theory of the formation of the universe. The information about the total energy density, the baryonic and dark matter abundances are therefore determined as results of the fit.

The total DM and baryonic (b) densities, Ωh^2, are measured from Plank to be [4]:

$$\Omega_b h^2 = 0.02226 \pm 0.00023 \qquad \Omega_{DM} h^2 = 0.1186 \pm 0.0020$$

where $h = H_0/100$ and H_0 is the Hubble constant [24]. These values translate in about 25.8% DM and 4.8% baryonic matter in the universe. The remaining 69.4% of the energy content comes from dark energy [24].

2.2 Introduction to the standard model

The standard model (SM) [5–8] is a gauge theory based on the $SU(3)_C \otimes SU(2)_L \otimes U(1)_Y$ symmetry group, which describes interactions between elementary particles through the strong ($SU(3)_C$) and electroweak forces ($SU(2)_L \otimes U(1)_Y$). In the symmetry group the colour charge, weak isospin and the hypercharge are identified with C, L and Y, respectively.

Fermions are the elementary matter components and the fundamental forces are described via the exchange of the bosonic gauge field mediator. Each fermion and boson has its own antiparticles with the same mass but opposite charge flavour.

Fermions follow the Fermi-Dirac statistics and have half-integer spins. They are divided in two categories depending whether they carry colour charge: leptons (colourless) and quarks (colour charged). Both groups are divided in three generations as shown in Table 2.1. The first lepton generation consists of the electron (e) and the electron neutrino (ν_e). The second and third generations include the muon (μ) and the tau

Generation	Particle	Charge (e)	Mass	Interaction
1^{st}	e	-1	$0.5109989461 \pm 0.0000000031$ MeV	EM, Weak
	ν_e	0	–	Weak
2^{nd}	μ	-1	$105.6583745 \pm 0.0000024$ MeV	EM, Weak
	ν_μ	0	–	Weak
3^{rd}	τ	-1	1776.86 ± 0.12 MeV	EM, Weak
	ν_τ	0	–	Weak
1^{st}	u	$+2/3$	$2.2^{+0.6}_{-0.4}$ MeV	EM, Weak, Strong
	d	$-1/3$	$4.7^{+0.5}_{-0.4}$ MeV	EM, Weak, Strong
2^{nd}	c	$+2/3$	1.27 ± 0.03 GeV	EM, Weak, Strong
	s	$-1/3$	96^{+8}_{-4} MeV	EM, Weak, Strong
3^{rd}	t	$+2/3$	$173.21 \pm 0.51 \pm 0.71$ GeV	EM, Weak, Strong
	b	$-1/3$	$4.18^{+0.04}_{-0.03}$ GeV	EM, Weak, Strong

Table 2.1: Fermion three generations subdivision with charge and mass specified. The interactions to which each particle participate are also listed (electromagnetic (EM)). Mass values are taken from [24].

(τ) as well as their corresponding neutrinos (ν_μ, ν_τ). The neutrinos are assumed to be massless within the SM. Each quark generation is composed of an up-type and a down-type quark with electric charge $+2e/3$ and $-e/3$ respectively, where e is the elementary electron charge. The first generation consists of the up (u) and down (d) quarks, while the second of charm (c) and strange (s) quarks. The last generation gather top (t) and bottom (b) quarks.

The fermion mass increases with the generation, as shown in Table 2.1, while the lifetime in general decreases. The c and b quarks provide an exception to this trend, having the b quark a longer lifetime with respect to the c quarks. This is an important feature used to distinguish c and b quarks in high energy experiments.

Fermion are further divided in left (L) and right (R) chirality states depending on whether they transform under $SU(2)_L$ as doublet or singlets, respectively:

$$\begin{array}{cccccc} \begin{pmatrix} \nu_e \\ e \end{pmatrix}_L & \begin{pmatrix} \nu_\mu \\ \mu \end{pmatrix}_L & \begin{pmatrix} \nu_\tau \\ \tau \end{pmatrix}_L & \begin{pmatrix} u \\ d' \end{pmatrix}_L & \begin{pmatrix} c \\ s' \end{pmatrix}_L & \begin{pmatrix} t \\ b' \end{pmatrix}_L \\ e_R & \mu_R & \tau_R & u_R & c_R & t_R \\ & & & d_R & s_R & b_R \end{array} \tag{2.2}$$

where b', d' and s' are weak eigenstates. Their corresponding mass eigenstates are given by:

$$\begin{pmatrix} d' \\ s' \\ b' \end{pmatrix} = V_{CKM} \begin{pmatrix} d \\ s \\ b \end{pmatrix} \tag{2.3}$$

where V_{CKM} is the Cabibbo-Kobayashi-Maskawa (CKM) matrix [25, 26],

$$V_{CKM} = \begin{pmatrix} V_{ud} & V_{us} & V_{ub} \\ V_{cd} & V_{cs} & V_{cb} \\ V_{td} & V_{ts} & V_{tb} \end{pmatrix} = \begin{pmatrix} 0.974 & 0.225 & 0.004 \\ 0.225 & 0.973 & 0.041 \\ 0.009 & 0.040 & 0.999 \end{pmatrix} \tag{2.4}$$

The CKM matrix shows that transitions between fermions of different generations are strongly suppressed. On the contrary, the diagonal elements corresponding to transitions in the same generation are close to one. For example, the top quark decays to b quark and a W boson with a corresponding matrix element of 0.999.

Fermions are described by Dirac spinors ψ in the Minkowski space-time $x^\mu \equiv (t, \boldsymbol{x})$ and the Lagrangian density $\mathcal{L}_D$ describing a non-interacting Dirac fermion is given by:

$$\mathcal{L}_D = \bar{\psi}\left(i\gamma^\mu \partial_\mu - m\right)\psi, \tag{2.5}$$

where γ^μ are the Dirac γ-matrices, $\bar{\psi} = \gamma^0\psi$ is the conjugate field and m is the fermion mass.

Gauge bosons have an integer spin and follow the Bose-Einstein statistics. Each interaction described in the SM is mediated by a spin-1 boson that couples to a specific charge as summarized in Table 2.2. The photon (γ) mediates the electromagnetic force, has a null electromagnetic charge and is massless. All charged fermions are subject to the electromagnetic force. The Z and $W^\pm$ bosons are the mediators of the weak force and they couple to weak charge. Differently from the previous boson are not massless. Mass terms for gauge bosons cannot be included in the SM Lagrangian because they do not respect the local gauge invariance. In the SM, the particles acquire mass through the Brout-Englert-Higgs mechanism [27–29]. In this formalism, an associated massive boson is also predicted, the so-called Brout-Englert-Higgs boson, which was recently discovered by the ATLAS and the CMS collaborations [30, 31]. The electromagnetic and weak interactions are included in a single electroweak theory with symmetry group $SU(2)_L \otimes U(1)_Y$. The mediators of the strong force are eight massless gluons (g) and the charge of the interaction is the "colour". Each gluon carries colour-charge itself, allowing interactions among gluons.

If a scalar boson is described by a wave function ϕ the dynamic of the free system is described by the Lagrangian density $\mathcal{L}_{free}$, given by:

$$\mathcal{L}_{free} = \frac{1}{2}\partial_\mu\phi\partial^\mu\phi - \frac{1}{2}m^2\phi^2$$

Symmetry	Interaction	Mediator	Mass (GeV)
$SU(2)_L \otimes U(1)_Y$	electromagnetic	γ	–
	weak	Z	91.1876 ± 0.0021
		W$^{\pm}$	80.385 ± 0.015
$SU(3)_C$	strong	g	–

Table 2.2: Fundamental forces described by the SM and their corresponding bosonic gauge field mediators. Mass values are taken from [24].

where the first term refers to the kinetic energy of the particle and in the second term m is the particle mass.

If a scalar field interacts with a Dirac fermion, their interaction is described by the following Lagrangian density $\mathcal{L}$:

$$\mathcal{L} = \frac{1}{2}\partial_\mu\phi\partial^\mu\phi - \frac{1}{2}m^2\phi^2 + \bar{\psi}\left(i\gamma^\mu\partial_\mu - m\right)\psi - \lambda\phi\bar{\psi}\psi$$

where the coefficient λ is the coupling constant.

If the fermion interact instead with a pseudo-scalar field A, the Lagrangian density takes the form:

$$\mathcal{L} = \frac{1}{2}\partial_\mu A\partial^\mu A - \frac{1}{2}m^2A^2 + \bar{\psi}\left(i\gamma^\mu\partial_\mu - m\right)\psi - i\lambda A\bar{\psi}\gamma^5\psi$$

The Lagrangian densities for free scalar (pseudo-scalar) fields, Dirac fermions and for their interaction are important concepts used in the description of the DM models used in this work, Section 6.3.2.

Limitations of the Standard Model

Despite the accuracy of the SM description of particle physics phenomena up to 0.1% [32], there are different reasons to believe that the Standard Model is an approximation at lower energies of a more general theory.

For example, the SM is not able to explained the observed matter-antimatter asymmetry, i.e the actual negligible amount of antimatter in the universe. Another unanswered question is the hierarchy problem regarding the difference between the Brout-Englert-Higgs boson mass $\mathcal{O}(10^2)$ GeV and the Plank scale $\mathcal{O}(10^{19})$ GeV [33]. In addition, the theory describes only $\sim 4\%$ of the universe, explanations for DM are not provided. Moreover, the gravitational force cannot be included in the current theoretical framework.

New physics that justifies these shortcomings can be directly or indirectly be observed by deviations from SM predictions. In the first approach, the direct production of particles predicted by theories beyond the SM is investigated. If evidence of these new particles are found direct coupling to the SM sector can estimated. In the indirect approach, hint of new physics might appear as small deviations between precision measurements and SM predictions. This second approach allows to distinguish between possible SM extensions and to derive indirect constraints on their parameters.

2.3 Dark matter candidates

Cosmological and astrophysical observations provide important constraints on the properties of DM. This information allows to understand which particles are feasible DM candidates.

The particles contributing to the measured DM matter density are required to have the following characteristics [24]:

- *stable on cosmological scales*: the DM decay lifetime has to be larger than the age of the universe (10^{17} seconds) to explain its current presence,
- *weak interactions with electromagnetic field*: otherwise DM particles would appear as luminous matter,
- *correct relic density*, the mass of the DM particles must satisfy the DM abundance observed today,
- *non-relativistic at the time of galaxies formation*: if DM is a relativistic particle then larger structure would have formed earlier in the evolution of the universe. Our galaxy appears to be older than the Local Group [34, 35], thus requiring non-relativistic DM.

The SM does not provide any DM candidate that satisfies these properties. For example, most of the SM particles are unstable and therefore cannot contribute to the current DM abundance. The best candidates are the neutrinos due to their stability and null electromagnetic charge. Nevertheless, the most stringent laboratory constraint on the neutrino mass m_ν [35] is:

$$m_\nu < 2.05 \text{ eV}$$

corresponding to a relic density of:

$$\Omega_\nu h^2 \leq 0.07.$$

The neutrino relic density is additionally constrained by the combination of CMB anisotropies and large-scale structure measurements, yielding a tighter limits of $\Omega_\nu h^2 \leq 0.0062$ [24]. In addition, neutrinos are relativistic particles. Therefore, these SM candidates cannot explain the measured DM abundance nor the observed structure of the universe.

The most studied candidate beyond the SM is a Weakly Interacting Massive Particle (WIMP). If it is the sole responsible for the DM abundance, the WIMP has a mass in the range 100 GeV to 1 TeV. In addition, WIMPs are predicted to have weak scale interactions with SM particles, allowing for various experiments described in Section 2.4 to aim to observe it.

The WIMP density parameter is calculated assuming that at the beginning of the universe these particles are produced as thermal relic. In the early universe, WIMPS and SM particles were in thermal equilibrium. The number of WIMP started decreasing as $e^{-m_\chi/T}$ when the universe temperature T dropped below the DM mass m_χ. Nevertheless, the DM abundance did not drop to zero because of the concomitant expansion of the universe. In fact, this process caused a decrease of the rate of annihilation of DM into SM particles. The WIMPs abundance then reached a constant value (freeze out), as explained in more detail in [36]. The expected WIMP relic density can be approximated by [35]:

$$\Omega_\chi h^2 \simeq \frac{3 \cdot 10^{-27} \mathrm{cm}^3 \mathrm{s}^{-1}}{\langle \sigma_A v \rangle}$$

where $\langle \sigma_A v \rangle$ is the thermal averaging of the DM annihilation cross section σ_A and the relative velocity v of the interacting WIMPs. In order to have the correct DM relic density, $\langle \sigma_A v \rangle$ has to be of the order of $3 \cdot 10^{-26} \mathrm{cm}^3 \mathrm{s}^{-1}$, which is extremely similar to the weak interaction cross sections. This value is obtained for DM masses on the weak scale (100 GeV - 1 TeV range). The fact that to account for the current abundance both the WIMP mass and its coupling to SM particles are at the weak scale is referred as WIMP miracle. Possible WIMPs candidates are predicted by many theories beyond the SM, as for example in SUper SYmmetry models [37].

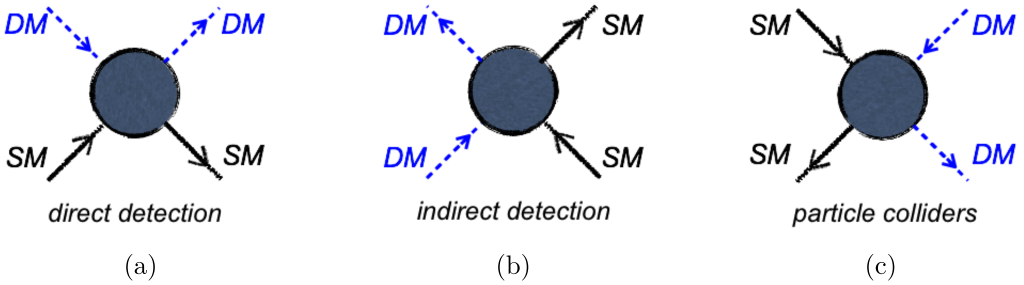

(a) (b) (c)

Figure 2.5: Schematic representation of the three different experimental approaches used to investigate interactions between DM and SM particles. The presented detection strategies are: direct searches investigating nuclear recoils as results of these interaction (a), indirect searches which detect DM annihilation products (b) and collider searches investigating for DM production in high energy collisions (c).

2.4 Dark matter searches

Interactions between DM and SM particles are investigated through different types of searches, represented schematically in Figure 2.5:

- *direct detection*, search for nuclear recoils produced in the elastic scattering of DM particles on nuclei,
- *indirect detection,* aims at detecting stable final SM products (neutrinos, gamma rays, positrons, antiprotons and their antiparticles) from the annihilation of DM particles,
- *particle colliders*, search for DM particles produced in high energy collisions. The DM particles will escape the detector volume without interacting with its components. For this reason, DM signatures at colliders are studied in processes where the DM is produced in association with detectable SM particles.

These different experimental approaches allow an important interplay and complementarity among them in the quest of discovering DM. The general working principles of these classes of experiments are explained in the following sections based on [35,38,39]. More detail can be found in [40,41].

2.4.1 Direct searches for dark matter particles

To account for the measured rotational curves (Section 2.1.1) the DM has to be trapped inside galaxies. Therefore, DM and star velocities with respect to the galactic center are similar.

Typical DM velocities in the solar system are of the order of few hundred kilometers per second. At these velocities, the interaction between DM and SM particles is an elastic scattering with recoil energies in the range $1-100$ KeV for DM masses between 10 GeV and 10 TeV. The expected interaction rate R can be approximated by:

$$R \approx \sum_i N_i \frac{\rho_\chi}{m_\chi} \sigma \langle v \rangle$$

where the sum is extended to the nuclei species i present in the detector, N_i is the number of target nuclei, ρ_χ the DM local density, and m_χ the mass of the DM particle. In the same equation, σ is the interaction cross section and $\langle v \rangle$ the velocity of the DM with respect to the detector. Typical values of $\rho_\chi = 0.3$ GeV/cm^3 and $\langle v \rangle = 230$ km/s yield an expected flux of 10^5cm^{2}s^{-1} for a DM particle of mass 100 GeV. The interaction rate depends on two unknown parameters, which are the mass of the DM particle and the interaction cross section. For this reason, the results from direct detection experiments are expressed in terms of these parameters.

Nuclear recoil from DM particles interactions are a rare process. In fact, the associated cross section is measured to be lower than 10^{-30}cm^{-2}. Furthermore, the energy spectrum of the recoiling nuclei is exponential with a mean value of the order of 50 keV or less. These low rate and energies require experiments to be located underground to reduce contributions from cosmic rays. Additional detector shielding and analysis techniques are employed to reject radiation activity and residual cosmic rays.

Depending on the coupling type, the interaction is classified as spin-independent or spin-dependent. In the former class, the cross section is proportional to the mass of the target nuclei. Therefore, experiments targeting this type of interaction employ heavy nuclei, as for example germanium and xenon. In the latter type of interaction the cross section depends on the nuclear spin factor. The nuclei typically employed are highly polarized, for example fluorine. Examples of spin-independent experiments are CDMS [42], CRESST-II [43], CoGeNT [44], DAMA , LUX [45] and Xenon100 [46]. A selection of spin-dependent experiments are COUPP [47], IceCube [48], PICASSO [49], SIMPLE [50] and Super-K [51]. The current experimental scenarios are shown in Figure 2.6. Positive results are presented together with exclusions from other experiments that do not confirm these DM signals.

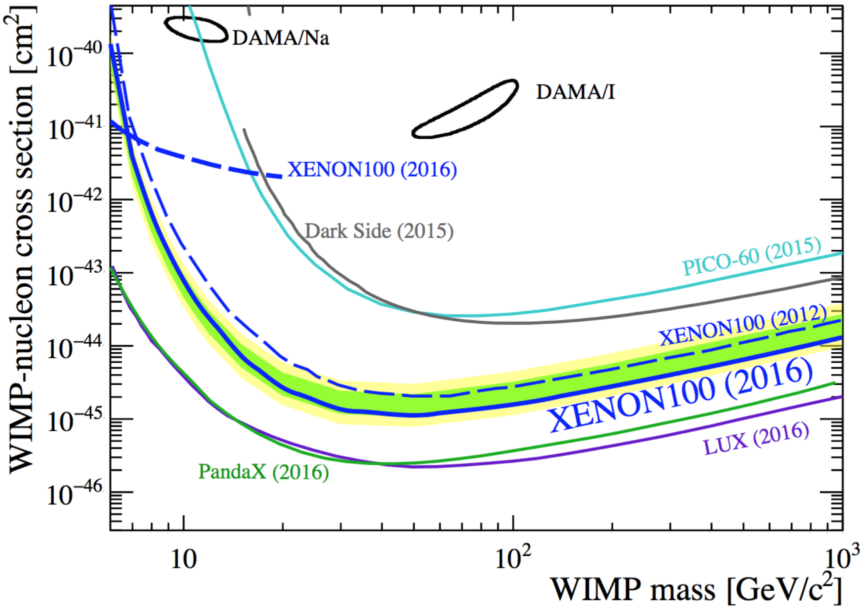

(a)

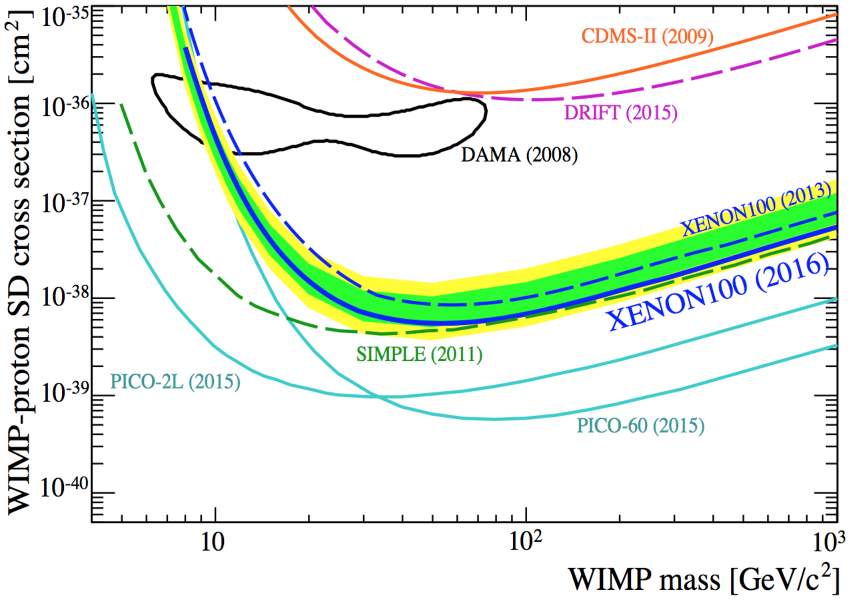

(b)

Figure 2.6: Cross section limits as a function of the DM mass for spin-independent (a) and spin-dependent (b) interactions for various experiments [46].

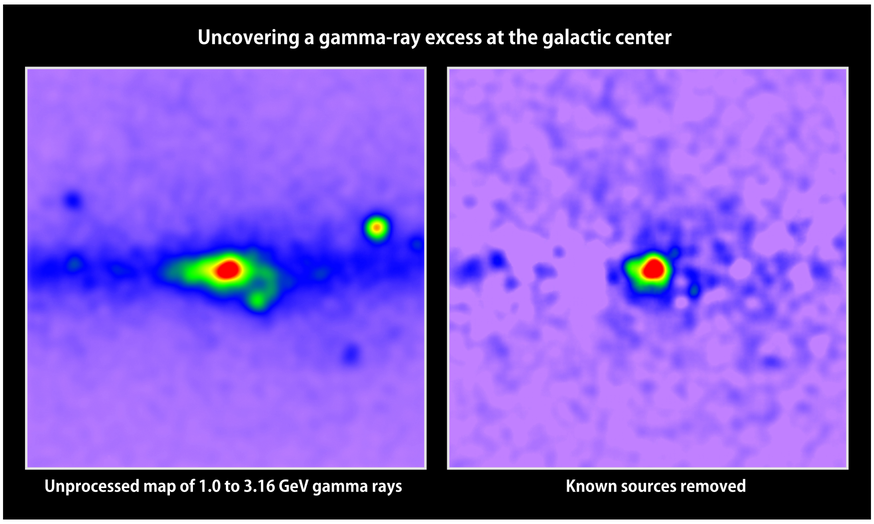

Figure 2.7: Map of gamma rays with energies between 1 and 3.16 GeV detected in the galactic center by Fermi's LAT satellite (left) with the red color indicating higher energies. The same map after removing all known gamma-ray sources shows an excess that might be due to DM annihilations (right) [52].

2.4.2 Indirect searches for dark matter particles

The annihilation products searched by indirect detection experiments include stable SM particles as neutrinos, gamma rays, positrons, and antiprotons. Photons and neutrinos allow to trace back the direction from which they are emitted, providing therefore information about the distribution of DM in the universe. Antiparticles have instead the advantage of a low astrophysical background.

The rate of the annihilation processes is proportional to the DM density. Consequently, larger quantities of annihilation products are expected from galactic centers. Additional high DM density regions are provided by the Sun and the Earth if DM is captured while passing through.

If DM is captured in the Earth center, the particles produced in the annihilation are absorbed before arriving to the Earth surface except for neutrinos. Also DM annihilation in the Sun can produced neutrinos that are then identified through their interaction with Earth. Experiments looking for this type of events are ICeCube and Super-K.

Dwarf spheroidal galaxies are faint objects with observed mass-to-light ratio of about 100, which is an indication of high DM densities. This type of galaxies are therefore an ideal candidate to search for gamma rays from DM annihilation. The Fermi Large Area Telescope (LAT) observed 25 dwarf spheroidal galaxies but no significant excess of gamma rays due to DM was observed [53].

The Fermi LAT collaboration has also observed gamma rays from the center of the Milky Way, where high DM concentrations are also expected. An excess of gamma rays with energies in the from 1 GeV to 3 GeV was observed [54], as shown in Figure 2.7. This result is in agreement with annihilating DM particles of mass in the range $36 - 51$ GeV. More data are necessary to validate this observation and to exclude that this excess is due to pulsar or to an incomplete understanding of the known gamma-ray sources.

Antimatter products from annihilating DM can be detected by satellite experiments such as Fermi LAT [55], PAMELA [56] and AMS [57]. In these experiments, an excess is observed in the positrons flux but not for the antiproton. This would imply that DM particles are "leptophilic". More data are required to interpret correctly the observed excess.

2.4.3 Collider searches for dark matter particles

The search for DM production at the LHC is based on different type of models.

Dark matter can be considered within a complete beyond the SM theory, as for example SUSY. The complexity of these models arise from the large number of parameters to be determined. Having almost no information on the properties of the DM particles, limiting the searches to specific interactions may leave possible signatures uncovered.

Assuming that the DM is the only new particle accessible at collider energies, the interaction between SM and DM particles can be described by effective operators. In this Effective Field Theory (EFT) approach the number of free parameters is minimal, the mass m_χ of the DM particle and the suppression scale M_* of the interaction. The small number of free parameters allows an easier comparison with results from direct and indirect detection experiments.

In the EFT approach, the kinematic of the DM production process depends on the nature assumed for the DM particles and on the Lorentz structure of the interaction. In particular, the DM can be assumed to be a scalar (real or complex) or a fermion (Majorana or Dirac) particle. The interactions is expressed by an EFT Lagrangian L_{int} with the form [11]:

$$L_{int} = C(\bar{\chi}\Gamma^{\chi}\chi)(\bar{q}\Gamma^{q}q)$$

where C is the coupling constant and the operator Γ describes the interaction type between quarks (q) and DM (χ). Considering quark bilinear operators, Γ is a 4×4

Name	Coupling constant	Operator
D1	m_q/M_*^3	$\bar{\chi}\chi\bar{q}q$
D2	im_q/M_*^3	$\bar{\chi}\gamma^5\chi\bar{q}q$
D3	im_q/M_*^3	$\bar{\chi}\chi\bar{q}\gamma^5 q$
D4	m_q/M_*^3	$\bar{\chi}\gamma^5\chi\bar{q}\gamma^5 q$
D5	$1/M_*^2$	$\bar{\chi}\gamma^\mu\chi\bar{q}\gamma_\mu q$
D6	$1/M_*^2$	$\bar{\chi}\gamma^\mu\gamma^5\chi\bar{q}\gamma_\mu q$
D7	$1/M_*^2$	$\bar{\chi}\gamma^\mu\chi\bar{q}\gamma_\mu\gamma^5 q$
D8	$1/M_*^2$	$\bar{\chi}\gamma^\mu\gamma^5\chi\bar{q}\gamma_\mu\gamma^5 q$
D9	$1/M_*^2$	$\bar{\chi}\sigma^{\mu\nu}\chi\bar{q}\sigma_{\mu\nu}q$
D10	i/M_*^2	$\bar{\chi}\sigma_{\mu\nu}\gamma^5\chi\bar{q}\sigma_{\alpha\beta}q$
D11	$\alpha_s/4M_*^3$	$\bar{\chi}\chi G_{\mu\nu}G^{\mu\nu}$
D12	$i\alpha_s/4M_*^3$	$\bar{\chi}\gamma^5\chi G_{\mu\nu}G^{\mu\nu}$
D13	$i\alpha_s/4M_*^3$	$\bar{\chi}\chi G_{\mu\nu}\tilde{G}^{\mu\nu}$
D14	$\alpha_s/4M_*^3$	$\bar{\chi}\gamma^5\chi G_{\mu\nu}\tilde{G}^{\mu\nu}$

(a)

Name	Coupling constant	Operator
M1	$m_q/2M_*^3$	$\bar{\chi}\chi\bar{q}q$
M2	$im_q/2M_*^3$	$\bar{\chi}\gamma^5\chi\bar{q}q$
M3	$im_q/2M_*^3$	$\bar{\chi}\chi\bar{q}\gamma^5 q$
M4	$m_q/2M_*^3$	$\bar{\chi}\gamma^5\chi\bar{q}\gamma^5 q$
M5	$1/2M_*^2$	$\bar{\chi}\gamma^\mu\gamma^5\chi\bar{q}\gamma_\mu q$
M6	$1/2M_*^2$	$\bar{\chi}\gamma^\mu\gamma^5\chi\bar{q}\gamma_\mu\gamma^5 q$
M7	$\alpha_s/8M_*^3$	$\bar{\chi}\chi G_{\mu\nu}G^{\mu\nu}$
M8	$i\alpha_s/8M_*^3$	$\bar{\chi}\gamma^5\chi G_{\mu\nu}G^{\mu\nu}$
M9	$\alpha_s/8M_*^3$	$\bar{\chi}\chi G_{\mu\nu}\tilde{G}^{\mu\nu}$
M10	$i\alpha_s/8M_*^3$	$\bar{\chi}\gamma^5\chi G_{\mu\nu}\tilde{G}^{\mu\nu}$

(b)

Name	Coupling constant	Operator
C1	m_q/M_*^2	$\chi^\dagger\chi\bar{q}q$
C2	im_q/M_*^2	$\chi^\dagger\chi\bar{q}\gamma^5 q$
C3	$1/M_*^2$	$\chi^\dagger\partial_\mu\chi\bar{q}\gamma^5 q$
C4	$1/M_*^2$	$\chi^\dagger\partial_\mu\chi\bar{q}\gamma^5 q$
C5	$\alpha_s/4M_*^2$	$\chi^\dagger\chi G_{\mu\nu}G^{\mu\nu}$
C6	$i\alpha_s/4M_*^2$	$\chi^\dagger\chi G_{\mu\nu}\tilde{G}^{\mu\nu}$
R1	$m_q/2M_*^2$	$\chi^2\chi\bar{q}q$
R2	$im_q/2M_*^2$	$\chi^2\chi\bar{q}\gamma^5 q$
R3	$\alpha_s/8M_*^2$	$\chi^2\chi G_{\mu\nu}G^{\mu\nu}$
R4	$i\alpha_s/8M_*^2$	$\chi^2\chi G_{\mu\nu}\tilde{G}^{\mu\nu}$

(c)

Table 2.3: List of leading operators for the interaction of DM with SM particles. the DM is assumed to be a Dirac (a), Majorana (b), complex scalar (C operators) or real scalar (R operators) (c) [58,59].

matrix of the complete set $\Gamma = \{1, \gamma^5, \gamma^\mu, \gamma^\mu\gamma^5, \sigma^{\mu\nu}\}$, corresponding respectively to scalar, pseudoscalar, vector, axial vector, and tensor interactions. Coupling to $G_{\mu\nu}G_{\alpha\beta}$, where G is a color field strength can also be considered. The complete list of leading operators is given in Table 2.3 [58, 59] for different hypotheses on the DM nature.

While the EFT models are considerably general, they have limitations depending on the momentum transferred in the collision. If the energy is such that the mediator of the interaction between the SM and DM particles is resolved, then the description of the DM production with the EFT approach is no longer valid. Simplified models overcome these limitations while trying to keep at a minimum the number of parameters. The additional free parameters are the characteristics of the mediator (mass, couplings, and width). In addition, different spin hypothesis on the unknown mediator particle are considered, typically spin-1 and spin-0 [60].

At hadron colliders, the presence of DM particles is inferred as missing momentum balanced by visible particles produced in association with the DM. The ATLAS [61] and CMS [10] collaborations, have performed various DM searches generally referred to as mono-X, where the visible particle X includes jets [62–68], vector bosons [69–73], or heavy flavour quarks [11, 12, 74–76].

Investigating different associated production modes allows a complementarity within collider searches. In fact, the same interaction type can be studied in different final states providing limits improvements on the associated parameters. In addition, specific associated production modes are more sensitive than others to a particular interaction. For example, scalar interactions of Dirac DM particles are studied with higher sensitivity in events where the DM couples to top quarks. This is motivated by the proportionality of the scalar couplings, to the mass of the quark involved in the interaction Table 2.3. The same is also valid for scalar simplified models, where the proportionality to the quark mass is maintained assuming that the spin-0 mediator has Yukawa type couplings to the SM sector. A process in which the DM couples directly to top quarks is the associated production of DM particles with a top quark pair. Also the mono-jet search is sensitive to scalar interactions, but couplings to light quarks are suppressed and top quarks enter only at loop level.

The EFT and simplified models approaches are discussed in more detail in Section 6.3, where the results of the analysis are interpreted in terms of DM production cross section.

2.4.4 Complementarity of dark matter searches

The complementarity between the discussed experimental approaches is essential to investigate DM [77]. For example, indirect detection experiments are sensitive to interactions between DM and all SM particles. Instead, in direct searches and at hadron colliders is difficult to investigate DM particles that couple only to leptons [77]. Furthermore, direct searches are sensitive to DM masses above 1 GeV, while this range is extended by the other experimental approaches.

This complementarity is even more important in case of DM discovery. In fact, each approach is limited by systematic uncertainties and a positive signal from one experiments needs to be confirmed by other DM searches before claiming discovery. Furthermore, an excess of events at colliders cannot be directly interpreted as a DM discovery. In fact, it would be possible to infer that the new particle has a lifetime of about 10^{-7} s, necessary to escape the detector. However, this value is much smaller than the lifetime

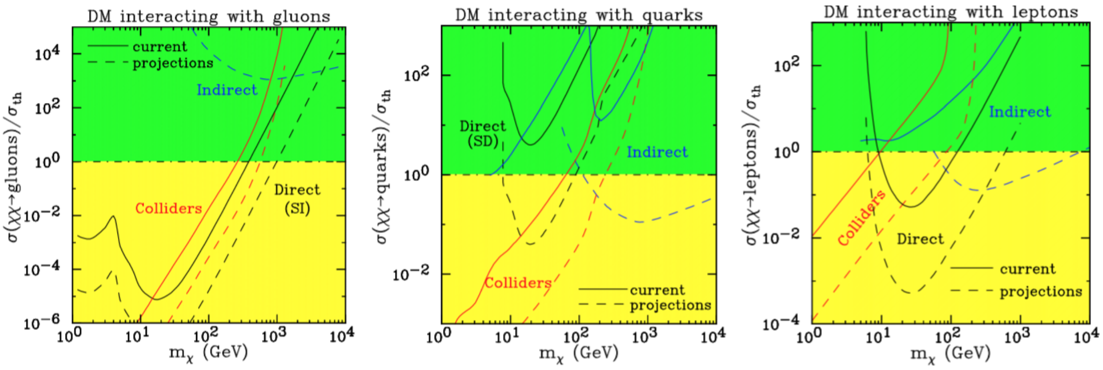

Figure 2.8: Discovery potential and current bounds on the ratio between the annihilation cross section and its theoretical value σ_{th} as a function of the DM mass m_χ. The bounds are presented for direct, indirect, and collider DM searches that are sensitive to interactions with quarks, gluons, and leptons [77].

of 10^{17} s necessary to explain the current presence of DM in the universe. Nevertheless, the other properties of such particle can be studied in detail at particle colliders and compared with the DM cosmological constraints.

The complementarity between DM searches is illustrated in Figure 2.8, where the correct DM relic density is assumed to be achieved through interactions with quarks, gluons, and leptons [77]. A similar picture remains valid also under different theoretical assumptions.

Chapter 3

Experimental apparatus

The search for DM in *pp* collisions presented here is performed with the data collected by the CMS experiment at the LHC. The LHC is an accelerator designed to collide protons at a center-of-mass energy of 14 TeV. From 2010 to 2011 the center-of-mass energy of 7 TeV was reached, while in 2012 and 2015 such energy was increased to 8 TeV and 13 TeV, respectively.

The LHC was built at the European Organization for Nuclear Research near Geneva to investigate the Brout-Englert-Higgs boson, recently discovered by the ATLAS and the CMS collaborations [30,31], to test the SM and to search for new physics. CMS is a general purpose detector located in one of the collision points of LHC.

In this chapter a description of LHC and of the CMS detector is presented.

3.1 The LHC

The Large Hadron Collider (LHC) [9] is a *pp* accelerator designed to collide protons at a center-of-mass energy of 14 TeV. In addition, the LHC plan involves heavy ions ($\mathrm{Pb}82^{+}$) collisions at an energy of 574 TeV per nucleus. The LHC, at the European Organization for Nuclear Research (CERN), is located and lays between 45 and 170 meters under the Franco-Swiss border in the surroundings of Geneva. It is a 27 km-long tunnel, which previously hosted the Large Electron Positron (LEP) accelerator.

Protons are accelerated up to 26 GeV through the LINear ACcelerator, the Proton Synchrotron Booster and the Proton Synchrotron. After this stage, protons are injected into the Super Proton Synchrotron and once an energy of 450 GeV is reached they are injected in the LHC rings. The LHC consists of two separate rings in which the protons are accelerated in opposite directions and are brought to collision at fixed interaction points. Accelerated protons are maintained on a circular path using superconducting dipole magnets, which provide a magnetic field of 8.3 T and operate at a temperature of 1.9 K. High Frequency (HF) cavities are used to accelerate the protons and to compensate for their energy loss in the circular orbit. The oscillation frequency of these cavities is tuned to 400 MHz and protons are required to be synchronized with it to be accelerated. For this reason, protons are grouped in so-called bunches with a designed inter-bunch distance of 25 ns. Quadrupole and sextupole magnets focus the particle beam to increase the interaction probability in the four collision points. Protons are accelerated and brought to the interaction points in 2808 bunches, containing 10^{11} protons each. The designed luminosity to be delivered to the experiments is $10^{34}\text{cm}^{-2}\text{s}^{-1}$.

Four main experiments are installed in the interaction points of the particle beams:

- A Large Ion Collider Experiment (ALICE) [78], a heavy ion detector especially built to analyze nucleus-nucleus interactions,
- Large Hadron Collider beauty (LHCb) [79], a b-physics detector,
- A Toroidal LHC ApparatuS (ATLAS) [61], a multipurpose experiment, and
- Compact Muon Solenoid (CMS), a multipurpose experiment.

A schematic overview of the injection chain, the LHC ring and of the experiments is shown in Figure 3.1.

3.1.1 Proton-proton collisions

The probability of having a particular physics event depends on the energy available in the collision and on the number of interacting particles. More specifically, the rate dN_{events}/dt of a process is given by:

$$\frac{dN_{events}}{dt} = \mathcal{L} \cdot \sigma$$

where the instantaneous luminosity $\mathcal{L}$ depends on several LHC parameters, as the number of bunches and of protons in each bunch. The integrated luminosity, defined as $L = \int \mathcal{L} dt$, measures the amount of data delivered by the LHC. The cross section, σ , is a function of the energy in the center-of-mass frame.

Proton-proton collisions are divided in two main classes:

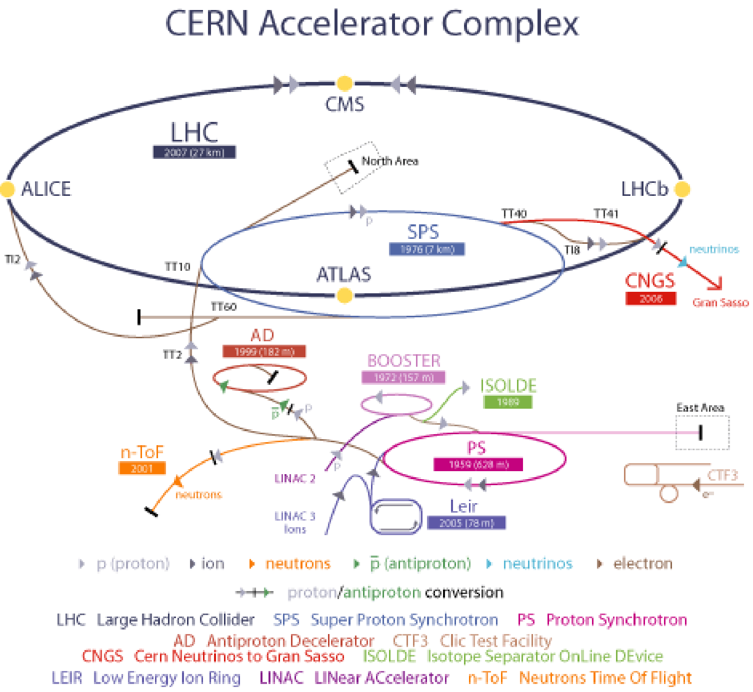

Figure 3.1: Schematic overview of the injection chain, the LHC ring and of the experiments at the interaction points [80].

- *soft*: proton collisions at large distances, where only a small momentum is transferred. In these collisions, particles are scattered at small angles with respect to the beam-axis (small transverse momentum),
- *hard*: protons collisions in which the proton constituents interact through a high momentum exchange. In these events, massive particles with high transverse momenta can be created.

In hard collisions [13], the effective center-of-mass energy $\sqrt{\hat{s}}$ depends on the energy fractions x_a and x_b carried by the two interacting partons a and b of the colliding protons:

$$\sqrt{\hat{s}} = \sqrt{x_a x_b s}$$

where $\sqrt{s}$ is the center-of-mass energy of the pp system. In hard interactions, $\sqrt{\hat{s}}$ is variable and unknown. For this reason, requirements on the conservation of longitudinal momenta cannot be applied. Nevertheless, the initial transverse momenta of the interacting partons are considered negligible and rules of conservation of this component can be applied. The conservation of the transverse momenta allows to infer the presence of particles that escape the detector without interacting with its components.

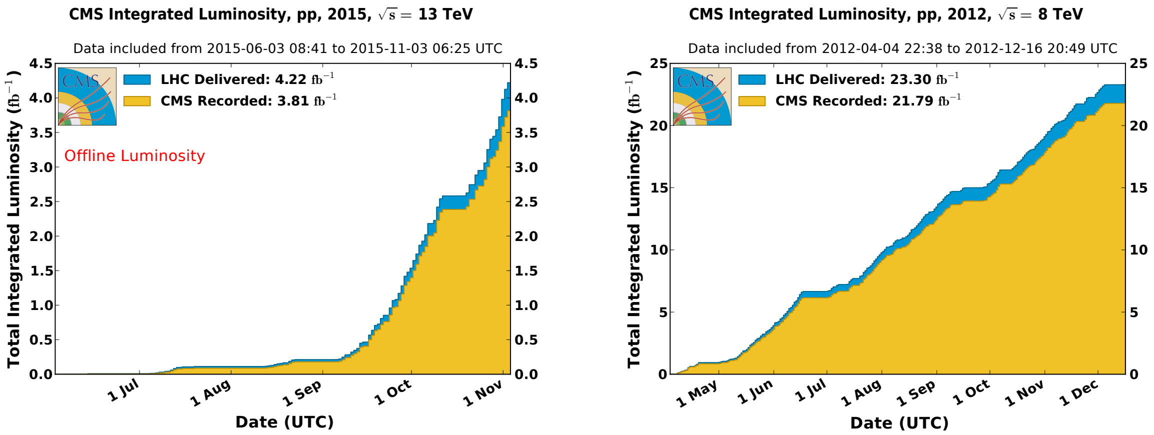

(a) (b)

Figure 3.2: Integrated luminosity delivered by LHC (blue curve) and recorded by the CMS experiment (yellow curve) in 2015 (a) and 2012 (b) during stable beams and for p-p collisions at 13 TeV and 8 TeV centre-of-mass energy respectively. The luminosity is determined from counting rates as measured by the luminosity detectors after offline validation [82, 83].

From 2010 to 2011, LHC collided protons at a center-of-mass energy of 7 TeV. In 2012 and 2015, the center-of-mass energy reached 8 TeV and 13 TeV, respectively. The data recorded by CMS and certified good for physics analyses correspond to an integrated luminosity of 34.68 pb^{-1} and of 5.09 fb^{-1} for 2010 and 2011 [81]. In the 2012 and 2015 periods, the collected and certified datasets correspond to integrate luminosities of 19.7 fb^{-1} and 2.2 fb^{-1}, respectively. Data are defined good for physics analyses if all subdetectors and physics objects reconstructions show the expected performance.

The total integrated luminosities delivered by LHC and recorded by CMS over the years 2015 and 2012 are shown in Figure 3.2.

3.2 CMS detector

The Compact Muon Solenoid (CMS) is a multipurpose detector built to study unknown SM physics and its extensions. A schematic view of the CMS apparatus is shown in Figure 3.3.

In order to describe the position and kinematic of particles within the detector, a coordinate system is defined as follow. The origin of the coordinates is identified by the geometrical center of the detector. The x-axis is taken to be horizontal and oriented towards the center of the LHC ring, while the y-axis points vertically upwards. The z-axis is oriented anti-clockwise along the beam direction. The transverse momentum

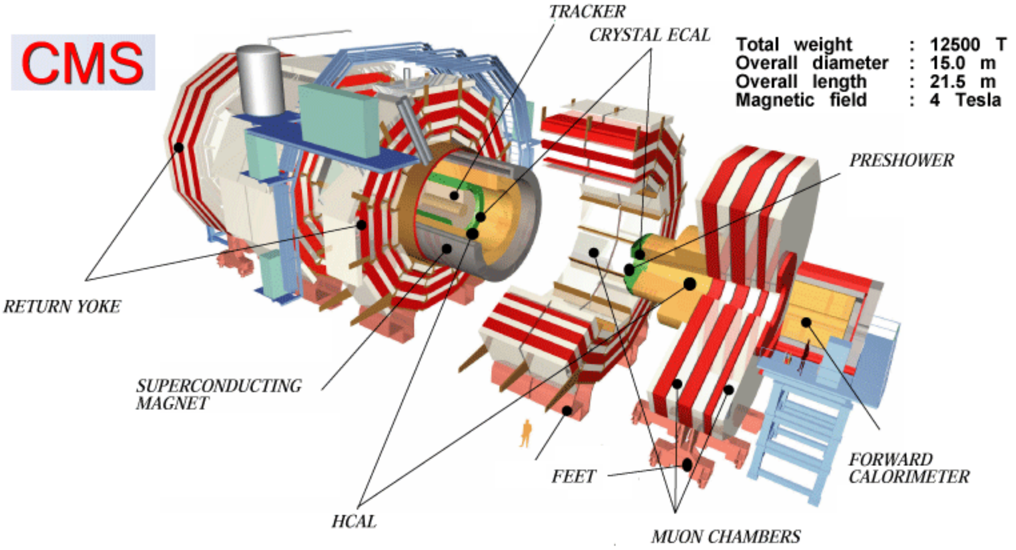

Figure 3.3: Schematic view of the CMS apparatus with its components [84].

and energy are measured in the xy-plane. The azimuthal angle ϕ is also measured in the xy-plane with respect to the x-axis. The polar angle θ is defined as the angle formed with respect to the z-axis, and is used to define the pseudorapidity variable $\eta = -\ln\tan(\theta/2)$.

CMS identifies all interacting particles and determine their energy and momenta. In order to accomplish these measurements CMS has:

- a tracking system embedded in a magnetic field,
- an electromagnetic and a hadronic calorimeters, and
- a muon system,

as shown in Figure 3.4.

The high LHC bunch crossing rate requires an online trigger system, which allows to process and store only events interesting for physics analysis. The high particle flux, also requires to meet high standards concerning fast electronics and radiation hardness for most components of the detector.

In the following, a summary of the characteristics and performances of each CMS subdetector is presented. Details about the CMS detector can be found in [10, 86, 87]

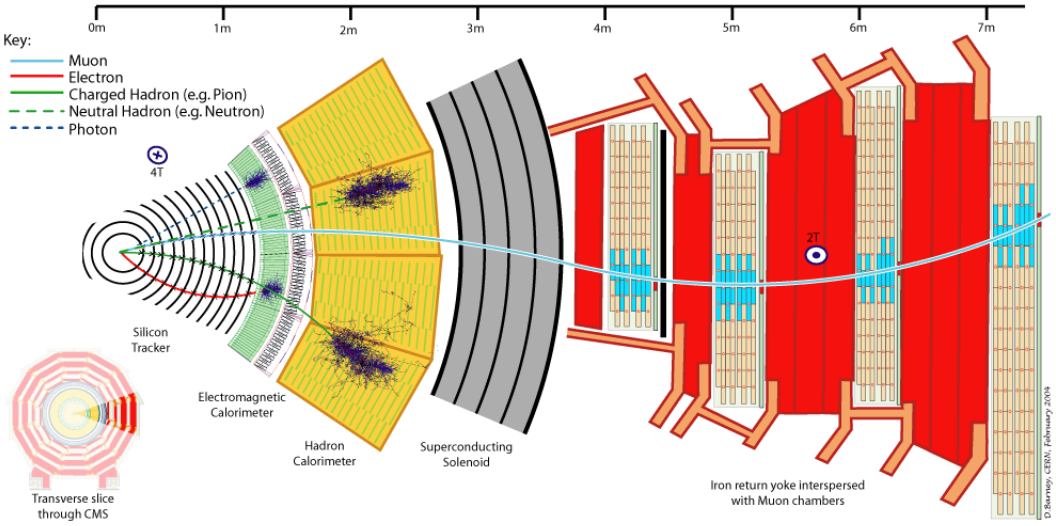

Figure 3.4: Schematic view of a transverse slice of the CMS detector. It is also shown how the different long-lived particles interact with each subdetector. This information is exploited to distinguish the different type of particles [85].

3.2.1 Magnet

In CMS, almost all the different subdetectors are embedded in a 3.8 Tesla magnetic field oriented parallel to the beamline. It is generated by a 13 m long superconducting solenoid with a diameter of 6 m [86]. The return field in the muon system is large enough to saturate 1.5 m of iron.

Charged particles move in helical trajectories inside the CMS magnetic field. The deflection angle θ in the plane transverse to the beamline is approximated by $\theta = \rho/L$, where ρ is the bending radius and L is the solenoid length [88]. From the curvature radius, the momentum component p_T perpendicular to the magnetic field B is obtained as [24]:

$$p_T = 0.3zB\rho$$

assuming a particle of charge ze. The associated relative error $\sigma(p_T)/p_T$ depends on the number of points N registered in the tracker system to measure the particle position with a spatial resolution σ [88]:

$$\frac{\sigma(p_T)}{p_T} = \frac{\sigma p_T}{0.3BL^2}\sqrt{\frac{720}{N+4}}$$

The CMS magnetic field is designed to provide a momentum resolution for charged

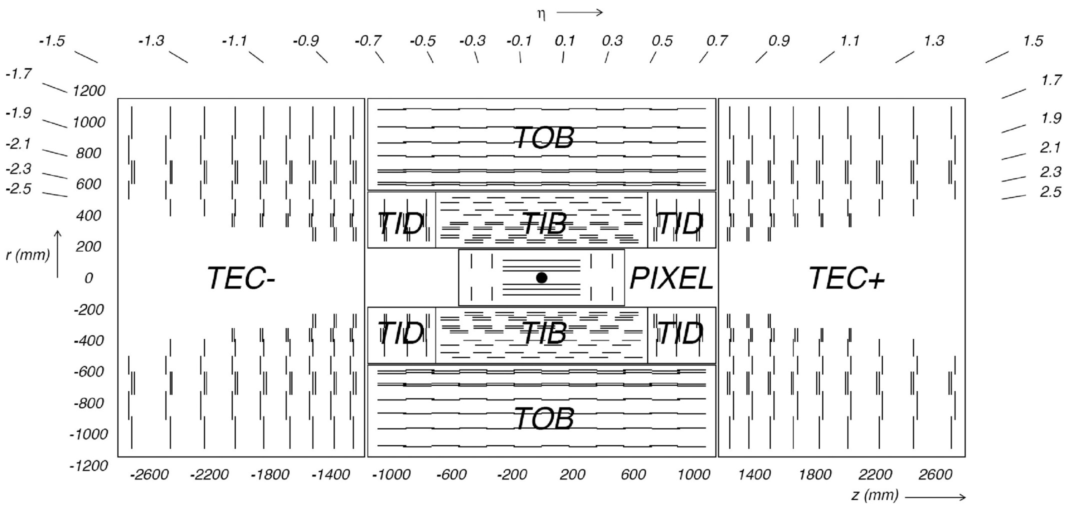

Figure 3.5: Schematic overview of the CMS tracker detector in the r-z plane [10].

particles of typically 1% for $p_T = 100$ GeV [89].

3.2.2 Inner tracking detectors

The CMS inner tracking system [90–92] allows charged particles pattern recognition. Exploiting the effect of the solenoid magnet, the momentum of charged particles is then measured.

The tracker features silicon pixels and microstrip detectors. A schematic view of the tracker system is shown in Figure 3.5.

Silicon pixels are placed close to the interaction point and constitute the innermost layer of the tracker. Silicon pixel detectors are grouped in layers, three for the barrel positioned at radii $r = 4.4$, 7.3 and 10.2 cm, and two for the endcaps positioned at z values on both sides, with $z = \pm 34.5$ and ± 46.5 cm. This configuration allows to precisely reconstruct primary and secondary vertices (Section 4.2.2), and to discriminate heavy flavour from light flavour quarks. Silicon pixel detectors have a spatial resolution of better than $10\,\mu$m in the $r - \phi$ plane and of about $20\,\mu$m in the z-axis [86].

Silicon microstrips surround the pixel detector and are grouped in three larger subsystems: Tracker Inner Barrel and Disks (TIB/TID), Tracker Outer Barrel (TOB), and Tracker End Cap (TEC). Silicon microstrips have a resolution between $35\,\mu m$ and $52\,\mu$m depending on the direction [86].

The tracker system has a total length of 5.8 m and a diameter of 2.6 m, and it covers a pseudorapidity region up to $|\eta| < 2.5$. Using only the information from the inner tracking system, the expected momentum resolution for a muon as a function of its

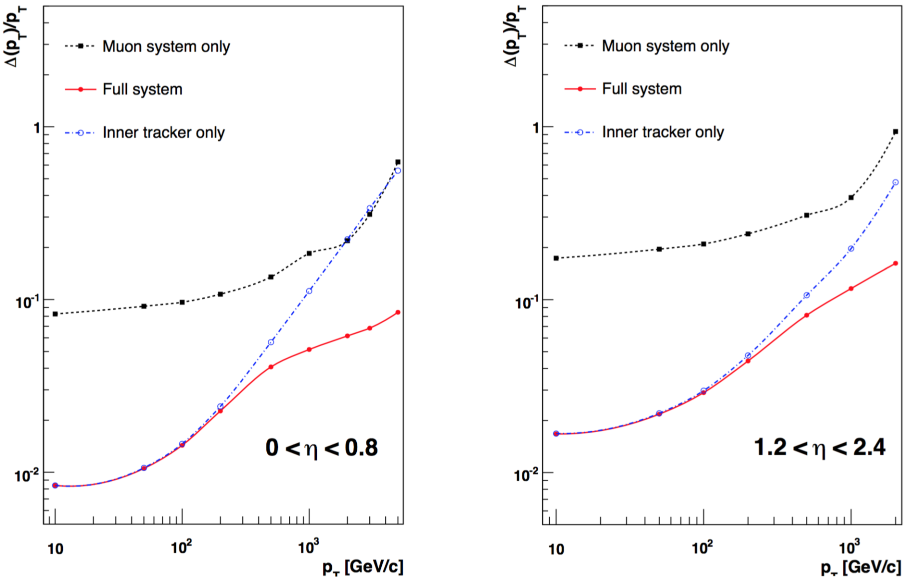

(a) (b)

Figure 3.6: The muon transverse momentum resolution as a function of the transverse momentum p_T using the muon system only, the inner tracking only, and both in the $|\eta| < 0.8$ (a) and $1.2 < |\eta| < 2.4$ regions [10].

transverse momentum is shown in Figure 3.6.

3.2.3 Calorimeter

The calorimeter system measures the energy of particles through their interactions with matter and allows to infer the presence of neutral particles.

It features two different parts: electromagnetic and hadronic calorimeter. In the electromagnetic calorimeter the particle energy is measured through electromagnetic showers, while in the hadronic part through inelastic scattering.

Information from the calorimeter system is also exploited to trigger on event interesting for physics analyses.

Electromagnetic calorimeter

The Electromagnetic CALorimeter (ECAL) [93] is a hermetic and homogeneous calorimeter made of $PbWO_4$ crystals. The ECAL is split into a barrel (EB) and two endcap (EE) regions. A schematic view of the electromagnetic calorimeter configuration is shown in Figure 3.7.

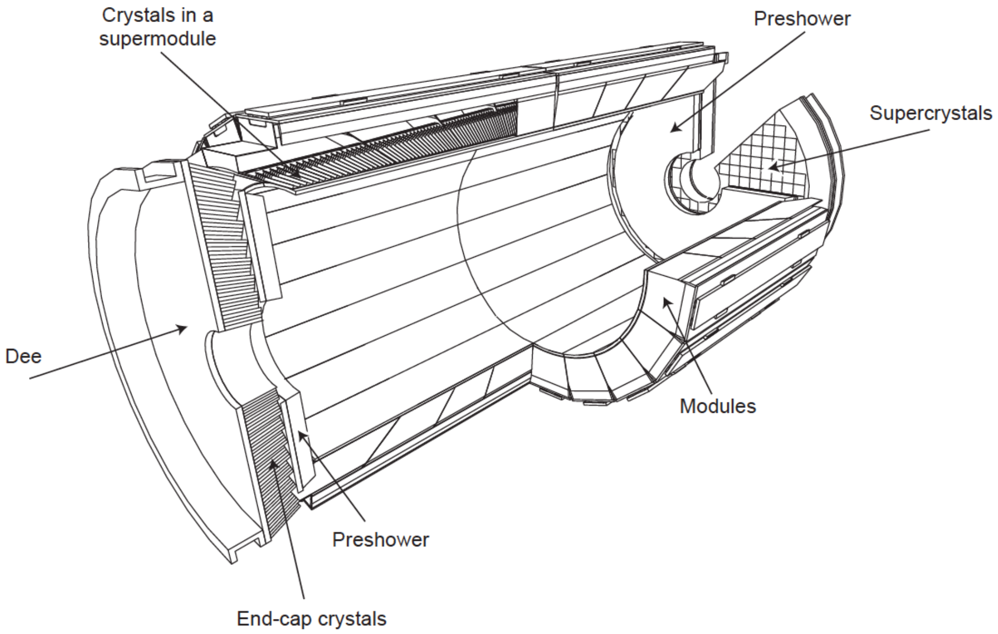

Figure 3.7: Layout of the CMS ECAL showing the arrangement of crystal modules, supermodules and endcaps, with the preshower in front. [10].

The barrel part covers a pseudorapidity interval up to $|\eta| < 1.479$, while both endcaps cover a range $1.479 < |\eta| < 3.0$. The crystals used in the barrel and endcaps have a cross-sectional area of 22×22 mm^2 and 28.6×28.6 mm^2, respectively [93].

Between the tracking system and the EE, a preshower detector made of two silicon sensors planes is located, which covers a pseudorapidity range $1.653 < |\eta| < 2.6$. It allows to distinguish between two closely-spaced photons showers from π^0 and a single-showers from γ because of its finer granularity (~ 2 mm pitch silicon sensors) [93].

The ECAL measures the particles energies with a resolution in the range 0.4% to 1.5% for energies in the interval $10 - 250$ GeV [94].

Hadronic calorimeter

The Hadronic CALorimeter (HCAL) [10,95] is formed by alternating layers of absorbing plates and active material. The HCAL is divided into a barrel (HB and HO) part, the endcap (HE) detectors and a forward calorimeter (HF). The HB and HE are both sampling calorimeters where the absorber is brass and the active material is a plastic scintillator. A schematic view of the HCAL configuration is shown in Figure 3.8.

The barrel part covers a pseudorapidity range up to $|\eta| < 1.3$, each endcap covers an interval $1.3 < |\eta| < 3.0$ and the HF extends up to $|\eta| < 5.2$ to maximize the coverage.

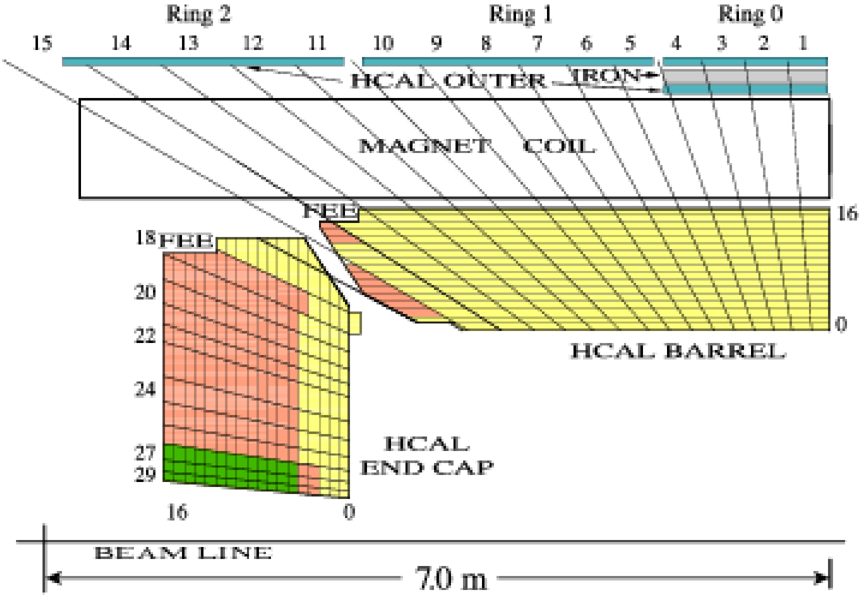

Figure 3.8: The HCAL tower segmentation in the rz-plane for one-fourth of the HB, HO, and HE detectors [10].

To achieve a precise energy measurement, a large fraction of the hadronic shower has to be collected by the calorimeter scintillators. For the HB the thickness is limited to 5.8 (10) hadronic interaction lengths at $|\eta| = 0$ (1.2). This is due to the available space between the outer extent of the electromagnetic calorimeter ($R = 1.77$ m) and the inner part of the magnet coil ($R = 2.95$ m). The HB is complemented with the HO, which is placed outside the magnet and exploit the solenoid as additional absorbing material. This setup allows to sample, with a thickness up to 11.8 interaction lengths, showers that leak out from the HB.

The HF calorimeter requires the use of radiation-hard materials because in the forward region the hadron rate is extremely high. On average, at $\sqrt{s} = 14$ TeV an energy of 760 GeV per pp interaction is deposited, to be compared with an energy of ~ 100 GeV in the rest of the detector [10]. For this reason, steel is used as absorber and quartz fibers are inserted as active medium.

Combined with the information from the ECAL, the barrel HCAL energy resolution σ_E is parametrized as [96]:

$$\left(\frac{\sigma_E}{E}\right)^2 = \left(\frac{0.847}{\sqrt{E/\mathrm{GeV}}}\right)^2 + (0.074)^2$$

for energies E in the range 30 GeV $-$ 1 TeV. The energy resolution for the endcap part

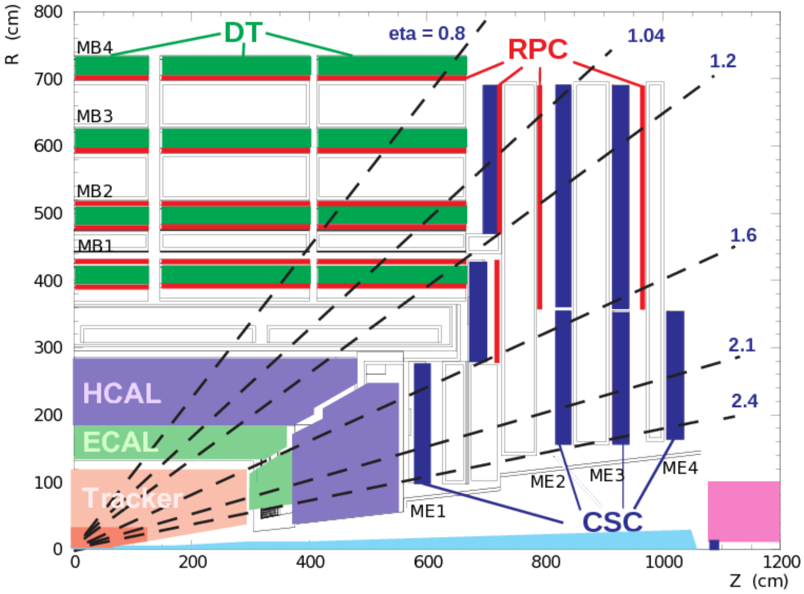

Figure 3.9: Schematic view of the CMS muon system [98].

is given by the same equation substituting 0.847 (0.074) with 1.98 (0.09).

3.2.4 Muon system

The CMS muon system [10, 97] identifies and measures the momentum of muons and provides a trigger for event selection. The muon system is the outermost subdetector and is placed outside the solenoid. It is divided into a barrel region and two endcap parts, as shown schematically in Figure 3.9.

The barrel region covers a pseudorapidity range up to $|\eta| < 1.2$ and features four layers of drift tubes (DT) chambers. The choice of DT as gaseous particle detectors is due to the low muon rate, the small neutron induced background, and the uniformity of the magnetic field in this region. The DT chambers are interleaved with the iron yoke plates. The magnetic flux in these iron plates provides the possibility of independent momentum measurements.

Both endcap regions cover a pseudorapidity interval $0.9 < |\eta| < 2.4$. In this part, the muon rate and the neutron induced background are higher and the magnetic field is large and non-uniform. Therefore, a faster response time, finer segmentation and radiation resistance is required. For these reasons cathode strip chambers (CSC) are used as detectors.

Resistive plate chambers (RPCs) are placed both in the barrel and endcap regions and cover a pseudorapidity interval $|\eta| < 1.6$. RPCs are used as complementary trigger system and to improve operations at high rates. RPC have coarser position resolution than the DTs or CSCs, but they can be used to resolve ambiguities when building a track from multiple hits in a chamber.

The resolution achieved for single point measurements is about $200\,\mu$m, both for drift tubes and for cathode strip chambers [86]. Using only the information from the muon system, the expected momentum resolution for a muon as a function of its transverse momentum is shown in Figure 3.6.

3.2.5 Readout system

In *pp* collisions at the LHC, the designed beam crossing interval is of 25 ns, which corresponds to a crossing frequency of 40 MHz. At the designed LHC luminosity, an average of 20 simultaneous *pp* collisions occur per bunch crossing. This translates in an enormous amount of data to be processed and stored. For this reason, the input rate must be greatly reduced by selecting only events that are of interest for physics analysis.

At the CMS, this reduction is done by a trigger system [99] divided in two parts: a hardware trigger named Level-1 (L1) and a software trigger named High Level Trigger (HLT). The rate reduction is designed to be of a factor 10^6 or higher for the combined L1 Trigger and HLT [10]. A Data Acquisition (DAQ) system is used to collect the data that pass the L1 trigger decision and to provide computing power to the HLT for the information rate reduction [100]. A schematic view of the trigger system and the DAQ is shown in Figure 3.10.

Level-1 Trigger

The L1 trigger analyzes every bunch crossing and takes a decision based on a subset of the event information. A positive trigger decision is obtained if the so-called trigger primitives are present, for example hits in the muons chambers or calorimeter measurements above threshold. A decision has to be reached in less than 3.2 μs.

The output rate of the L1 trigger is about 30 kHz, which is suitable for further processing by the HLT. The trigger architecture is shown in Figure 3.11.

High Level Trigger

The data that pass the L1 trigger are transferred to the front-end readout buffers and then to the central processing units that run the HLT software. The HLT has a more

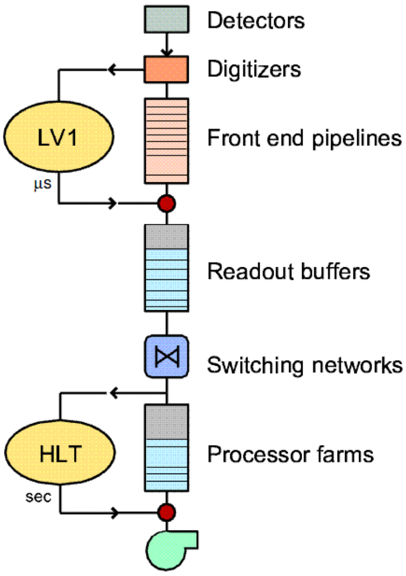

(a)

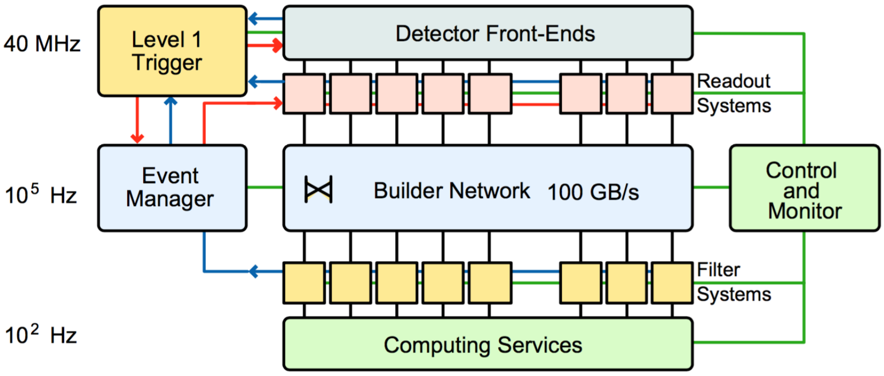

(b)

Figure 3.10: Schematic view of the CMS trigger system configuration (a) and of the CMS DAQ architecture [10].

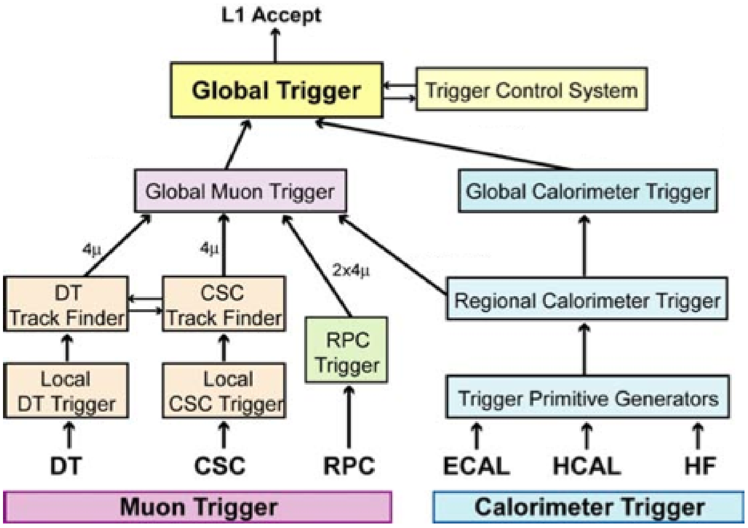

Figure 3.11: Schematic view of the CMS trigger system configuration [10].

complex criteria to reduce the event rate with respect to the L1. On average, a decision takes 40 ms and all subdetectors information is used.

The output from the HLT has a rate of 100 Hz, which is suitable for data storing.

Data acquisition and computing

The computing system permits to store, manage and analyze the data collected with the experimental apparatus. During CMS operation, the output of the trigger system is stored at the Tier 0, which is the computing centre at CERN.

The amount of real and simulated data is such to require the distribution to other computing centres (Tier 1, Tier 2, Tier 3), located all over the world. All centres are interconnected and form the so-called computing Grid that is used, in addition to storage purposes, to process the data from the four LHC experiments [10]. More details about the LHC computing Grid can be found in [101].

Chapter 4

Analysis tools

Monte Carlo event generators are employed in the presented analysis to simulate the production of DM particles in *pp* collisions, as well as SM processes that mimic the kinematics of signal events. Furthermore, simulated events allow to estimate the detector response to the particles produced in the collision. An overview of the *pp* collisions simulation is presented in Section 4.1.

After the simulation of the collision and of the detector response, generated and real events are reconstructed from the information of the various CMS subdetectors. The techniques employed to reconstruct and identify the stable particles produced in the collision and used in the analysis are presented in Section 4.2.

4.1 Monte Carlo simulation

Monte Carlo (MC) event generators are used to fully simulate the proton-proton collisions produced at the LHC. The simulated events allow to investigate the kinematic topology of the inelastic collisions and to estimate the detector response to particles produced in the collision.

The simulation of *pp* interactions at colliders is divided in steps: event generation, tracking of particles through the material, and detector response. These different components of the event simulation describe the physics of the collision starting from short distance scales, less than a fm, where the hard interaction collisions are produced and perturbation theory can be used to describe them. Then as hadrons form and decay as moving to a larger scale, the simulation cannot longer use perturbation theory and phenomenological models are employed instead [24].

The response of the detector is later added to the simulation. Finally, all simulated samples are processed as real data through reconstruction and physics analysis. In collider physics, MC simulation methods are used both to generate events and to propagate particles through the detector.

4.1.1 Event generation

The event generation is typically divided in three steps: hard scattering process, parton shower, and hadronization, as explained in the following.

Hard scattering process

In high energy collisions, the interaction occur between individual constituents of the protons (quarks and gluons). The probability to find a parton i inside a beam particle a with a fraction x of the total momentum is described by the Parton Density Function (PDF), $f_i^a(x, Q^2)$. These functions depend on the energy scale Q^2 characterizing the hard process and are obtained from measurements in Deep Inelastic Scattering (DIS) experiments [102].

The cross section for a general hadronic process $i + j \to X + Y$ is given by [103]

$$\sigma_{i+j\to X+Y} = \int dx_1 \int dx_2 f_i^1(x_1, Q^2) f_j^2(x_2, Q^2) \hat{\sigma}_{i+j\to X+Y}, \tag{4.1}$$

where $\hat{\sigma}$ is the cross section for the hard partonic process.

The parton sum extends to $u,\ d,\ s,\ c$ quarks and gluons in the so-called 4-flavour scheme, while in the 5-flavour scheme also the b quark is taken into account. In the computation of the final cross section, the unknown energy scale Q^2 and the x fractions are integrated out.

The hard process cross section is calculated from Feynman diagram matrix elements using perturbation theory at different fixed order of approximation. For example, at Leading Order (LO) the lowest number of vertices needed to describe the physics process is considered, while at Next-to-Leading Order (NLO) diagrams with a greater number of vertices than in the LO are considered in the perturbation. For higher orders computation of QCD processes, that include for example real emission by radiation, divergences appears and as a solution energy scales are introduced, namely factorization and renormalization scales [104].

Parton shower

Initial and final state radiation (ISR and FSR) of gluons and photons may cause large corrections to the event cross section. These higher order corrections are included in the ME calculation or in the parton-shower step [103].

In the latter approach, secondary partons are generated considering the branching rates $e \to e\gamma$, $q \to qg$, $q \to q\gamma$, $g \to gg$, and $g \to qq$. The probability for a parton i to split into j and k is proportional to the integral $\int P_{i\to jk}(z)dz$, where $P_{i\to jk}(z)$ are the splitting kernel given by the Altarelli-Parisi equation [105] and z describes the sharing of the initial parton energy among the daughters.

If higher orders corrections are considered at the hard interaction level, the same process can be described both by the ME and the parton shower. Double counting of these events is avoided using a matching algorithm.

Hadronization and decay

The partons produced in the hard scattering process carry strong colour charge and are not directly detected. In fact, only colour-neutral configurations are allowed in nature.

The process of formation of colourless hadrons from partons is called hadronization and is described through phenomenological models. String and cluster models are commonly used [103]. At a later stage the unstable hadrons are decayed.

Underlying event

Beam remnants from the hard scattering process have soft interactions or hadronize into neutral-colour particles. Both these types of processes are described by the underlying event (UE) and lead to additional hadrons in the final state.

The precise modeling of the UE is essential for the experiments. In general, the UE is characterized by low energy processes modeled through non-perturbative QCD [106]. The interactions of the beam remnants are not described in the hard scattering processes. Instead, the additional hadrons in the final state are included at the detector simulation step.

4.1.2 Detector response simulation

After the event generation, the passage of the produced particles through the detector is simulated using MC methods.

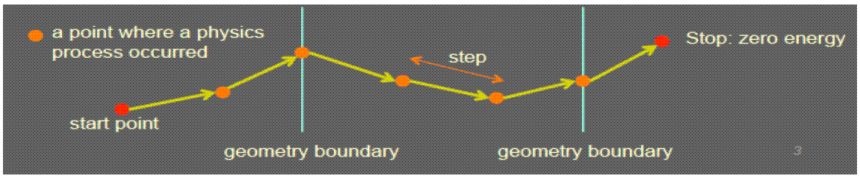

(a)

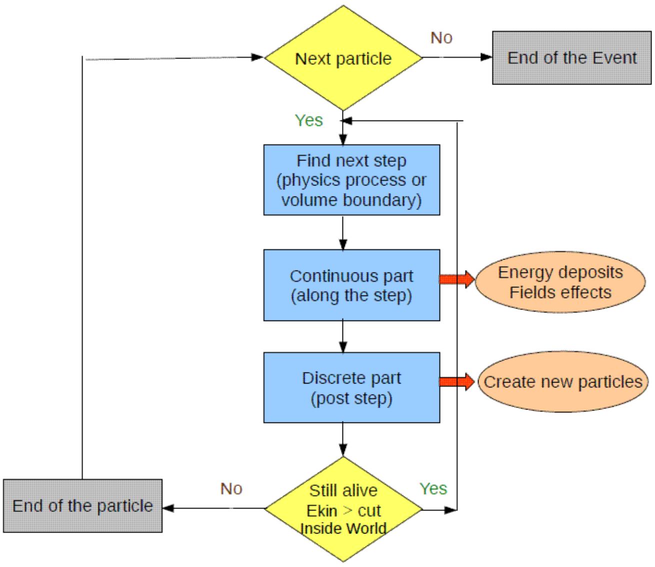

(b)

Figure 4.1: Schematic view of the particle trajectory inside the detector divided in steps (a) and of the MC detector simulation functioning (b) [108].

The detector simulation takes into account the geometry of the experimental apparatus and the physical processes that take place when the produced particles interact with the detector. The CMS detector simulation uses GEANT4 [107].

In the detector simulation phase, each particle produced in the event generation is considered at a time. The particle trajectory inside the detector is divided in steps of lengths determined by the physical process cross section and the geometrical boundaries of the detector, as shown in Figure 4.1(a). For each of these steps, the interactions between the particle and the detector material are considered and the energy deposits simulated. New particles produced in these interactions are added to the input list of particles whose trajectory has to be simulated. This procedure is continued until each particle leaves the detector region, or its energy is below tracking threshold, or it decays. A schematic view of the working steps of the detector simulation is given in Fig. 4.1(b).

After this simulation step, hits in the detector are produced that simulate the response of the readout electronics. The same reconstruction of objects, as explained below, is subsequently applied to collision LHC data and simulation.

4.2 Objects reconstruction

Reconstruction and identification of stable particles is performed in CMS using the so-called particle-flow (PF) algorithm [109]. This technique combines the information of all CMS subdetectors to achieve an optimal determination of the particle direction, energy, and type. In the following, the main elements of the PF technique are presented.

4.2.1 Particle-flow event reconstruction

To reconstruct stable particles, the PF technique starts from three main elements (PF elements): charged-particle tracks, calorimetric clusters, and muon tracks [109, 110].

Each particle has more than one PF element associated to it, corresponding to its interactions with the various subdetectors. The elements belonging to the same particle are grouped together in blocks by a link algorithm [109]. Starting from these collections, the PF algorithm reconstructs and identifies the particles produced in the event following the order: muons, electrons, charged hadrons, photons and neutral hadrons. The reconstructed stable particles are then used to reconstruct jets and calculate the missing energy in the transverse plane. From reconstructed jets it is possible to infer the energy and direction of quarks or gluons before their hadronization, while from the missing transverse energy we can estimate energy and direction of particles that do not interact with the detector.

Particle tracks are also used to reconstruct and identify the location of all pp interaction vertices.

In the next sections, the reconstruction and identification procedures for interaction vertices and for the particles used in this analysis are presented in more detail. The method employed for track reconstruction is explained in the following.

Tracks

Charged particle trajectories (tracks) inside CMS are reconstructed from hits in the tracking system and provide measurements of the particle momentum and direction.

The high number of particles produced in a *pp* interaction translates in a large number of hits in the detector and in a computationally challenging reconstruction of tracks.

In CMS, track reconstruction is performed with the so-called Combinatorial Tracker Finder software, which is based on a Kalman filter technique [111–113], through an iterative tracking process [109, 110]. In this strategy, tracks are seeded with pixel hits close to the interaction point and $p_T > 0.8$ GeV. The seed trajectories are then extrapolated along the foreseen particle path, and compatible hits are associated to the track candidate using a combinatorial Kalman filter. After the hits are assigned to the particle trajectory, a fit is performed to extract the momentum and direction parameters.

Quality parameters, as the transverse impact parameter and the number of layers in which hits are found, are imposed to suppress reconstructed tracks not associated with particles (fake tracks). If a track passes these requirements, the associated hits are removed from the input list. A new iteration is then performed with the residual hits lowering the seeding requirements.

4.2.2 Primary vertex and pileup

Reconstruction

Primary-vertex (PV) reconstruction [110] is used to identify and measure the location of all *pp* interaction vertices present in the same LHC bunch crossing.

The reconstruction is divided in different steps:

- *track selection*, all tracks consistent with being produced promptly in the primary interaction region are selected. This requirement is checked based on the significance of the transverse impact parameter relative to the centre of the beam spot, the number of hits in the tracker, and on the normalized χ_2 associated with each track;

- *track clustering*, selected tracks are clustered using a deterministic annealing algorithm (DA) [114] based on the track z-coordinate of closest approach to the luminous region;

- *fitting for vertex position*, vertex parameters are computed with an adaptive vertex fitter [115] for all candidates with at least two tracks. In this procedure, a weight w_i close to 1 (0) is assigned to each track i if the probability of originating from the considered vertex is high (low). The performance of the fit is then

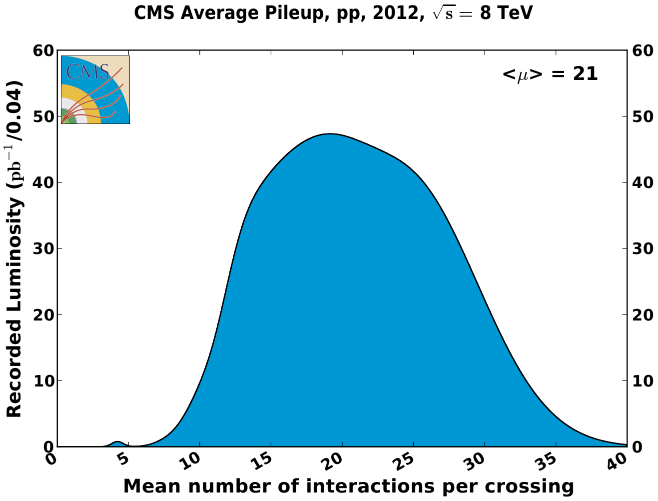

Figure 4.2: Number of interactions per bunch crossing in *pp* collisions recorded by the CMS experiment in 2012 at $\sqrt{s} = 8$ TeV [116].

evaluated from the number of degrees of freedom n_{dof}, defined as:

$$n_{dof} = -3 + 2 \sum_{i=1}^{\#tracks} w_i$$

The PV is defined as the reconstructed vertex with the highest value of $\sum_i p_{T_i}^2$. Here, p_{T_i} is the transverse momentum of the track i belonging to the vertex.

The additional *pp* interactions occurring in the same bunch crossing, or out of time, are referred as pileup (PU) events. The 2015 and 2012 data are recorded in a period of time in which the number of PU interactions in the same bunch crossing is on average 11 and 21, respectively. The distribution of the average number of PU for the 2012 data-taking is shown as an example in Figure 4.2.

Secondary vertices from decay of long-lived particles are identified as vertices displaced with respect to the primary interaction but consistent with the momentum direction of the track associated to the PV.

The resolution on the position of a reconstructed PV depends on the p_T and number of tracks used in the fitting procedure. For minimum-bias events, processes where no hard scattering occur, the resolution achieved using at least 50 tracks is less than 20 μm and 25 μm in x and z, respectively [110]. For mean PU of 8, the PV reconstruction efficiency is close to 100% if more than two tracks are used for the reconstruction. This efficiency decreases with higher values of PU [110].

Selection

In this work, reconstructed vertices are selected if they are consistent with the expected interaction point. This is verified asking $n_{dof} > 4$ and the vertex to be less than 2 (24) cm away in the x, y (z) direction from the interaction point. In the presented analysis, at least one selected vertex is required in the event.

Due to PU events, particle tracks and energy deposits not associated with the primary interaction are registered. Two algorithms are employed to subtract these contributions in the reconstruction of the event. One algorithm filters all the charged hadrons not compatible with the primary interaction (track-based). The other estimates the energy density in the calorimeter due to PU events and subtracts this value from the total energy measurement (calorimeter-based) [117].

4.2.3 Muons

Reconstruction

The muon reconstruction in CMS is presented in this section. A more detailed description is found in [118].

Muon reconstruction starts from tracks in the inner tracker (tracker track) and in the muon spectrometer (standalone-muon track). These tracks are reconstructed from hits collected in the DT, CSC, and RPC subdetectors with the same procedure explained in Section 4.2.1. In this work, *global muon* [118] candidates are considered, which are reconstructed matching a standalone-muon track to a tracker track. The hits in both subdetectors are then re-fitted. If at the matching stage there are ambiguities, the χ^2 of the global fit is used to select a unique global muon. This approach improves the momentum resolution for candidates with $p_T > 200$ GeV compared to what is achieved considering tracker tracks alone [119, 120].

Within the PF algorithm, global muons candidates are selected if their combined momentum is compatible with that determined from the sole tracker within three standard deviations. This requirement increases the correct identification of muons within jets and lower the misidentification of charged hadrons as muons.

Selection

The purity of the muon candidates sample is increased by applying a selection at the analysis level, which is based on:

Variable type	Variable name	tight cat.	loose cat.
Reconstruction	global muon	yes	–
	global or tracker muon	–	yes
	PF muon	yes	yes
Identification	$\chi^2/d.o.f.$	< 10	–
	muon chamber hits in global fit	> 0	–
	segments with two muon stations	> 1	–
	inner tracker hits	> 0	–
	tracker layers with hit	> 5	–
	d_{xy}	< 0.2 cm	–
	d_z	< 0.5cm	–
Isolation	Iso/p_T	< 0.15	< 0.25

Table 4.1: Muon identification selection for the tight and loose categories.

- $\chi^2/d.o.f.$, fit quality of the global-muon track,
- *number of hits* in the inner tracker and in the muon spectrometer,
- d_{xy} and d_z, transverse and longitudinal impact parameters with respect to the PV,
- *isolation* Iso/p_T, which controls the energy flow near the muon candidate trajectory relative to the muon p_T. The isolation Iso is defined as:

  $$\mathrm{Iso} = \sum p_T^{charged} + \left(\sum p_T^{neutral\ had} + \sum p_T^{\gamma} - p_T^{PU}\right) \tag{4.2}$$

  considering all PF candidates reconstructed within a cone of radius ΔR around the momentum direction of the muon candidate. In Equation 4.2, the first term refers to charged PF candidates originating from the primary vertex, the second to neutral hadrons, and the third to photons. The last term p_T^{PU} corrects the isolation for the energy associated to PU interactions. The muon candidate contribution is excluded from the computation.

The selection applied on these variables depends on the identification efficiency and purity desired for the analysis. In this work, the loose and loose identification categories are used to achieve an average efficiency of about 90% and 100%, respectively. The tight and loose identification selections for the 2015 data-taking period are presented in Table 4.1. A similar selection is applied for the data collected at 8 TeV.

Reconstruction and identification efficiencies are estimated in data using a tag-and-probe technique on Z $\rightarrow \mu^+\mu^-$ events [121]. As an example, the tight identification

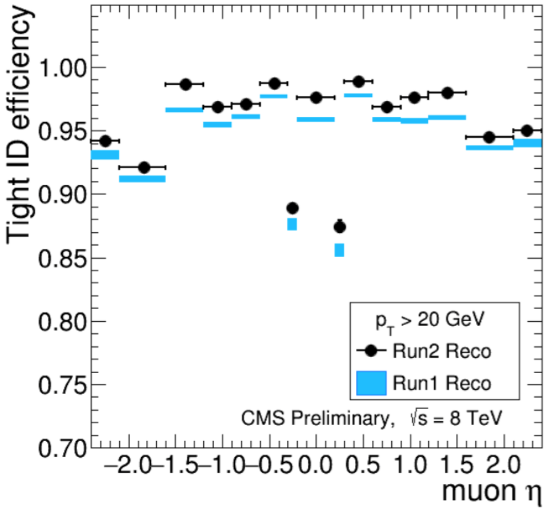

Figure 4.3: Muon tight category identification efficiency in data collected in *pp* collisions at $\sqrt{s} = 13$ (black point) and simulation (blue square) as a function of the muon $|\eta|$ [121].

efficiency in data and simulation is presented in Figure 4.3 as a function of the muon $|\eta|$. The efficiency results in data and simulation are compared and correction factors for the MC are derived based on the differences observed.

4.2.4 Electrons

Reconstruction

Electrons produced within the CMS detector loose up to 86% of their initial energy due to bremsstrahlung [122]. The exact energy loss depends on the intervening material before reaching the ECAL. The spread of the energy deposits over the ECAL crystals is mainly in the ϕ direction because of the motion of the electrons in the magnetic field. This energy drop translates in significant changes in the electron direction of motion and reduces the efficiency of standard track reconstruction methods. In addition, the energy of radiated photons has to be taken into account to precisely reconstruct the electron initial energy. Additional electrons from photon conversion can also occur.

These difficulties require a specific reconstruction procedure for electrons, which starts from energy measurements of ECAL superclusters that are formed from ECAL energy deposits using dedicated algorithms [122]. The superclusters are then matched to pairs or triplets of hits in the inner tracker layers (track seeds) compatible with being generated by an electron. Trajectories of the electron candidates are reconstructed using a dedicated Gaussian sum filter (GSF) [123] that takes into account radiative energy losses for the electrons.

Jets or uncorrelated tracker hits can be reconstructed as electrons. This background is reduced with selections on the ECAL shower shape, the track-ECAL cluster matching, and on the probability for the candidate to come from the primary vertex, as explained in the following.

A more detailed description of electron reconstruction in CMS is found in [122].

Selection

In the presented analysis, electron are selected with $|\eta| < 2.5$, which corresponds to the pseudorapidity coverage of the tracker. The ECAL barrel-endcap overlap region, $1.4442 < |\eta| < 1.566$, is excluded because the reconstruction of an electron object in this region is not optimal.

Electrons are selected from reconstructed candidates based on the following criteria [122, 124]:

- Identification variables:
    - $\left|\frac{1}{E} - \frac{1}{p}\right|$, difference between the inverse of the energy E from the ECAL cluster and the inverse of the momentum p measured from the reconstructed track,
    - $|\Delta\eta_{in}|$ and $|\Delta\phi_{in}|$, spatial matching between track and supercluster in η and ϕ,
    - σ_{inin}, width of the supercluster along the η direction,
    - H/E, hadronic leakage variable that measures the energy fraction deposited in the HCAL,
- Rejection of electrons from conversion:
    - d_{xy} and d_z, transverse and longitudinal impact parameters with respect to the PV. Electrons from conversion tend to have greater distances to the beam position,
    - *missing hits*, electrons from conversion are characterized by missing hits in the innermost tracker layers,
    - *conversion veto*, a fit is performed to find the probability for a reconstructed track to come from a conversion vertex,

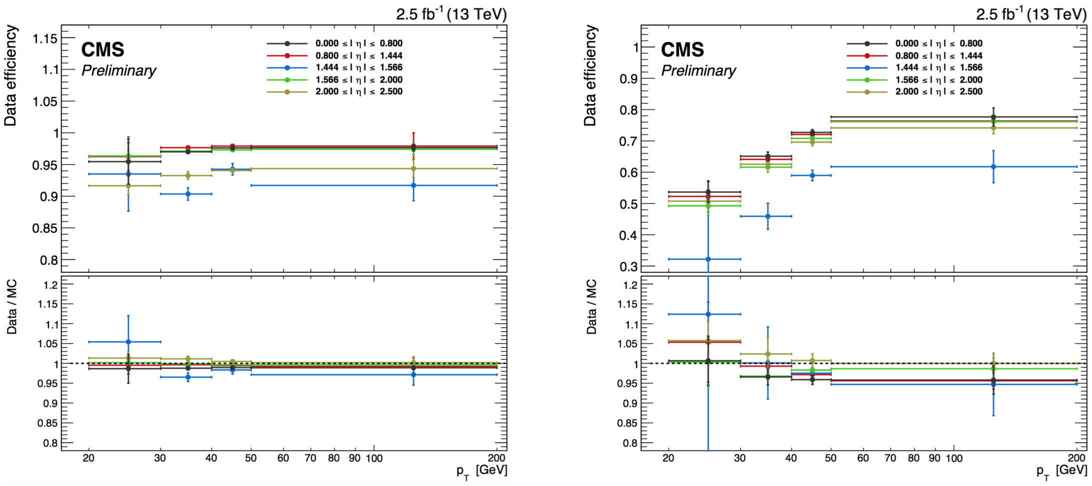

(a) (b)

Figure 4.4: Electron reconstruction (a) and tight category identification (b) efficiency in data collected in pp collisions at $\sqrt{s} = 13$ (top pad) and data to simulation efficiency ratios (bottom pad) as a function of p_T and for different $|\eta|$ of the electron [125].

- Isolation requirements:
  - Iso/p_T, the main backgrounds for primary electrons come from misidentified jets and electrons from semileptonic quark decays. In this case, a higher energy activity close to the electron trajectory is registered. The Iso/p_T variable is defined as for the muon, Equation 4.2.

Different categories for electron identification are defined: veto, loose, medium and tight. This division is based on the selection applied on the discussed variables in order to achieve an average electron identification efficiency of 95, 90, 80 or of 70%, respectively. The probability of misidentify background as electrons is less than 4% for the tight identification criteria. The selection of each category is optimized separately for candidates in the ECAL barrel and endcaps. In this analysis, tight and veto categories are used and their associated selections are presented in Table 4.2 for the 13 TeV analysis. A similar selection is applied for the data collected at 8 TeV.

Reconstruction and identification efficiencies are estimated in data using a tag-and-probe technique on $Z \to e^+e^-$ events [122,125]. As an example, the reconstruction and tight electron identification efficiencies in data and simulation are presented in Figure 4.4 as a function of p_T and for different $|\eta|$. The results are compared and correction factors for the simulation are derived based on the differences observed.

Variable type	Variable name	tight cat.		veto cat.	
		barrel	endcap	barrel	endcap
Identification	$\left\lvert \frac{1}{E} - \frac{1}{p} \right\rvert$	< 0.012	< 0.00999	< 0.207	< 0.174
	$\lvert\Delta\eta_{in}\rvert$	< 0.00926	< 0.00724	< 0.0152	< 0.0113
	$\lvert\Delta\phi_{in}\rvert$	< 0.0336	< 0.0918	< 0.216	< 0.237
	σ_{inin}	< 0.0101	< 0.0279	< 0.0114	< 0.0352
	H/E	< 0.0597	< 0.0615	< 0.181	< 0.116
Rejection conversion electrons	d_{xy}	< 0.0111 cm	< 0.0351 cm	< 0.0564	< 0.222
	d_z	< 0.0466cm	< 0.417cm	< 0.472	< 0.921
	missing hits	≤ 2	≤ 1	≤ 2	≤ 3
	conversion veto	false	false	false	false
Isolation	Iso/p_T	< 0.0354	< 0.0646	< 0.126	< 0.144

Table 4.2: Electron identification selection for tight and veto categories.

4.2.5 Jets

Reconstruction

Partons produced in the primary interaction carry strong colour charge and are not directly detected by the instrumentation, since only colour-neutral configurations are observed in nature. After production, partons undergo hadronization. In this process, a collimated group of colour-neutral particles, so-called jet, is generated with approximately the same direction of the parton from which originate. The energy and momentum of the parton produced in the primary interaction is reconstructed using a jet algorithm to cluster the particles coming from its hadronization.

The jet energy is shared among charged particles, photons and neutral hadrons with fractions of 65%, 25% and 10%, respectively. Because charged particle carry the highest energy portion, jets are reconstructed more precisely including the tracking system information in addition to calorimeters clusters. The additional information is taken into account employing all PF particles as input for the jet reconstruction. This type of jets, called PF-jets, are reconstructed with a higher precision with respect to jets built using HCAL and ECAL information only, called calo-jets [109]. The jet response, energy and direction resolutions are presented in Figure 4.5 for PF- and calo-jets, showing the better performances achieved using as input for the reconstruction all PF particles [109].

The jets used in this analysis are calculated using the $anti - k_T$ jet reconstruction algorithm [126] using as input all PF objects. The $anti - k_T$ algorithm reconstructs jets considering two input objects and defining their relative distance d_{ij} and the distance between each object and the beam d_{iB}:

$$d_{ij} = min\left(\frac{1}{p_{T_i}^2}, \frac{1}{p_{T_j}^2}\right)\frac{\Delta R_{ij}^2}{R^2}, \tag{4.3}$$

$$d_{iB} = \frac{1}{p_{T_i}^2}, \tag{4.4}$$

where p_{T_i} is the transverse momentum of the i-particle, ΔR_{ij}^2 is the angular distance between the two particles and R is a parameter of the algorithm that quantifies the jet size. In this analysis $R = 0.4$ is used.

All possible combinations of particles are evaluated and the minimum between all d_{ij} and all d_{iB} values is searched until no particles are left in the input list of the algorithm. If the minimum value corresponds to the:

- *beam distance* d_{iB}, the corresponding particle i is removed from the input list and defined as a jet candidate,
- *distance between objects* d_{ij}, a new particle with transverse momentum corresponding to the sum of the i and j particles momenta is created and added to the algorithm list.

Identification

In this analysis, reconstructed candidates are considered as jets if they satisfy the following requirements: $|\eta| < 4$, they are associated with at least two tracks, and the energy deposits in the ECAL and HCAL are at least 1% of the candidate total energy.

Energy calibration

The energy of a parton produced in the primary interaction is obtained from the measured jet energy through a factorized approach [127,128]. In particular, a correcting factor C is applied to the four-momentum vector p_i^{raw} of each particle clustered in the jet to obtain the corrected value p_i^{corr}:

$$p_i^{corr} = C \cdot p_i^{raw}.$$

The C factor consists of different components derived from simulation and applied sequentially to p_i^{raw}, i.e the output of each step is the input to the next one. Residual

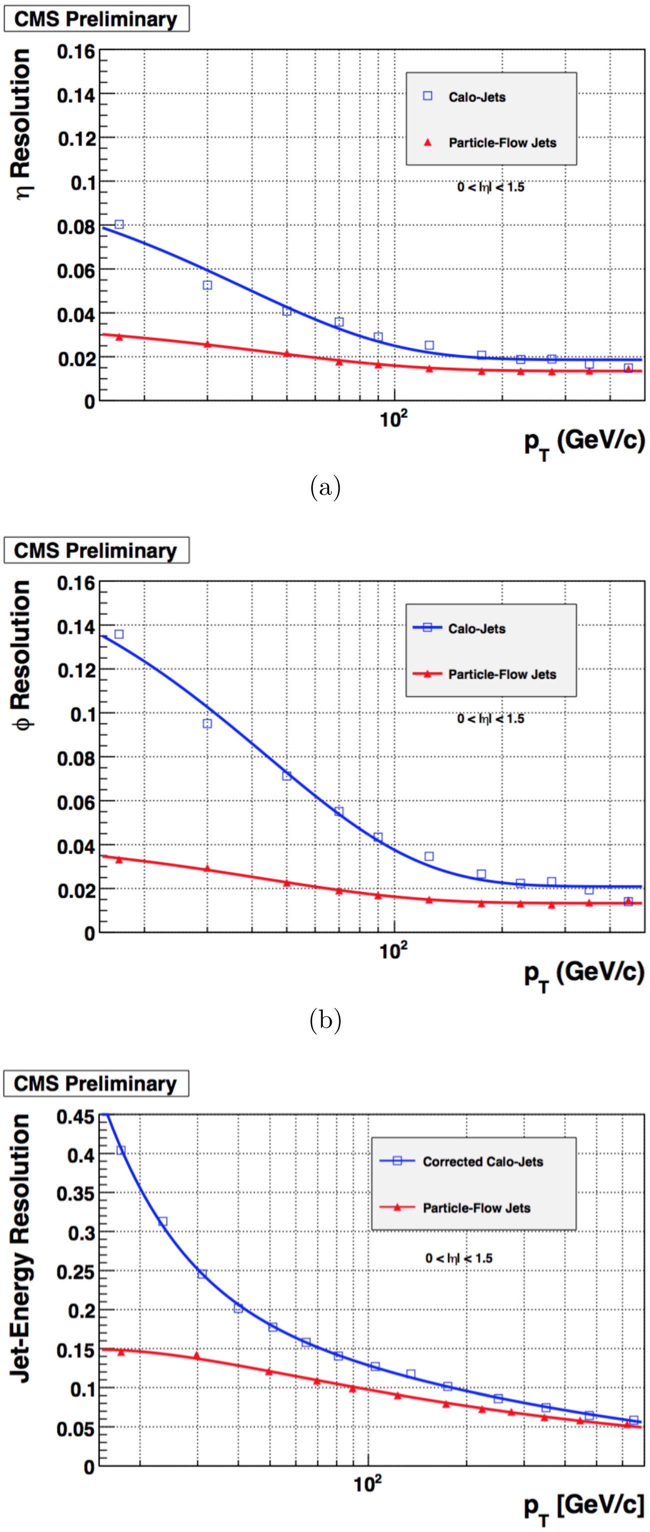

(a)

(b)

(c)

Figure 4.5: Jet $|\eta|$ (a), ϕ (b) and energy (c) resolutions as a function of p_T in the $0 < |\eta| < 1.5$ region. Performances for reconstructed calo-jets (open squares) and for PF-jets (upwards triangles) in simulation are presented [109].

corrections are determined from data to account for differences between the jet response in data and simulation.

The different components included in C are presented in the following in the order in which they are applied [127]:

- C_{offset}, to subtract electronic noise and remaining PU contributions (referred to as "offset"). This correction is applied both to simulation and data;
- C_{MC}, to correct for the jet response dependence on η and p_T due to non-linearity and p_T thresholds in the ECAL and HCAL cluster energies, detector properties, and to geometry effects [128]. This correction is applied both to simulation and data;
- $C_{residual}$, to correct for remaining differences in the jet response in data and simulation as a function of η and p_T. These corrections are of the order of few % and are applied to data only.

After these factorized approach, the average jet response, called jet energy scale (JES), is one within 2% to 8% uncertainties depending on the jet η and p_T [129].

Transverse momentum resolution

The detector resolution for the jet p_T is measured to be smaller in simulation than in data [127, 128]. For this reason, the jet transverse-momentum resolution (JER) in simulation is smeared to match the response observed in data. After corrections, for jets with $|\eta| < 5.0$ and $p_T > 100$ GeV a resolution better than 10% is achieved [129].

Jet energy resolution corrections are applied to jets in the analysis of the 8 TeV dataset. For the data collected at 13 TeV, the correcting factors are found to be negligible and are therefore not applied.

4.2.6 b jets

It is of high importance for the presented analysis, as well as for many new physics searches and SM measurements, to distinguish jets coming from the hadronization of b quarks (b jets) from jets arising from c quarks (c jets), light quarks and gluons (udsg jets).

Bottom hadrons have larger masses, longer lifetimes and daughter particles with larger momentum with respect to other hadron flavours. These peculiar properties are exploited by the Combined Secondary Vertex (CSV) [130] algorithm to identify b jets.

All the variables considered for the b jets discrimination are used as input to a Likelihood Ratio, which is applied once to distinguish between b quark and c quark jets and another time to distinguish between b quark and light quark (gluon) jets. The algorithm provides a continuous output between 0 and 1, where values close to 1 indicate a jet likely to arise from the hadronization of a b quark, as shown in Figure 4.6.

In the CSV b-tagging algorithm, b hadrons secondary vertex candidates are required to satisfy quality criteria to improve the identification of jets from b quarks and to reduce the contamination from vertices due to particle interactions with the detectors or to long-lived mesons [130]. Track-based information are also included, allowing to discriminate jets even if there is no reconstructed secondary vertex in the event.

Efficiency

The performance of the b jet tagging algorithms is based on the probabilities ϵ_b, ϵ_c and ϵ_q to tag correctly a b jet or to misidentify c, light or gluons as b, respectively. These efficiencies are defined as:

$$\epsilon_i = \frac{\#\text{identified as b} - \text{jets}}{\#i\ -\text{jets}};\ i = b, c, q$$

and are shown in Figure 4.6 for simulation as obtained with the CSV algorithm.

Based on the percentage of misidentified light-flavour jets, three different selections for the CSV discriminant are defined: loose ($\epsilon_q \sim 10\%$), medium ($\epsilon_q \sim 1\%$) and tight ($\epsilon_q \sim 0.1\%$) [131, 132]. In the presented analysis the medium selection is used, for which b quarks are tagged with an efficiency of about 69%, and 35% of c quarks are mis-tagged as b quarks. Corrections are applied to simulation to cover differences in efficiency with respect to the performance in data [133].

4.2.7 Missing transverse energy

The missing transverse energy vector is defined as the negative vectorial sum of the transverse momenta p_T of all the PF particles reconstructed in the event [109]:

$$\overrightarrow{E}_T^{miss} = -\sum \overrightarrow{p}_T$$

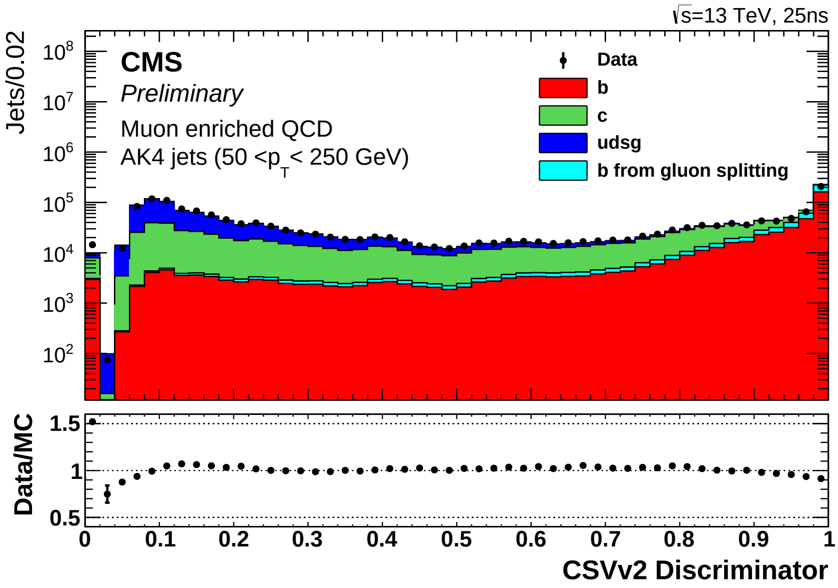

(a)

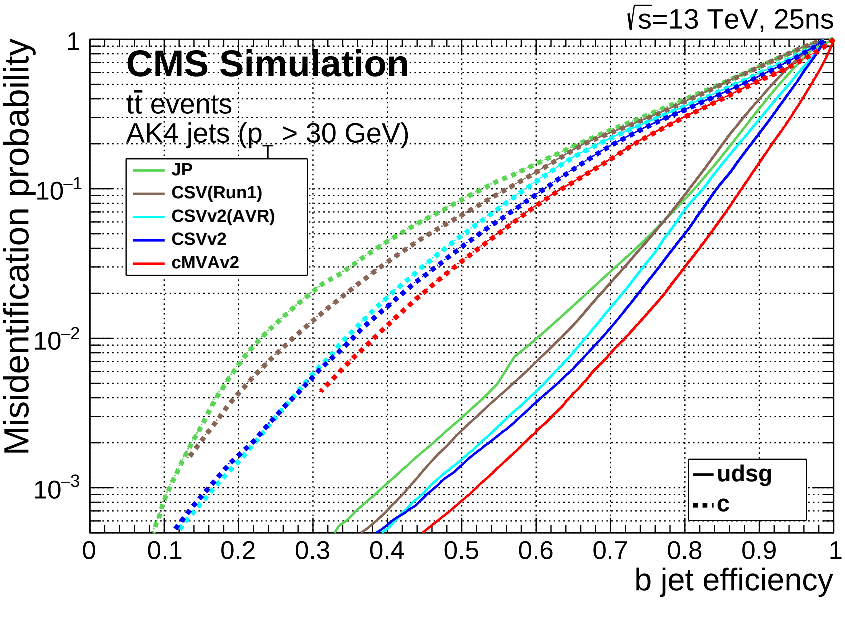

(b)

Figure 4.6: Discriminator distribution for the CSV algorithm (a) shown for an inclusive muon enriched topology with data collected at $\sqrt{s} = 13$ TeV. Underflow and overflow are added to the first and last bins, respectively. The total number of entries in the simulation is normalized to the observed number of entries in data. Performance of CSV b-jet tagging algorithm (light-blue curve) in terms of identification efficiency and mistag rate are shown in (b) [131].

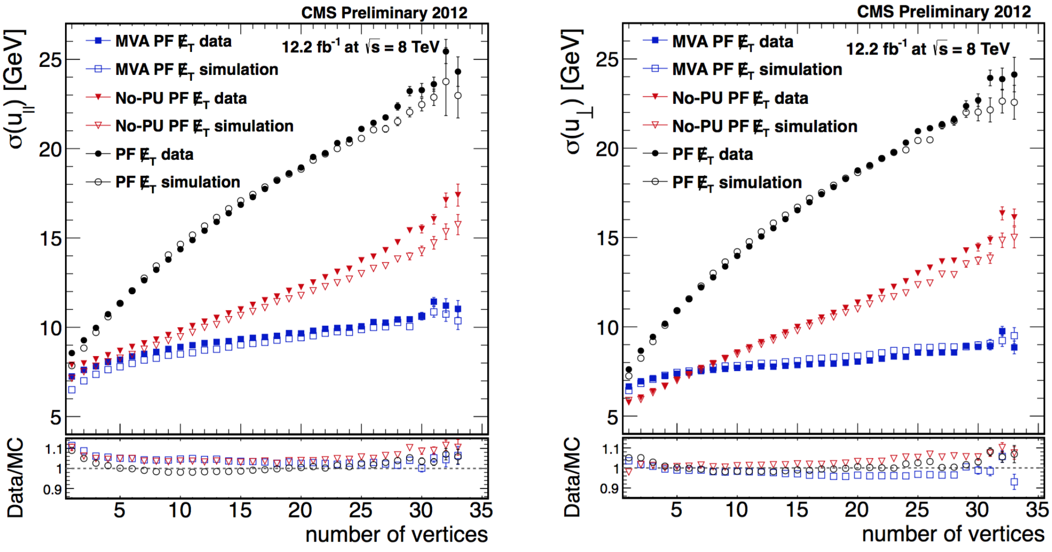

(a) (b)

Figure 4.7: Parallel (a) and perpendicular (b) E_T^{miss} resolution as a function of the number of reconstructed vertices for $Z \rightarrow \mu^+\mu^-$ events in data (black circle) and simulation (white circle) [133]. The E_T^{miss} is reconstructed with the PF algorithm (PF $\not\!\!E_T$ in the plot).

The magnitude of this vector is defined as the missing transverse energy E_T^{miss}.

The estimation of this variable strongly depends on the correct energy and momentum measurements for all the PF objects. To reduce contributions from jet mismeasurements, jet energy-scale corrections are accounted for in the E_T^{miss} calculation. Quality filters are further applied in the analysis to remove events where the E_T^{miss} is severely mis-reconstructed.

The E_T^{miss} variable is extremely important to identify particles, like DM, which escape the detector without interacting with its components. In fact, neglecting momentum mismeasurements, the E_T^{miss} refers to the total transverse momentum of these weakly interacting particles. Its accurate determination also allows to distinguish SM events, where the E_T^{miss} comes from neutrinos, from new physics processes where the missing transverse energy is expected to be higher.

The E_T^{miss} resolution as a function of PU is shown in Figure 4.7 for the 2012 data-taking period [133]. Similar performances are observed in the 2015 data. [134].

Chapter 5

Data analysis

This section describes a search for events in which two top quarks are produced in association with DM candidates. The search has been performed with the data collected by the CMS detector in 2012 and 2015 at a center-of-mass energy of 8 TeV and 13 TeV respectively (referred to as 8 TeV and 13 TeV analyses in the following). The data recorded and good for physics analysis correspond to an integrated luminosity of 19.7 fb^{-1} and 2.2 fb^{-1} for the 2012 and 2015 data-taking period, respectively (see also Section 3.1.1).

The topology of the investigated events consists of two DM particles recoiling against a top quark pair. The DM particles are assumed to escape the detector without decaying and interacting with its components. Therefore, the DM particles are inferred from an imbalance of the transverse momenta. Section 5.1 explains the general characteristics of the DM signal of interest. The SM processes that mimics the kinematics of signal events (background events) are introduced in Section 5.2. The methods used to reject these SM events are presented in Section 5.3.

The analysis of the 2012 data is based on the counting of the observed number of events with respect to the predictions. The 2015 data is analyzed including the use of the shape of the E_T^{miss} distribution in order to improve the sensitivity of the analysis. More details about the two methods are explained in Section 6.2. The source of uncertainties affecting the results are listed in Section 5.3.5.

The following sections are based on [11, 12] and focus on the 13 TeV analysis. Similar techniques are used for the 8 TeV analysis except when outlined.

5.1 Dark matter signal

The signal process under study is characterized by the presence of two top quarks recoiling against two DM particles (tt+DM). Representative Feynman diagrams are shown in Figure 5.1. The two diagrams refer to different descriptions of the interaction between SM and DM particles. An EFT based model was used for the 8 TeV data analysis, while the increase of the center-of-mass energy demanded the use of simplified models for the analysis of the 13 TeV data, as explained in more detail in Sections 2.4.3 and 6.3. In both approaches, the DM is assumed to be a Dirac particle and the mediator to be have spin 0.

In general, the E_T^{miss} spectrum is expected to peak at higher values for signal with respect to SM processes because of the presence of DM particles in the final state. Furthermore, in signal events two top quarks recoil against the DM system. This translates in an azimuthal angle between the high p_T jets from the top quark decay and the E_T^{miss} that is close to π for signal events. These characteristics are presented in more detail in Section 5.3.3.

The produced top quarks decay into a b quark and a W boson before hadronizing. The final state of signal events is based on the decay of these W bosons. This analysis considers the more favorable decay modes:

- *single lepton*: $t\bar{t} \to bW^+(l^+\bar{\nu})\ \bar{b}W^-(q\bar{q})$, or $t\bar{t} \to bW^+(q\bar{q})\ \bar{b}W^-(l^-\nu)$. In these processes, one W boson decays hadronically to a quark q and anti-quark $\bar{q}$ pair and one leptonically to a neutrino ν and a lepton l ($\sim 44\%$ $t\bar{t}$ branching ratio [24]),
- *hadronic*: $t\bar{t} \to bW^+(q\bar{q})\ \bar{b}W^-(q\bar{q})$, both W bosons decay hadronically to quarks ($\sim 46\%$ $t\bar{t}$ branching ratio [24]).

In particular, for the 8 TeV analysis only the single lepton final state is considered, while in the 13 TeV analysis the hadronic channel is also included to increase the signal efficiency. In these analyses only electrons and muons are considered as leptons, lowering the $t\bar{t}$ single lepton branching ratio to $\sim 30\%$. Events where both W bosons decay to a lepton and a neutrino (dilepton) are not considered in this work because of the lower branching ratio with respect to the single lepton and hadronic channels. Dilepton events have been investigated by the CMS collaboration with the data collected at $\sqrt{s} = 8,\ 13$ TeV and the results are presented in [135] and [136], respectively.

Signal events are generated with Madgraph at LO and showered with Pythia, following the procedures in Section 4.1. Differences between the 13 TeV and 8 TeV simulations

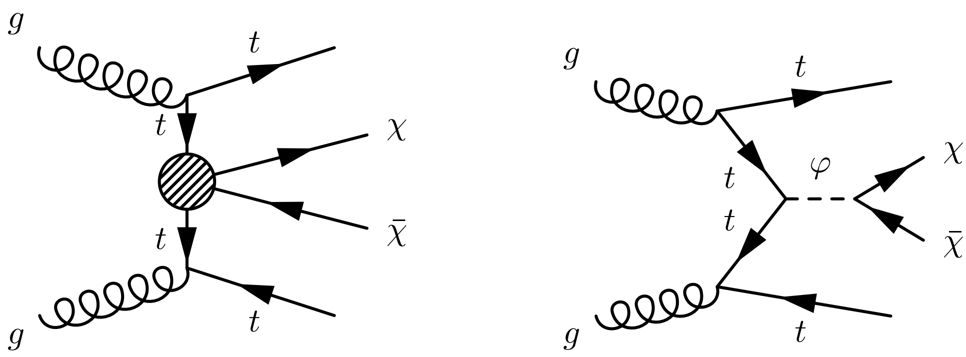

(a) (b)

Figure 5.1: Representative Feynman diagrams describing the associated production of DM particles χ with a pair of top quarks assuming a contact interaction (a) or an explicit scalar or pseudoscalar mediator φ (b).

Process	Matrix element generator	PDF	Showering	Calculation order	Matching/ Merging
$t\bar{t}$	Powheg (v2) [137]	NNPDF (3.0) [138]	Pythia (8.205) [139]	NNLO	-
single top	Powheg (v1) [137]	NNPDF (3.0)	Pythia (8.205)	NLO (t-channel) NNLO (tW-channel)	-
Z+jets W+jets $t\bar{t}+\gamma$ QCD	MG5_aMC@NLO (v2.2.2) [140]	NNPDF (3.0)	Pythia (8.205)	LO	MLM (matching) [141]
$t\bar{t}+W$ $t\bar{t}+Z$	MG5_aMC@NLO (v2.2.2)	NNPDF (3.0)	Pythia (8.205)	NLO	FxFx (merging) [142]
WW WZ ZZ	MG5_aMC@NLO (v2.2.2) or Powheg (v2)	NNPDF (3.0)	Pythia (8.205) -	NLO	-
signal (up to 1 additional parton)	MG5_aMC@NLO (v2.2.2)	NNPDF (3.0)	Pythia (8.205)	LO	MLM (matching)

Table 5.1: Simulation setup used in the 13 TeV analysis for background and signal simulated samples.

are mainly in the choice of PDF used for the hard process calculation. The details of the event generation are summarized in Tables 5.1 and 5.2, which refer to the 13 TeV and 8 TeV analyses respectively. Since the mass of the DM particle and of the mediator are unknown, different hypotheses are considered in the simulation. Each of them is treated as a different search for DM particles.

5.2 Standard model backgrounds

In order to be able to extract from data a small signal it is crucial to have a good modeling and evaluation of all the SM processes that can mimic the signal (referred to as backgrounds). The characteristics of these SM processes are explained in the following sections. A summary of their cross sections at $\sqrt{s} = 8,\ 13$ TeV is presented

Process	Matrix element generator	PDF	Showering	Calculation order
$t\bar{t}$+jets	Madgraph (v5.1.5.11) [140]	CTEQ6L1 [143]	Pythia (v6.424) [103]	NNLO
$t\bar{t}+\gamma$ $t\bar{t}+W$ $t\bar{t}+Z$	Madgraph (v5.1.5.11)	CTEQ6L1	Pythia (v6.424)	NLO
W+jets Z+jets	Madgraph (v5.1.5.11)	CTEQ6L1	Pythia (v6.424)	NNLO
WZ ZZ	Madgraph (v5.1.5.11)	CTEQ6L1	Pythia (v6.424)	NLO
WW	Pythia (v6.424)	CTEQ6L1	-	NLO
single top	Powheg (v1) [137]	CTEQ6M [143]	-	NLO
signal (up to 2 additional parton)	Madgraph (v5.1.5.11)	CTEQ6L1	Pythia (v6.424)	LO

Table 5.2: Simulation setup used in the 8 TeV analysis for background and signal simulated samples.

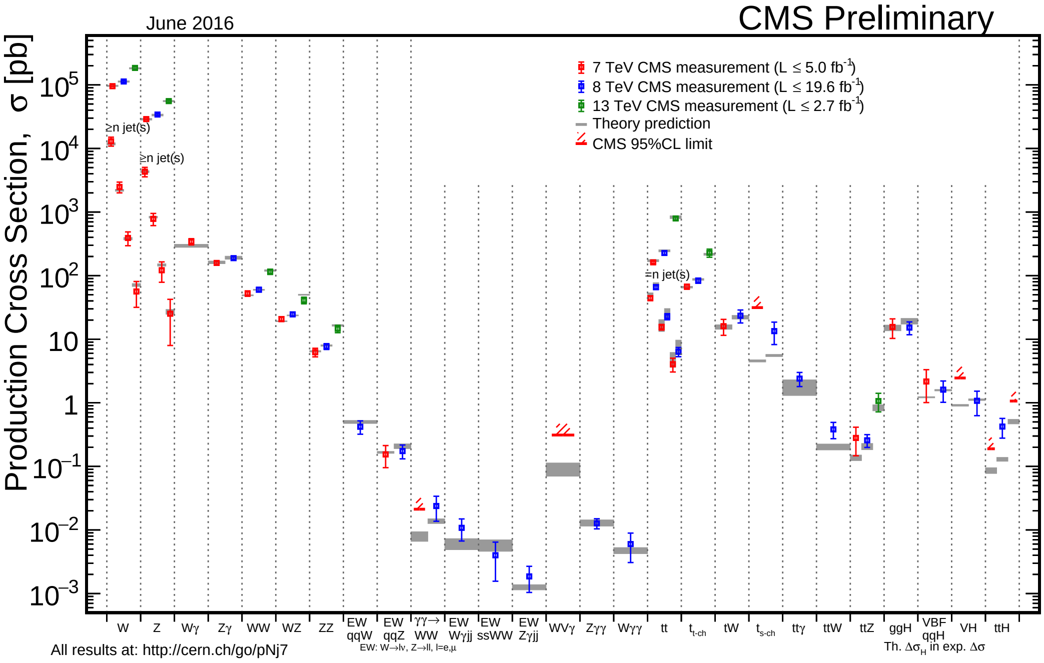

Figure 5.2: Cross sections for various SM processes as predicted by theory and measured by CMS at $\sqrt{s} = 7,\ 8,\ 13$ TeV [144].

in Figure 5.2. The simulation details used for these events are listed in Tables 5.1 and 5.2.

5.2.1 Top quarks

At hadron colliders, top quarks are produced predominantly in pairs through the strong interaction process $gg \to t\bar{t}$ [24]. Single top quarks are produced through electroweak interactions with a cross section at $\sqrt{s} = 13$ (8) TeV about six (two) times smaller than top quark pair events [24], Figure 5.2. Single production is obtained through processes mediated by virtual s-channel or t-channel W bosons, for example $qq' \to t\bar{b}$ and $qb \to q't$ respectively, or through associated production with a W boson, $qq' \to tW^-$. The single top processes are ordered in terms of decreasing cross sections at LHC as t-, tW- and s-channel, Figure 5.2. Top quarks are also produced in association with bosons, $t\bar{t}W$ and $t\bar{t}Z$, with a cross section smaller with respect to the previous processes.

Based on the production and decay mode, background events from top quarks are divided in:

- $t\bar{t}(2l)$: production of $t\bar{t}$ in association with jets in which both W bosons decay leptonically to a neutrino and a lepton, $t\bar{t} \to bW^+(l^+\bar{\nu})\ \bar{b}W^-(l^-\nu)$ ($\sim$ 10% $t\bar{t}$ branching ratio [24]),
- $t\bar{t}(1l)$: production of $t\bar{t}$ in association with jets, where a W boson decay leptonically to a neutrino and a lepton, and the other hadronically to quarks,
- $t\bar{t}$: $t\bar{t}(2l)$ and $t\bar{t}(1l)$ productions,
- *single top*: production of a single top quark through t-, tW-,or s-channel processes,
- ttV: top quark pair associated production with a boson V ($V = W,\ Z,\ \gamma$).

Top quark pair events constitute the main background for both the hadronic and the single lepton channels. In these processes, the main source of E_T^{miss} is the neutrino from the leptonic decay of the W boson and the lepton if it is not detected. Therefore, $t\bar{t}(2l)$ events are the main background for the single lepton channel when one lepton is undetected and fakes a high E_T^{miss} value. For the same reason, $t\bar{t}(1l)$ processes are the main background for the hadronic analysis. If the lepton is detected, events from top quarks processes are distinguished from the signal employing the transverse mass M_T, reconstructed from the lepton momentum p_T^l and the E_T^{miss} as:

$$M_T = \sqrt{2p_T^l E_T^{miss}(1 - cos\Delta\phi_{l,E_T^{miss}})},$$

where $\Delta\phi_{l,E_T^{miss}}$ is the opening angle in the transverse plane between the lepton and the E_T^{miss} vector. This variable does not exceed the W mass m_W value (80.39 GeV) for top quarks events where the W boson is produced on-shell. This and other variables used to reject top quarks events are explained in more detail in Section 5.3.3.

Single top quark and ttV processes constitute a subdominant background due to the lower jet and b jet multiplicities with respect to the signal.

Top quark p_T reweighting

The top quark differential cross section shows that the p_T spectra of leptons and jets from the top quark decay are softer in data than in MC simulation. This is understood to be caused by a mismodeling of the simulated top quark p_T distribution. In order to improve the description of top quark pair events, simulated samples are reweighted to match CMS measurements [145–147].

The distributions of the leading-in-p_T jet and of the lepton transverse momentum are shown in Figure 5.3 before and after the reweight is applied. The distributions are shown for the 8 TeV analysis after requiring: $E_T^{miss} > 160$ GeV, 1 electron or muon, at least 3 jets, and at least 1 jet from b quarks. Applying this selection, signal like events where one of the W bosons decays leptonically and the other hadronically are selected. Similar improvements are observed in the 13 TeV analysis.

5.2.2 Vector bosons plus jets

Vector bosons V (V = W, Z) can be produced in association with light or heavy flavour jets (V+jets). The production cross section decreases of a factor ~ 5 for each jet produced in association with the V boson, Figure 5.2.

In the presented analysis, V+jets events are classified as:

- Z→ ll: Z+jets events in which the Z boson decays leptonically Z→ l^+l^- to two leptons ($\sim 6\%$ Z branching ratio),
- Z→ $\nu\nu$: Z+jets events in which the Z boson decays to two neutrinos, Z→ $\nu\bar{\nu}$ (20% Z branching ratio)

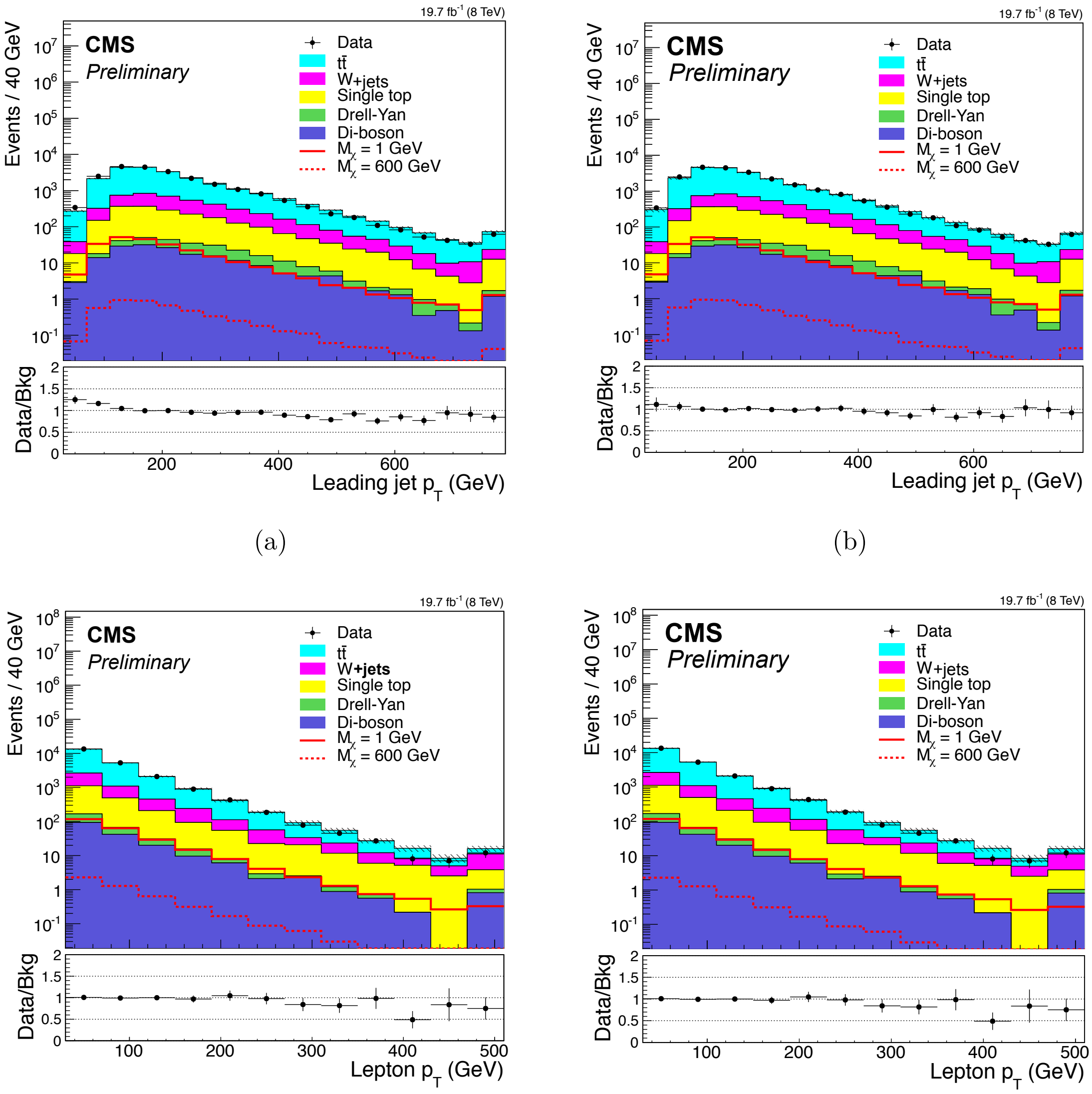

(a)

(b)

(c)

(d)

Figure 5.3: Leading-in-p_T jet p_T distributions before (a) and after (b) applying the top p_T reweighting. Similar distributions are presented for the lepton p_T (c and d). A preselection is applied to select signal like events where one of the W bosons decays leptonically and the other hadronically. The solid histograms for the simulated SM backgrounds are summed cumulatively and rescaled to luminosity, and the grey hatched band represents the associated statistical uncertainty. The data are represented by solid points on which the horizontal bar indicates the width of the bin and the vertical one the associated statical uncertainty. In the lower plots the ratio between data and the total SM background is presented with the associated statistical uncertainty. Two simulated signal models based on the production process of Figure 5.1(b) are also included. The last bin of the distributions includes the overflow. The shown distributions refer to the 8 TeV search.

- Drell-Yan: inclusive Z+jets production,
- W+jets: events in which a W boson is produced in association with jets and decays leptonically (W→ $l\nu$) with a branching ratio of $\sim$ 20% or hadronically (W→ jj) in $\sim$ 67% of the cases.

The production of Z→ $\nu\nu$ is the second largest source of background in the hadronic channel. The presence of two neutrinos in the final state leads to comparable E_T^{miss} to the DM signal. The main handle to reject Z+jets background events is the lower jet multiplicity with respect to tt+DM processes.

Events from W+jets constitutes one of the leading backgrounds in the single lepton channel, together with top quark events. In fact, high E_T^{miss} (above 160 GeV) is achieved by the presence of the neutrino in the leptonic decay of the W boson together with jet mismeasurements. As for the case of *tt(1l)* events, the M_T distribution helps in rejecting the W+jets background. Only events where the W boson is produced off-shell will have an end point in the M_T distribution above the m_W.

Higher order corrections

In the 13 TeV analysis, the cross section for V+jets events is calculated at LO, Table 5.1. The information from NLO electroweak and QCD calculations is enclosed in so-called k-factors, which are defined as the ratio of the NLO to LO cross sections. The k-factors used are calculated with MG5_aMC@NLO (v2.2.2) as function of the generated vector boson p_T. The results of the calculation are presented in Table 5.3. The EWK and QCD k-factors are assumed to factorize and are therefore applied to the simulated samples as a product.

5.2.3 Dibosons

Vector bosons VV (V = W, Z) are produced in pair through electroweak processes, and are considered inclusively as:

- VV (diboson): WZ, WW, and ZZ production of dibosons pair.

These processes constitutes a subdominant background in both the hadronic and the single lepton channels. This is due to their lower jet and b-jet multiplicity with respect to signal events.

$p_T(V)$ (GeV)	W+jets		Z+jets	
	EWK	QCD	EWK	QCD
<150	0.980859	1.89123	0.984525	1.685005
[150-200]	0.962119	1.70414	0.969079	1.552560
[200-250]	0.944429	1.60726	0.954627	1.522595
[250-300]	0.927686	1.57206	0.941059	1.520624
[300-350]	0.911802	1.51689	0.928284	1.432282
[350-400]	0.8967	1.4109	0.91622	1.457417
[400-500]	0.875368	1.30758	0.899312	1.368499
[500-600]	0.849097	1.32046	0.878693	1.358024
>600	0.792159	1.26853	0.834718	1.164847

Table 5.3: Electroweak (EWK) and QCD NLO/LO k-factors for W+jets and Z+jets processes as calculated in MG5_aMC@NLO (v2.2.2) as function of generated boson p_T.

5.2.4 QCD production of jets

The QCD production of jets (multijet) has a higher cross section with respect to the other SM processes, for example at $\sqrt{s} = 13$ TeV $\sigma_{QCD} \sim 10^6\ \sigma_{t\bar{t}}$. Nevertheless, multijet processes constitute a negligible background for the analysis. In the single lepton channel, this is due to the lack of isolated leptons in multijet events. Jets missed or mis-measured are the source of E_T^{miss} in multijet processes and the ϕ opening between jets and E_T^{miss} tends to be smaller with respect to signal events. For these reasons, the multijet background can be reduced to a negligible amount also in the hadronic channel.

In the analysis, the following naming is used:

- *QCD*: multijet QCD production.

5.2.5 Pileup reweighting

The simulation does not reproduce the PU observed in data. In order to remove this discrepancy simulated samples are corrected.

A cross section of 69 (69.4) mb for minimum bias events is used to estimate the number of PU interactions during the 2015 (2012) data-taking. In Figure 5.4, this PU distribution is shown together with that obtained from simulation. From the ratio of the two normalized distributions, scaling factors to be applied to the simulation on an event-by-event basis are derived. A variation of ±5% on the minimum-bias cross section is used to cover uncertainties on the PU modeling.

A closure test is performed comparing the number of reconstructed vertices in data and

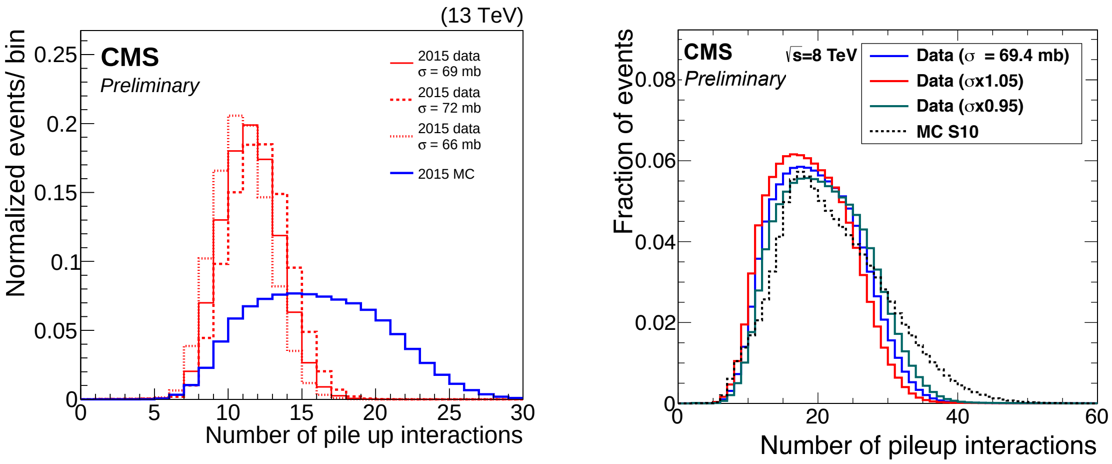

(a)

(b)

Figure 5.4: Normalized PU scenario from uncorrected simulation compared with the the normalized distribution observed in 2015 (a), 2012 (b) data. The distributions with ±5% variation on the minimum bias cross-section used to estimate the PU scenario in data are also shown.

simulation before and after the PU re-weighting. As an example, these distributions are shown for the 13 TeV analysis in Figure 5.5. The number of reconstructed vertices is shown after basic requirements on the number of jets, b-tagged jets, leptons, and on E_T^{miss}. The employed selections identify the single lepton and hadronic final states, Section 5.3.2. A better agreement between data and simulation is obtained after the PU weights are applied, both in the 13 TeV and in the 8 TeV analyses.

5.3 Data analysis

The data used in this search are collected requiring events to pass either a single lepton or a $E_T^{miss} > 120$ GeV trigger. The details of the trigger selection are presented in Table 5.4. The same requirements are also employed for simulated samples.

Corrections are applied to MC simulation to take into account disagreements between data and simulation trigger efficiencies.

5.3.1 Strategy

The strategy for this search is to define a region, called signal region (SR), where tt+DM events are enhanced with respect to SM backgrounds. The identification of such SR is based on MC simulation and exploits the kinematic differences between

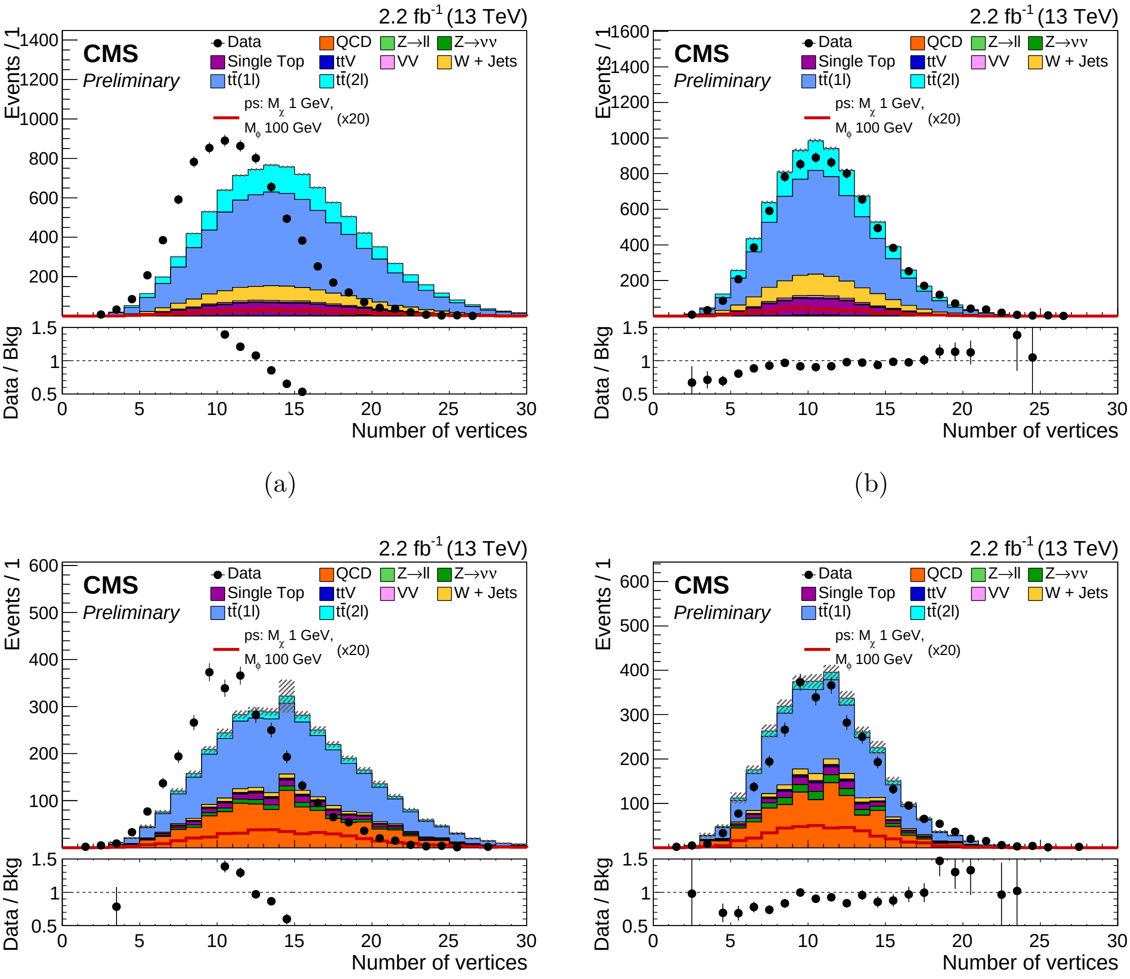

(a) (b)

(c) (d)

Figure 5.5: Distribution of the number of reconstructed vertices in data and simulation before and after the pileup re-weighting after basic requirements on the number of jets, b-tagged jets, leptons and missing transverse energy in the events which identify the single lepton (a and b respectively) and hadronic final states (c and d respectively). The solid histograms for the simulated SM backgrounds are summed cumulatively and rescaled to luminosity and the grey hatched band represents the associated statistical uncertainty. The data are represented by solid points on which the horizontal bar indicates the width of the bin and the vertical one the associated statical uncertainty. In the lower plots the ratio between data and the total SM background is presented with the associated statistical uncertainty. One simulated signal model based on the production process of Figure 5.1(a) is also included.

Trigger	Selection 13 TeV	 8 TeV
single-muon	1 muon with $p_T > 20$ GeV	1 muon with $p_T > 24$ GeV $\|\eta\| < 2.1$
single-electron	1 electron with $p_T > 20$ GeV $\|\eta\| < 2.1$	1 electron with $p_T > 27$ GeV
E_T^{miss}	$E_T^{miss} > 120$ GeV	–

Table 5.4: Trigger event selection used for the 8 TeV and 13 TeV analyses.

signal and background events. The variables used in the SR selection are explained in detail in Sections 5.3.2 and 5.3.3.

After defining a SR, the background contributions are evaluated from simulation for the subdominant SM processes and from data for the dominant backgrounds. In the data-driven approach, so-called control regions (CR) enriched in a specific SM process are identified. A CR is defined such that is as kinematically close as possible, but does not overlap with the SR, and has sufficient event statistics. The definition of the background enriched regions used in the analysis is presented in Section 5.3.4. In the CRs the background normalization is obtained matching the simulation to the observed data and this estimate is then extrapolated to the SR. The data-driven background estimation is explained in more detail in Section 5.3.4.

Finally, results in terms of DM particles production are extracted. Different methods are used in the 8 TeV and 13 TeV analyses. In the former, the results are extracted counting the observed number of events with respect to the predictions. In the latter, a simultaneous fit of the E_T^{miss} distributions in SR and CRs is performed. This technique increases the sensitivity of the analysis exploiting the differences in E_T^{miss} shape between signal and background processes. These methods are explained in Section 6.1 and 6.2.

5.3.2 Event preselection

A preselection is applied to select events with single lepton and hadronic final states. The requirements are based on the number of jets, b jets, leptons, and on the E_T^{miss} as presented in the following. After this selection, the background composition of each channel can be identified and kinematic differences between signal and background events exploited to define a SR. In addition, the preselection requirements are defined to assure high (above 90%) trigger efficiencies and to reject low E_T^{miss} values (< 160

GeV) due to detector mis-measurements.

In the **single lepton channel preselection** events are required to:

- pass the single-muon or single-electron trigger selection, and to have
- 1 lepton (electron or muon) with $p_T > 30$ GeV, $|\eta| < 2.1$, and that satisfies tight identification criteria (Sections 4.2.3 and 4.2.4),
- 0 additional leptons (electrons or muons) with $p_T > 10$ GeV, $|\eta| < 2.4$, and satisfying the loose (veto) identification criteria if they are muons (electrons) (Sections 4.2.3 and 4.2.4),
- ≥ 3 jets with ≥ 1 b jets; with $p_T > 30$ GeV, $|\eta| < 4$ for jets and $p_T > 30$ GeV, $|\eta| < 4$ for b jets,
- $E_T^{miss} > 160$ GeV,

with the requirements on the leptons ensuring a trigger efficiency above 90%. The presented preselection reduces SM backgrounds from V+jets and QCD processes.

In signal events, at least four jets are expected from the decay of the two top quarks. In the preselection, ≥ 3 jets are required because this looser selection is found to improve the signal sensitivity of the single lepton channel by about 10%.

The **hadronic channel preselection** requires events to:

- pass the E_T^{miss} trigger selection, and to have
- 0 leptons (electrons or muons) with $p_T > 10$ GeV, $|\eta| < 2.4$ and satisfying the loose (veto) identification criteria if they are muons (electrons),
- ≥ 4 jets with ≥ 2 b jets; with $p_T > 30$ GeV, $|\eta| < 4$ for jets and $p_T > 30$ GeV, $|\eta| < 4$ for b jets,
- $E_T^{miss} > 200$ GeV,

with the selection on the E_T^{miss} guaranteeing a trigger efficiency of $\sim$ 100%. The hadronic preselection requirements reduce SM backgrounds from QCD events.

The distributions of the jets and b jets multiplicities, of the p_T of the two jets with highest momentum, and of the E_T^{miss} are presented in Figures 5.6 and 5.7 for the single lepton and hadronic channels after preselection. In the single lepton channel, the lepton momentum distribution is also shown. A discrepancy is observed between data and simulation for the jet and b jet multiplicities. It is understood to be related to the mismodeling of radiated jet energies, causing the simulated hadronic activity to be higher than in data. This discrepancy affects only the normalization of the final distribution and is therefore corrected by the simultaneous fit, Section 6.2. In the 8 TeV analysis, the modeling of the jets and b jets multiplicities is not affected by this problem.

5.3.3 Signal region and discriminating variables

After preselection, the dominant SM backgrounds in the single lepton channel are from top and W+jets events. The QCD multijet contribution is negligible because of the requirement of one isolated lepton with $p_T > 30$ GeV, $E_T^{miss} > 160$ GeV and of 1 b jet. In the hadronic channel, $t\bar{t}$ and V+jets events contribute the most to the background composition after preselection.

To improve the search sensitivity additional event selections are applied in both channels. These further requirements are based on discriminating variables for which the distributions of signal and backgrounds are different. In the following, the variables used in the single lepton and hadronic channels are introduced as well as the selection applied.

Single lepton channel

- *Transverse mass M_T*: is kinematically constrained to m_W for on-shell decays of the W boson in $t\bar{t}$ and W+jets events, as introduce in Section 5.2. The m_W value is exceeded in signal events, because the E_T^{miss} comes from the DM particles and from the neutrino of the W boson leptonic decay. It is exceeded also in $t\bar{t}$ and W+jets events where the W boson is off-shell. This is shown in Figures 5.9(a) and 5.10(a) for the 13 TeV and 8 TeV analyses, respectively.

- M_{T2}^W: assuming that two identical particles decay into a b quark and a W boson, and that the measured E_T^{miss} is shared among the two decay chains, the minimal value of the mass of such particles can be estimated. The M_{T2}^W variable is defined as the minimal mass value for the decaying particle compatible with the assumed event topology and daughters masses [148]:

$$M_{T2}^W = \min_{\bar{p}_1, \bar{p}_2} \left\{ m_y : \left[\begin{array}{r} \vec{p}^{\,T}_1 + \vec{p}^{\,T}_2 = \vec{E}^T_{miss},\, \bar{p}_1^2 = 0,\, (\bar{p}_1 + \bar{p}_\ell)^2 = \bar{p}_2^2 = m_W^2, \\ (\bar{p}_1 + \bar{p}_\ell + \bar{p}_{\mathrm{b}_1})^2 = (\bar{p}_2 + \bar{p}_{\mathrm{b}_2})^2 = m_y^2 \end{array} \right] \right\} \quad (5.1)$$

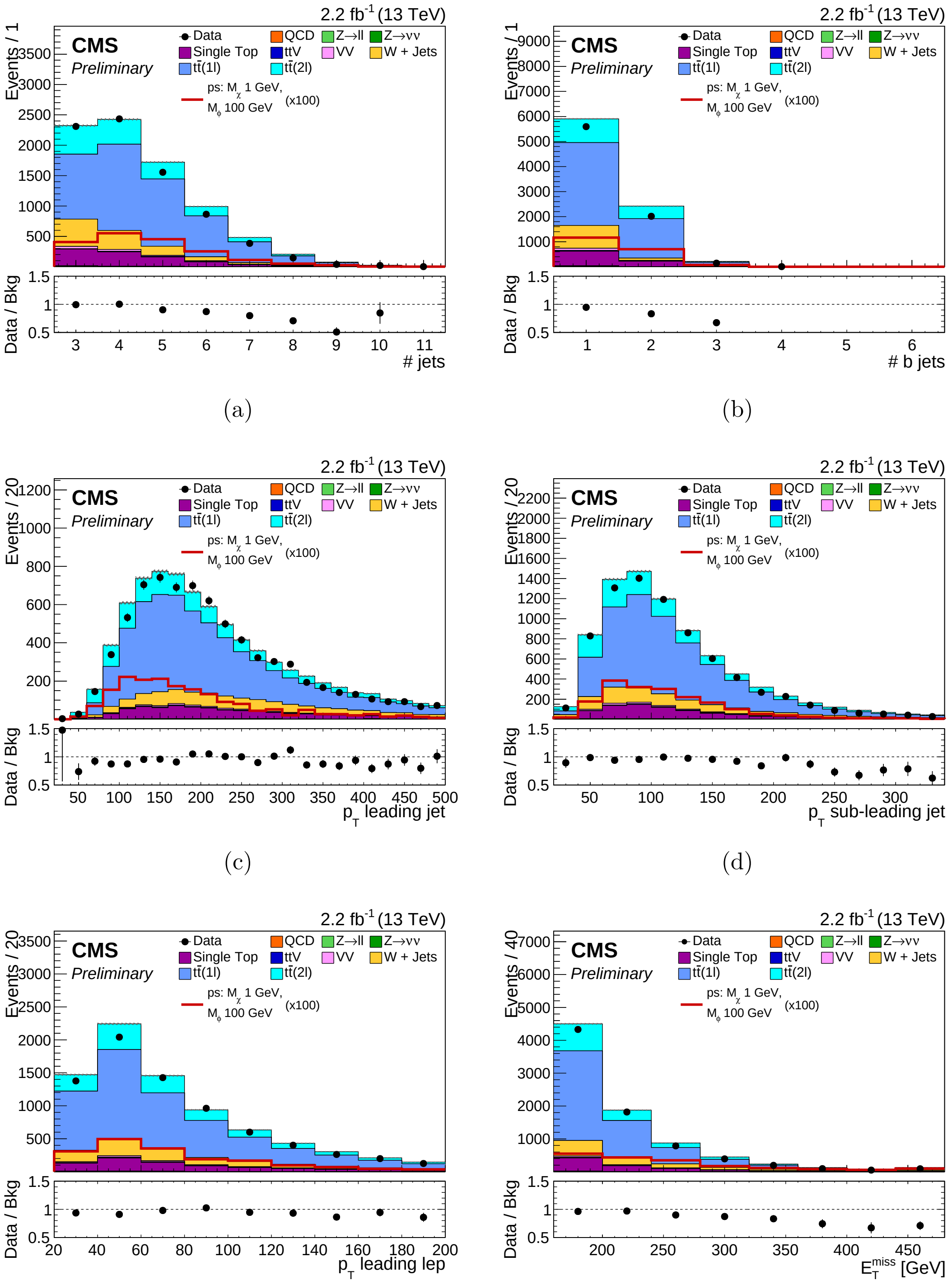

(a) (b)

(c) (d)

(e) (f)

Figure 5.6: Distributions of the number of jets and b-tagged jets, of the p_T of the leading-, trailing-in-p_T jets, of the lepton and of E_T^{miss} for the 13 TeV single lepton channel after preselection. The solid histograms for the simulated SM backgrounds are summed cumulatively and rescaled to luminosity and the grey hatched band represents the associated statistical uncertainty. The data are represented by solid points on which the horizontal bar indicates the width of the bin and the vertical one the associated statical uncertainty. In the lower plots the ratio between data and the total SM background is presented with the associated statistical uncertainty. One simulated signal model based on the production process of Figure 5.1(a) is also included for comparison.

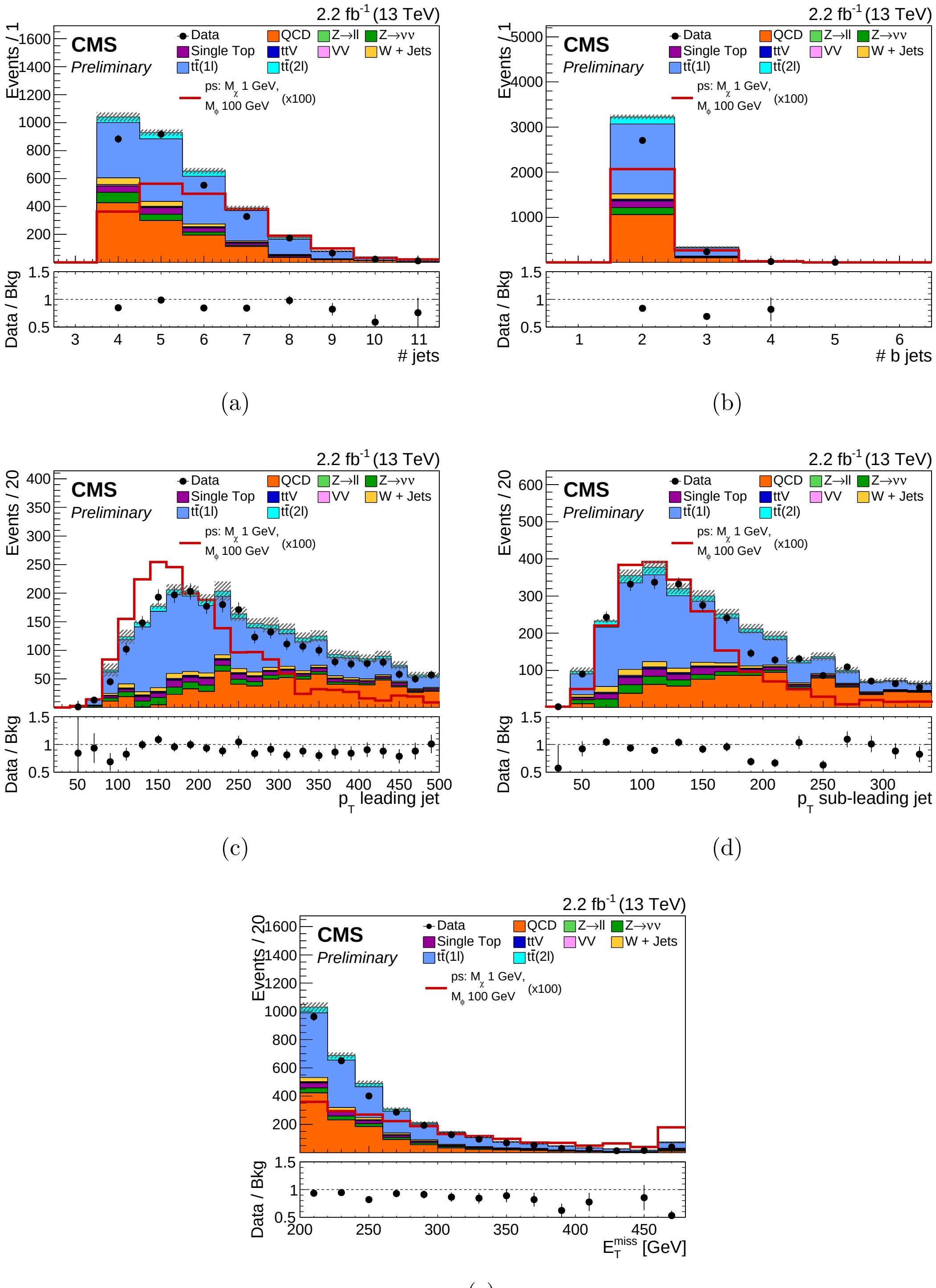

(a) (b) (c) (d) (e)

Figure 5.7: Distributions of the number of jets and b-tagged jets, of the p_T of the leading-, trailing-in-p_T jets, of the lepton and of E_T^{miss} for the 13 TeV hadronic channel after preselection. The solid histograms for the simulated SM backgrounds are summed cumulatively and rescaled to luminosity. The grey hatched band represents the associated total uncertainty. The data are represented by solid points on which the horizontal bar indicates the width of the bin and the vertical one the associated statical uncertainty. In the lower plots the ratio between data and the total SM background is presented with the associated statistical uncertainty. One simulated signal model based on the production process of Figure 5.1(a) is also included for comparison.

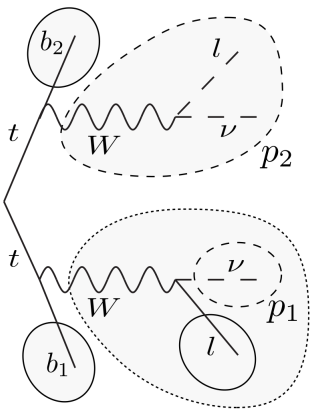

Figure 5.8: Illustration of a $t\bar{t}(2l)$ event where one of the leptons from the W boson decay is unobserved. In the presented diagram p_2 indicates the momentum of the W boson that decays into an undetected electron and p_1 the momentum of the neutrino from the leptonic decay of the other W boson. The same notation is used in Equation 5.1 [148].

where the E_T^{miss} is decomposed into the vectors $\vec{p}\,_1^T$ and $\vec{p}\,_2^T$, as also shown in Figure 5.8. One of the two W bosons, with momentum $\vec{p}\,_2^T$, is assumed to decay into an unreconstructed electron and a neutrino. Both W bosons are assumed to be on-shell.

The undetected lepton gives rise to $E_T^{miss} > 160$ GeV and $M_T > m_W$. As a consequence, $t\bar{t}(2l)$ events are the dominant background for the single lepton channel. The M_{T2}^W variable rejects $t\bar{t}$ events in which both W bosons decay leptonically but one of the leptons is unobserved, as illustrated in Figure 5.8. For $t\bar{t}$ events, the M_{T2}^W distribution has a kinematic end-point at the mass of the top quark if mismeasurements from the detector are ignored. This is not the case for signal events where the E_T^{miss} is also due to the DM particles, as can be seen in Figures 5.9(b) and 5.10(b). The calculation of the M_{T2}^W requires two b jets in the event for the minimization procedure. If only one b jet is identified, the first three jets with highest p_T are considered as second b jet candidate. In case of more than two b jets in the event, all possible combinations of jets and b jets are considered.

- $\Delta\phi(j_{1,2}, E_T^{miss})$ or $min\Delta\phi(j_{1,2}, E_T^{miss})$: evaluates the minimum opening angle in the transverse plane between the two highest p_T jets and the E_T^{miss} vector. In $t\bar{t}$ events, the E_T^{miss} from the neutrino tends to be more collinear to the jets with the highest p_T. This because they are likely to come from the decay of the same top quark. For signal processes, the $\Delta\phi(j_{1,2}, E_T^{miss})$ tends to higher values in case

Variables	*Single lepton signal region* 8 TeV	*Single lepton signal region* 13 TeV	*Hadronic signal region* 13 TeV
preselection			
leptons	$= 1$	$= 1$	$= 0$
jets	≥ 3	≥ 3	≥ 4
b jets	≥ 1	≥ 1	≥ 2
E_T^{miss}	> 160 GeV	> 160 GeV	> 200 GeV
discriminating variables			
M_T	> 160 GeV	> 160 GeV	–
M_{T2}^W	> 200 GeV	> 200 GeV	–
$\Delta\phi(j_i, E_T^{miss})$	$i = 1, 2;$ > 1.2	$i = 1, 2;$ > 1.2	$i = 1, .., 6;$ > 1
additional E_T^{miss} selection	–	> 320 GeV	–

Table 5.5: Overview of the preselection and requirements on the discriminating variables used to define the signal regions for the single lepton (8 TeV and 13 TeV) and hadronic (13 TeV) channels.

of back-to-back production of the DM particle with respect to the $t\bar{t}$ system, as shown in Figures 5.9(d) and 5.10(d) for the 13 TeV and 8 TeV searches.

The selection criteria for the discriminating variables are optimized, after preselection, to increase the significance for various DM signals. The same SR requirements are used in the 8 TeV and 13 TeV analyses with the exception of the E_T^{miss} variable, as presented in Table 5.5.

The distributions of M_T, M_{T2}^W, and $\Delta\phi(j_{1,2}, E_T^{miss})$ are shown in Figure 5.11 and 5.12 after the SR selection is applied except for the requirement on the plotted variable. This shows the discrimination power of each variable between tt+DM signal and SM backgrounds.

Hadronic channel

- $\Delta\phi(j_{1,..,6}, E_T^{miss})$: evaluates the minimum opening angle in the transverse plane between the 6 highest p_T jets and the E_T^{miss} vector. Considering up to 6 jets for the computation of this variable, instead of two as for the single lepton case, improves the search sensitivity of the hadronic channel. The $\Delta\phi(j_{1,..,6}, E_T^{miss})$ variable helps discriminating the tt+DM signal against $t\bar{t}$ events where the E_T^{miss} is typically aligned with a b jet. It also rejects QCD multijet events in which the E_T^{miss} from jet mismeasurements is collinear with other hadronic activity. For signal processes the $\Delta\phi(j_{1,2}, E_T^{miss})$, as for the single lepton channel, tends to higher value with respect to the SM background, as presented in Figures 5.13.

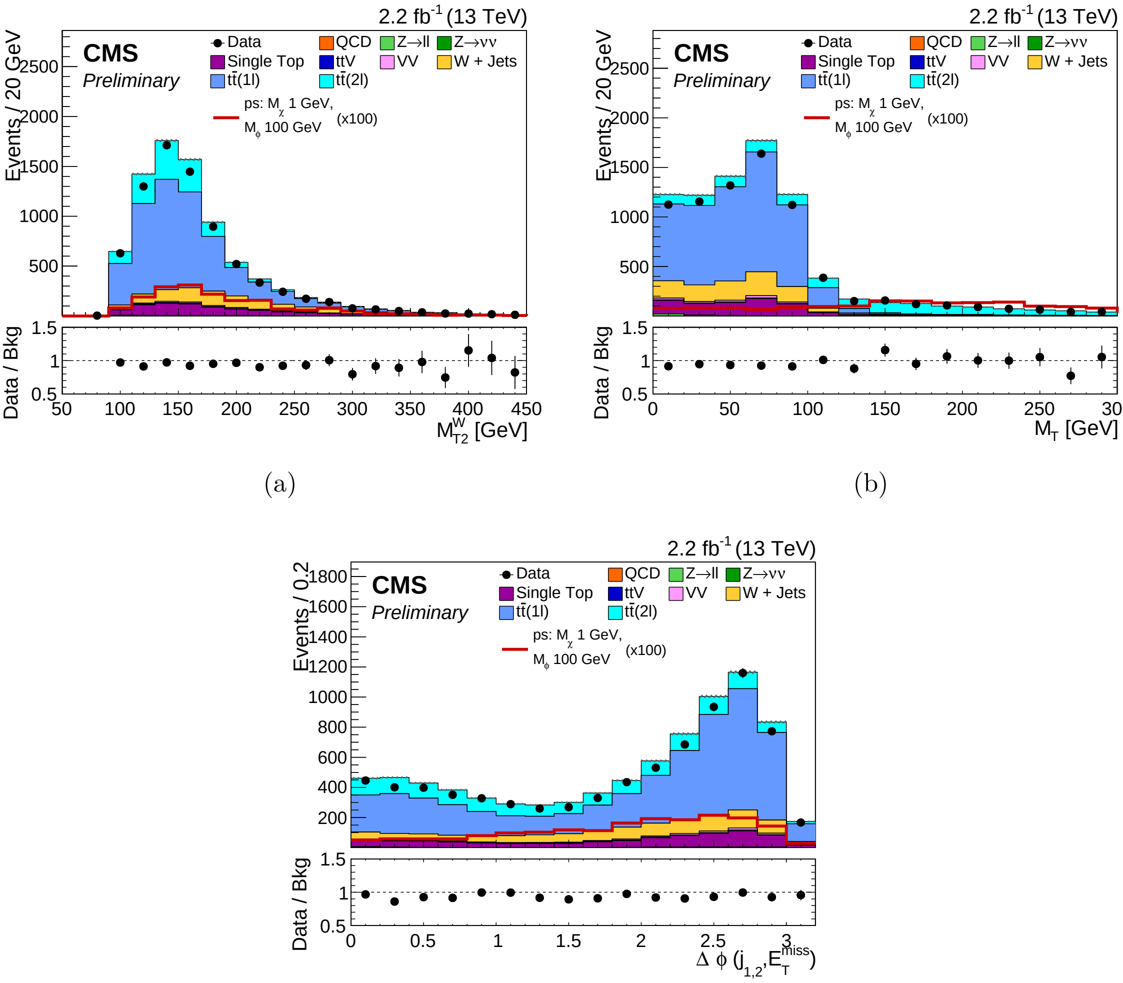

(a)

(b)

(c)

Figure 5.9: Distributions of M_T (a), M_{T2}^{W} (b) and $\Delta\phi(j_{1,2}, E_T^{miss})$ (c) after applying the single lepton preselection for the 13 TeV analysis. The solid histograms for the simulated SM backgrounds are summed cumulatively and rescaled to luminosity and the grey hatched band represents the associated statistical uncertainty. The data are represented by solid points on which the horizontal bar indicates the width of the bin and the vertical one the associated statical uncertainty. In the lower plots the ratio between data and the total SM background is presented with the associated statistical uncertainty. One simulated signal model based on the production process of Figure 5.1(a) is also included for comparison.

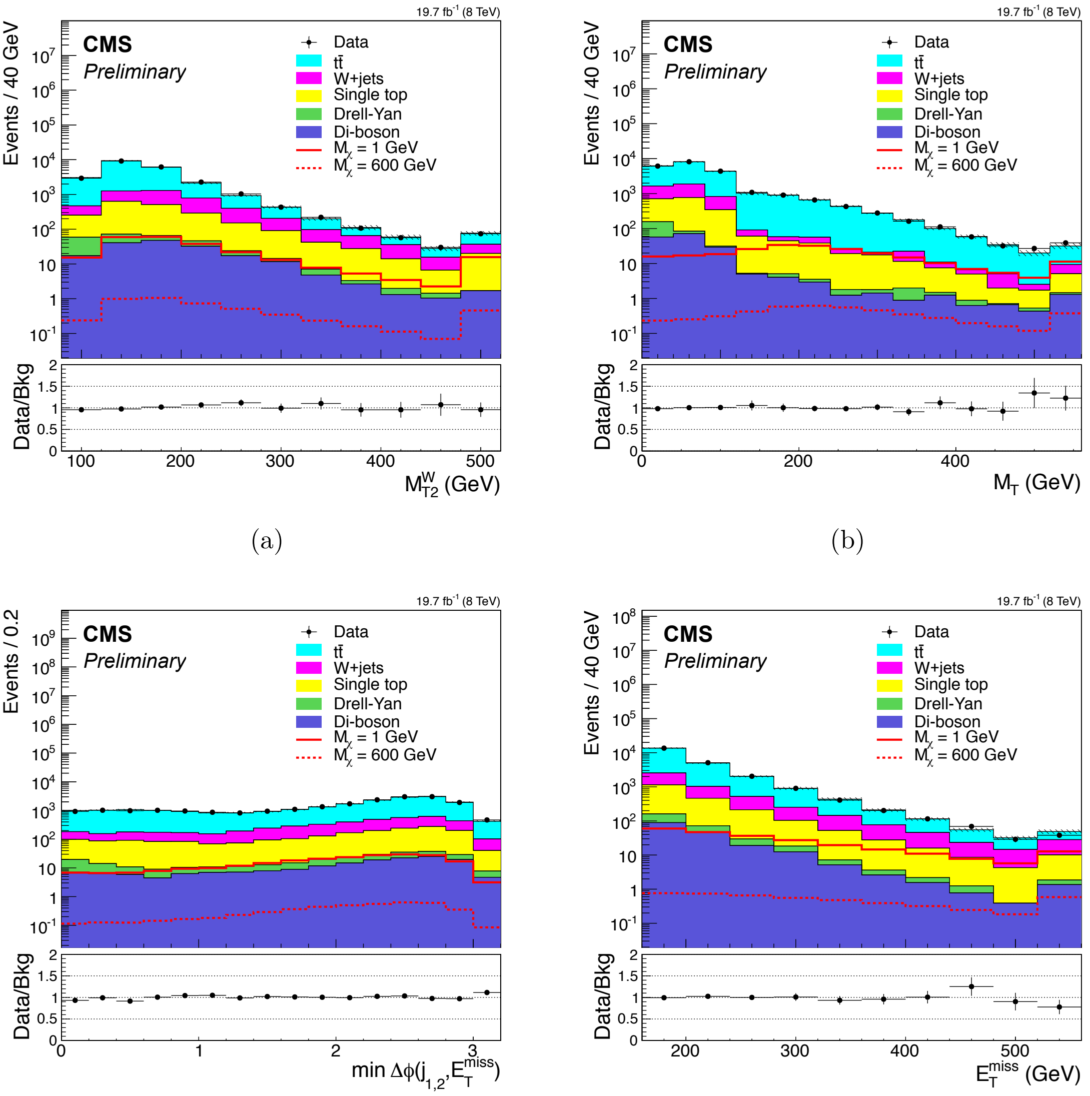

(a) (b)

(c) (d)

Figure 5.10: Distributions of M_T (a), M_{T2}^W (b), $\Delta\phi(j_{1,2}, E_T^{miss})$ (c) and E_T^{miss} (d) after applying the single lepton preselection for the 8 TeV analysis. The solid histograms for the simulated SM backgrounds are summed cumulatively and rescaled to luminosity and the grey hatched band represents the total uncertainty in the background prediction. The data are represented by solid points on which the horizontal bar indicates the width of the bin and the vertical one the associated statical uncertainty. In the lower plots the ratio between data and the total SM background is presented with the associated statistical uncertainty. Two simulated signal models based on the production process of Figure 5.1(b) are also included for comparison.

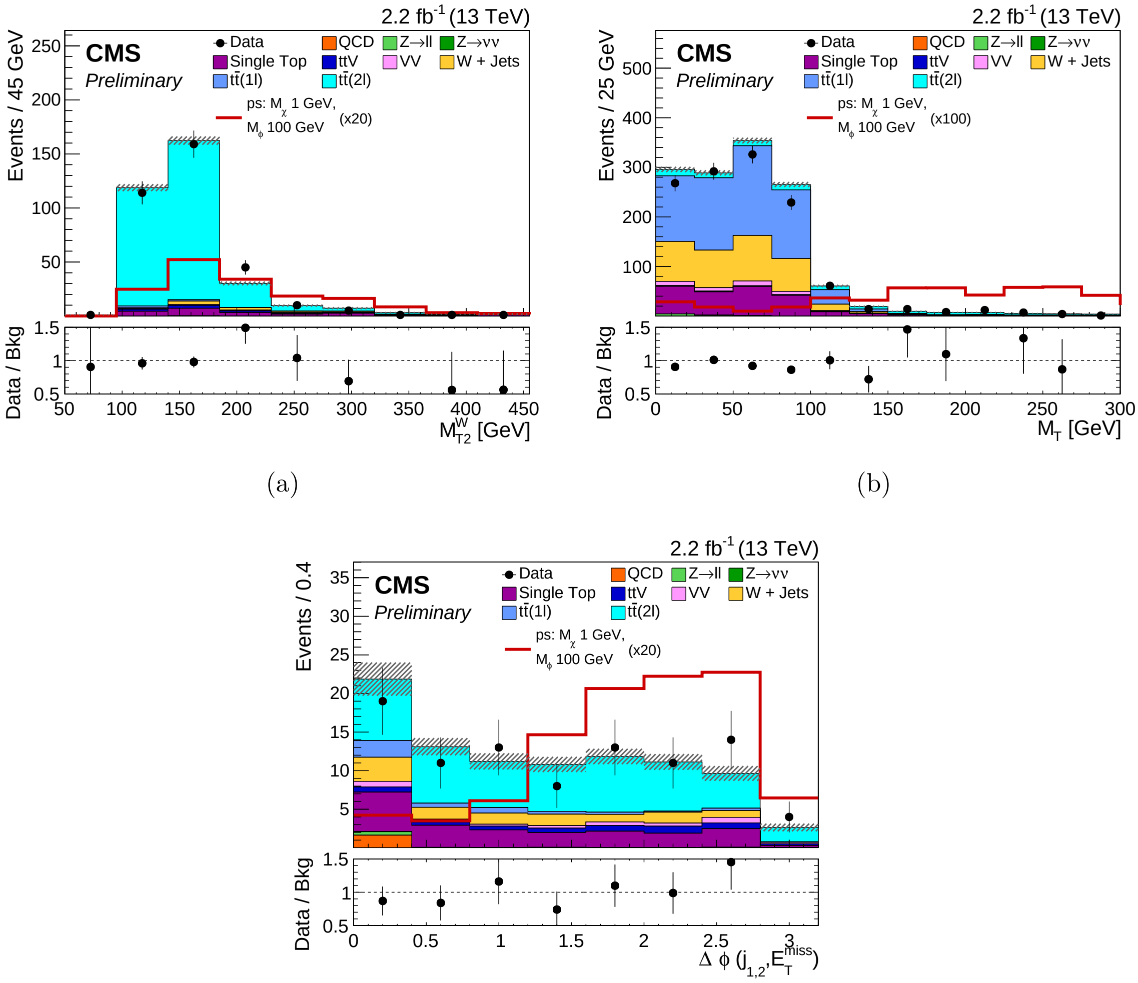

(a) (b)

(c)

Figure 5.11: Distributions for the 13 TeV analysis of M_T (a), M_{T2}^W (b) and $\Delta\phi(j_{1,2}, E_T^{miss})$ (c) after applying the SR selection except the requirement on the shown variable. The solid histograms for the simulated SM backgrounds are summed cumulatively and rescaled to luminosity and the grey hatched band represents the associated statistical uncertainty. The data are represented by solid points on which the horizontal bar indicates the width of the bin and the vertical one the associated statical uncertainty. In the lower plots the ratio between data and the total SM background is presented with the associated statistical uncertainty. One simulated signal model based on the production process of Figure 5.1(a) is also included for comparison.

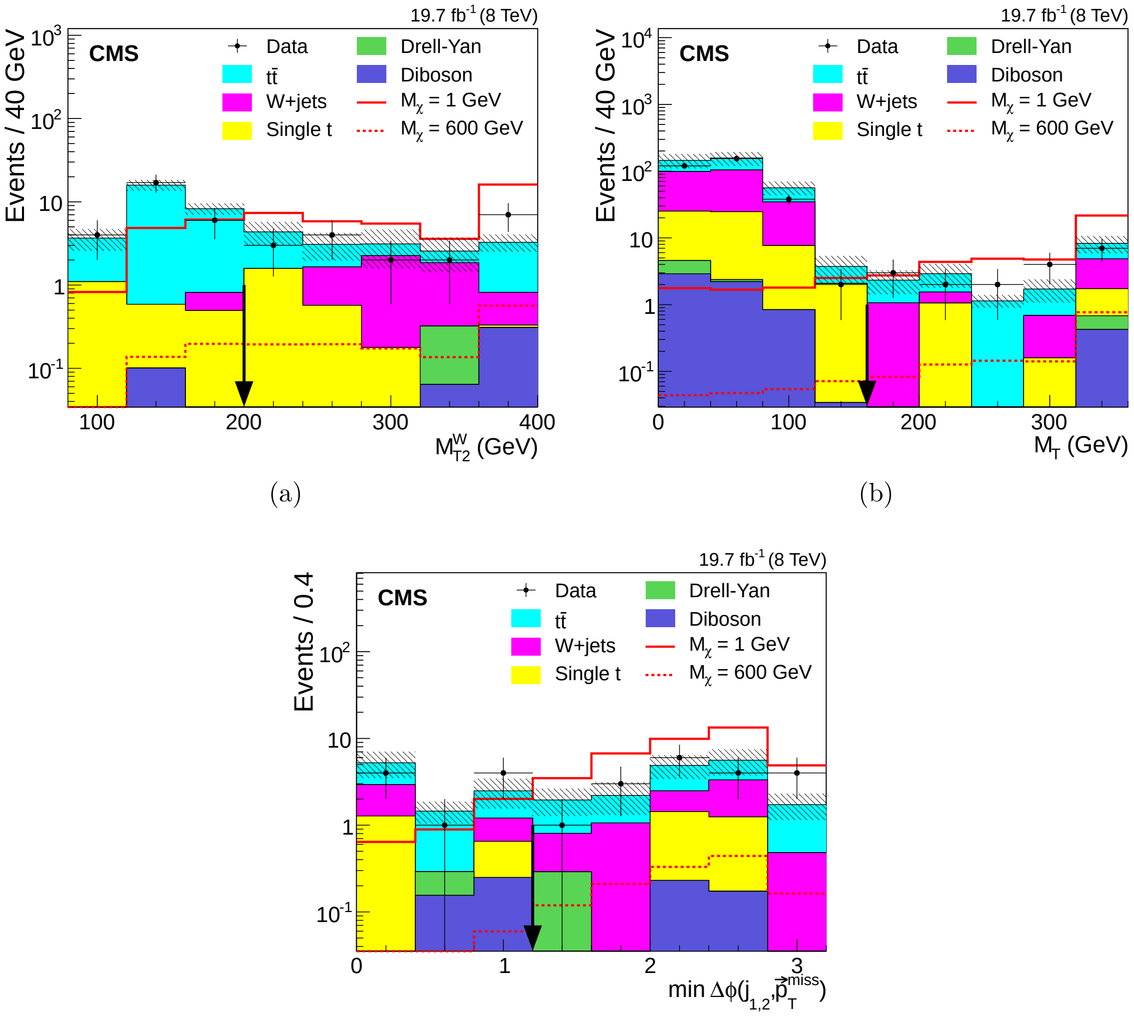

(a)

(b)

(c)

Figure 5.12: Distributions for the 13 TeV analysis of M_T (a), M_{T2}^W (b), and $\Delta\phi(j_{1,2}, E_T^{miss})$ (c) after applying the SR selection except the requirement on the shown variable. The solid histograms for the simulated SM backgrounds are summed cumulatively and rescaled to luminosity and the grey hatched band represents the total uncertainty in the background prediction. The data are represented by solid points on which the horizontal bar indicates the width of the bin and the vertical one the associated statical uncertainty. In the lower plots the ratio between data and the total SM background is presented with the associated statistical uncertainty. The last bin of the distributions includes the overflow. Two simulated signal models based on the production process of Figure 5.1(a) are also included for comparison.

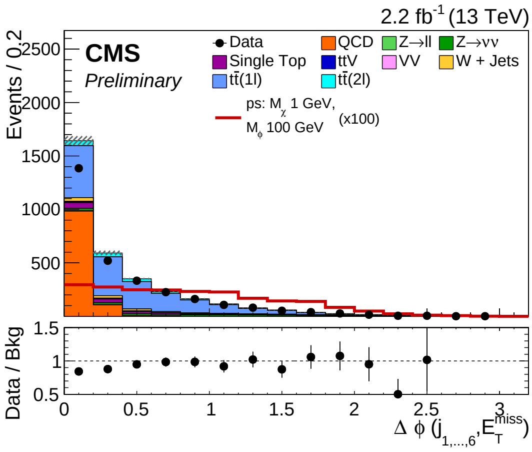

Figure 5.13: Distribution of $\Delta\phi(j_{1,2}, E_T^{miss})$ after applying the hadronic preselection for the 13 TeV analysis. The solid histograms for the simulated SM backgrounds are summed cumulatively and rescaled to luminosity and the grey hatched band represents the associated statistical uncertainty. The data are represented by solid points on which the horizontal bar indicates the width of the bin and the vertical one the associated statical uncertainty. In the lower plots the ratio between data and the total SM background is presented with the associated statistical uncertainty. One simulated signal model based on the production process of Figure 5.1(a) is also included for comparison.

The selection criteria for $\Delta\phi(j_{1,..,6}, E_T^{miss})$ is optimized, after preselection, to increase expected significance for various DM signals and it is presented in Table 5.5.

5.3.4 Background data-driven estimate

In the presented analysis, SM background predictions in SR are improved employing CRs enriched in specific SM contributions. As mentioned above, the subdominant SM backgrounds are estimated instead from the simulation.

In the 13 TeV analysis, the E_T^{miss} distributions in the CRs and SR are fitted simultaneously in the signal extraction procedure, Section 6.2. This technique improves the background estimation constraining the predicted SR normalization via the background enriched regions. It also accounts for possible signal contamination in the CRs.

For the 8 TeV analysis, data-to-simulation scaling factors (SFs) are extracted from the CRs. Two orthogonal CRs are defined, one enriched in the $t\bar{t}$ background and another dominated by W+jets events. In both regions, the remaining contributions from subdominant backgrounds are subtracted from data. The SFs are calculated by matching simultaneously to data the M_T distribution in the $t\bar{t}$ CR and the E_T^{miss} distribution in the W+jets CR. In this procedure, the shapes of the simulated distributions are maintained fixed constructing probability density functions (PDFs) and their normalizations are determined from data as parameters of the fit. The RooFit toolkit for data modeling [149] is used for the construction of the PDFs. The SFs obtained from the fit are then extrapolated into the SR, obtaining the expected number of background events $N(bkg\ pred,\ SR)$ as:

$$N(bkg\ pred,\ SR) = SF(CR) \cdot N(bkg\ (MC),\ SR)$$

where $N(bkg\ (MC),\ SR)$ are the number of simulated events in the SR, which are then multiplied by the scaling factors $SF(CR)$ determined in the CR. The contribution from DM events in the CRs is estimated to be negligible and therefore does not have an impact on the estimation of the SFs.

The selections used to define the CRs for the hadronic and single lepton channels are described in the following and summarized in Table 5.6.

Single lepton channel

In the single lepton channel, the dominant backgrounds consist of $t\bar{t}(2l)$ and W$(l\nu)$+jets events. In the 13 TeV analysis, another sizable contribution arise from single top quark processes, which are estimated from the $t\bar{t}(2l)$ enriched CR. For the 8 TeV analysis, a CR targeting the inclusive $t\bar{t}$ background is used in addition to a W+jets enriched region.

The details of the various regions used to improve the background description are listed in the following specifying for which analysis have been employed. A schematic view of the main requirements used to guarantee the orthogonality of each CR with respect to the associated SR is shown in Figure 5.14.

$t\bar{t}(2l)$: it is defined requiring an additional lepton with $p_T > 30$ GeV, $|\eta| < 2.1$ and satisfying tight identification criteria with respect to the associated SR. The requirements on the M_T, M_{T2}^W and $\Delta\phi(j_{1,2}, E_T^{miss})$ variables used for the SR are not applied to guarantee a higher statistics. The $t\bar{t}(2l)$ passes the single lepton SR selection when one lepton from the decay of the top quarks is not identified rather than being out of the detector acceptance. This motivates why the E_T^{miss} distribution is considered in this region instead of a distribution obtained by the sum of E_T^{miss} and the p_T of the non identified lepton.

$t\bar{t}$: the control region used in the 8 TeV analysis for the $t\bar{t}$ background is identified by the single lepton preselection with the additional requirement $M_T > 160$ GeV.

W($l\nu$)+jets: the same number of jets and leptons used to identify the single lepton SR is used, but zero b-tagged jets are required. In addition, events are required to satisfy $M_T > 160$ GeV and $E_T^{miss} > 160$ GeV.

Hadronic channel

The major backgrounds for the hadronic channel are $t\bar{t}(1l)$ and W($l\nu$)+jets, where one lepton is not identified, and Z($\nu\nu$)+jets events. The details of the various regions used to improve the background description are listed in the following.

$t\bar{t}(1l)$: the control region enriched in the $t\bar{t}(1l)$ background is defined requiring one lepton with $p_T > 30$ GeV, $|\eta| < 2.1$ and satisfying tight identification criteria. The other hadronic preselection requirements are applied with the addition of $M_T < 160$ GeV to avoid overlap with the single lepton SR. A requirement on the discriminating variable $\Delta\phi(j_{1,..,6}, E_T^{miss})$ is not applied to increase the statistics of the CR. Similarly to the case of $t\bar{t}(2l)$ CR, events which pass the SR selection are characterized by one lepton from the top quark decay that is not identified rather than being out of the detector acceptance. For this reason the E_T^{miss} distributions is considered in this CR for the simultaneous fit.

V+jets: an inclusive V+jets CR is obtained applying the hadronic SR selection but requiring 0 b-tagged jets. The background composition of this CR consists of both W+jets and Z+jets events, for which dedicated CRs are also defined as explained in the following.

W($l\nu$)+jets (no b jets): a CR enriched mainly in W($l\nu$)+jets events is defined as the V+jets CR, requiring in addition one lepton with $p_T > 30$ GeV, $|\eta| < 2.1$ and satisfying tight identification criteria, and $M_T < 160$ GeV.

Z($\nu\nu$)+jets: for the Z($\nu\nu$)+jets background a CR enriched in Z(ll)+jets events is identified. It is obtained with the same requirements used for the V+jets CR but demanding two leptons with $p_T > 30$ GeV, $|\eta| < 2.1$ and satisfying tight identification. In addition, the two leptons are required to have the same flavour, opposite charge and a total invariant mass m_{ll} between 60 and 120 GeV. For the Z($\nu\nu$)+jets background the E_T^{miss} in the SR is given, assuming perfect measurements, by the two neutrinos in the final state. In order to reproduce the predicted SR distribution, the E_T^{miss} subtracted of the lepton pair momentum is considered in this CR for the simultaneous fit.

	Single lepton control regions			*Hadronic control regions*			
Variables	$t\bar{t}(2l)$	$t\bar{t}$	W($l\nu$)+jets	$t\bar{t}(1l)$	V+jets	W($l\nu$)+jets	Z(ll)+jets
leptons	$= 2$	$= 1$	$= 1$	$= 1$	$= 0$	$= 1$	$= 2$
jets	≥ 3	≥ 3	≥ 3	≥ 4	≥ 4	≥ 4	≥ 4
b jets	≥ 1	≥ 1	$= 0$	≥ 2	$= 0$	$= 0$	$= 0$
E_T^{miss}	> 160 GeV	> 160 GeV	> 160 GeV	> 200 GeV	> 200 GeV	> 200 GeV	> 200 GeV
M_T	–	> 160 GeV	> 160 GeV	< 160 GeV	–	< 160 GeV	–
M_{T2}^{W}	–	–	–	–	–	–	–
$\Delta\phi(j_i, E_T^{miss})$	–	–	–	$i = 1, .., 6;$ > 1	$i = 1, .., 6;$ > 1	$i = 1, .., 6;$ > 1	$i = 1, .., 6;$ > 1
m_{ll}	–	–	–	–	–	–	$[60, 120]$ GeV
opposite charge leptons	–	–	–	–	–	–	yes

Table 5.6: Overview of the requirements used to define the controls regions for the single lepton (8 TeV and 13 TeV) and hadronic (13 TeV) channels.

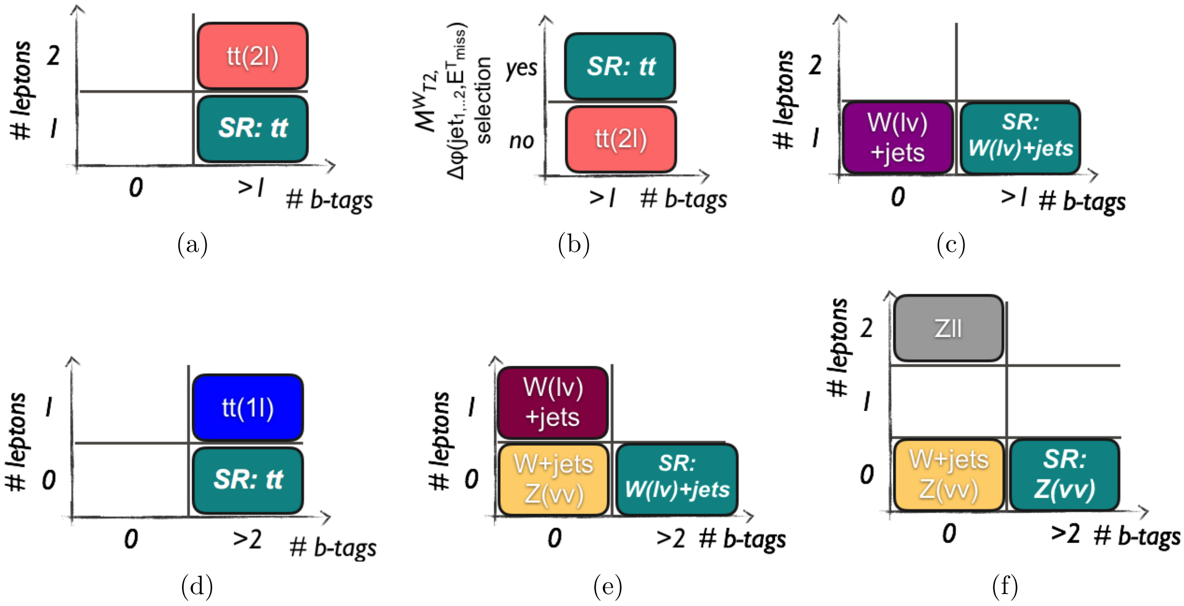

(a) (b) (c)

(d) (e) (f)

Figure 5.14: Schematic view of the main requirements used to guarantee the orthogonality of $t\bar{t}(2l)$ (a), $t\bar{t}$ (b) and W($l\nu$)+jets (c) CRs with respect to the associated single lepton SR and of $t\bar{t}(1l)$ (d), W($l\nu$)+jets (no b jets) (e) and Z($\nu\nu$)+jets (f) with respect to the hadronic SR.

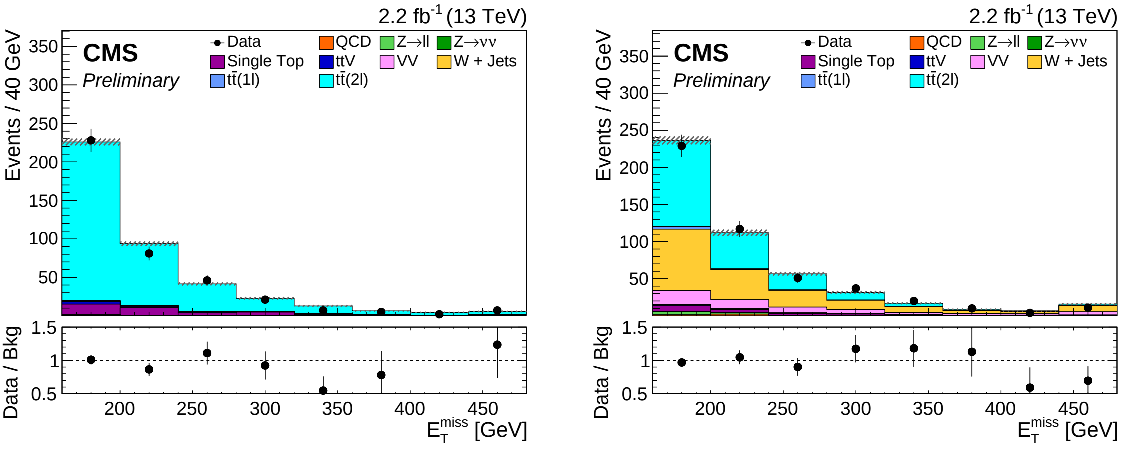

(a)

(b)

Figure 5.15: E_T^{miss} distributions in the 13 TeV analysis single lepton control regions enriched in $t\bar{t}(2l)$ (a) and W$(l\nu)$+jets (b) events. The solid histograms for the simulated SM backgrounds are summed cumulatively and rescaled to luminosity and the grey hatched band represents the associated statistical uncertainty. The data are represented by solid points on which the horizontal bar indicates the width of the bin and the vertical one the associated statical uncertainty. In the lower plots the ratio between data and the total SM background is presented with the associated statistical uncertainty. The last bin of the distributions includes the overflow.

Kinematic distributions in control regions and scale factor extraction

Figures 5.15 and 5.16 show the expected and observed E_T^{miss} distributions for the 13 TeV single lepton and hadronic CRs, respectively. In general, the E_T^{miss} spectrums in data and simulation are in good agreement. Differences are observed in the W$(l\nu)$+jets (no b jets) and Z$(\nu\nu)$+jets hadronic CRs. The discrepancies are mainly in the normalization, which are resolved by the simultaneous fit performed for the result extraction, Section 6.2.

The results of the 8 TeV simultaneous fit are presented in Figure 5.17. In particular, the M_T distribution is shown after the fit in the $t\bar{t}$ CR and the E_T^{miss} spectrum in the W$(l\nu)$+jets CR. The obtained SFs for $t\bar{t}$ and W+jets processes are 1.11 ± 0.02 (stat) and 1.26 ± 0.06 (stat), respectively.

Figure 5.18 and 5.19 present the E_T^{miss}, M_T, M_{T2}^W and $\Delta\phi(j_{1,2}, E_T^{miss})$ distributions in the $t\bar{t}$ and W$(l\nu)$+jets CRs after the SFs are applied to the simulation. Since part of these variables are used to assure the orthogonality of the CRs with respect to the SR, the good agreement observed between data and simulation validates the procedure used to evaluate the SFs and their propagation to the SR.

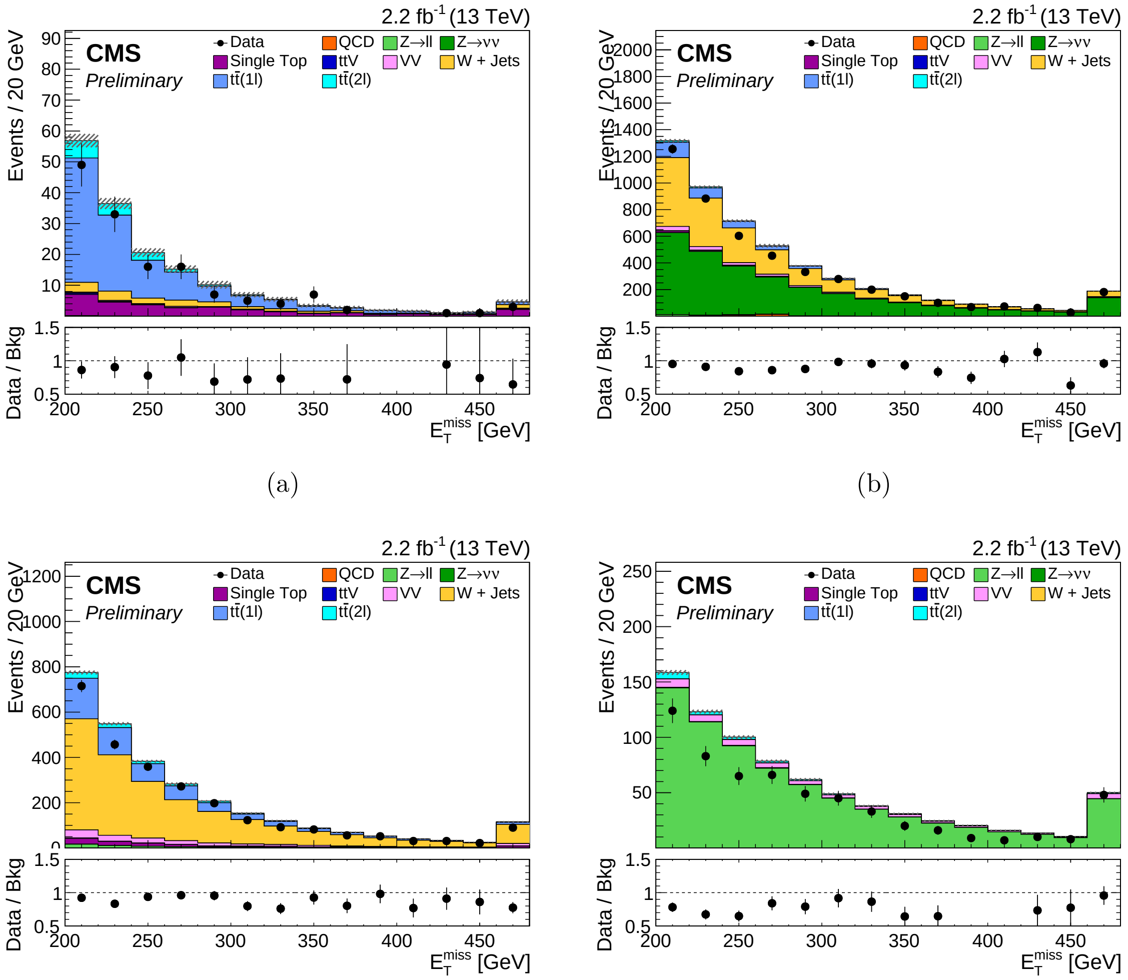

(a) (b) (c) (d)

Figure 5.16: E_T^{miss} distributions in the 13 TeV analysis single lepton control regions enriched in $t\bar{t}(1l)$ (a), V+jets (b), W($l\nu$)+jets (c) and Z($\nu\nu$)+jets (d) events. The solid histograms for the simulated SM backgrounds are summed cumulatively and rescaled to luminosity and the grey hatched band represents the associated statistical uncertainty. The data are represented by solid points on which the horizontal bar indicates the width of the bin and the vertical one the associated statical uncertainty. In the lower plots the ratio between data and the total SM background is presented with the associated statistical uncertainty. The last bin of the distributions includes the overflow.

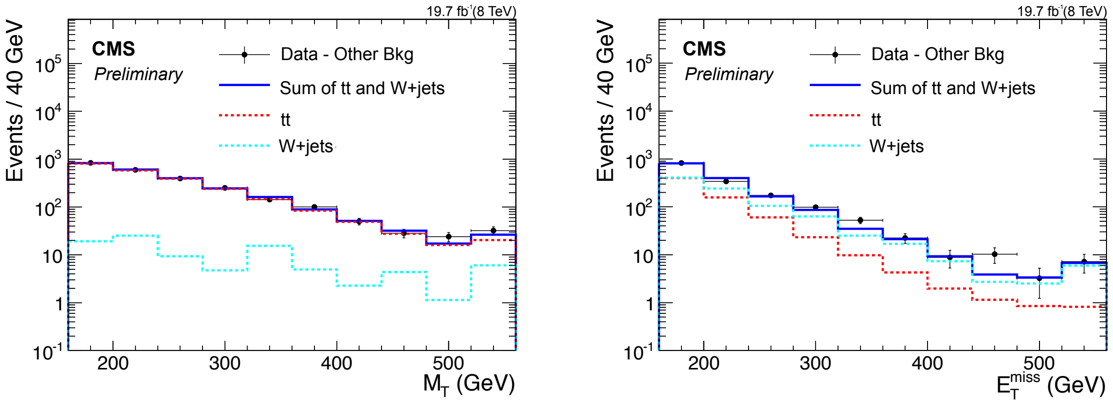

(a) (b)

Figure 5.17: Simultaneous matching of $t\bar{t}$ and W($l\nu$)+jets simulated samples to data considering the M_T distribution in the CR enriched in $t\bar{t}$ events (a) and the E_T^{miss} spectrum for the CR dominated by W($l\nu$)+jets processes. The red and cyan dashed histograms correspond to $t\bar{t}$ and W($l\nu$)+jets simulated distribution respectively after the fit procedure. The solid histograms corresponds to the sum of the two backgrounds. The data are represented by solid points on which the horizontal bar indicates the width of the bin and the vertical one the associated statical uncertainty. The last bin of the distributions includes the overflow.

5.3.5 Systematic uncertainties

The results of the analysis are sensitive to experimental and theoretical uncertainties affecting the distributions in the SR and CRs. Their effect is incorporated in systematic uncertainties (systematics).

A distinction is made between uncertainties affecting the normalization (normalization uncertainties) or the shape (shape uncertainties) of the distributions. In the latter category an overall normalization effect might be also present. In general, systematic uncertainties on observables are taken into account by introducing in the result extraction nuisance parameters θ that follow a specific probability density function (*pdf*), Section 6.1. In this work, the normalization and shape uncertainties categories are modeled with a log-normal distribution and a morphing techniques, respectively.

The uncertainties considered in this analysis are presented below.

Log-normal distribution

The log-normal *pdf* is defined as [150]:

$$\rho(\theta) = \frac{1}{\sqrt{2\pi}\ln(\kappa)} \exp\left(-\frac{(\ln(\theta/\tilde{\theta}))^2}{2(\ln\kappa)}\right)\frac{1}{\theta}$$

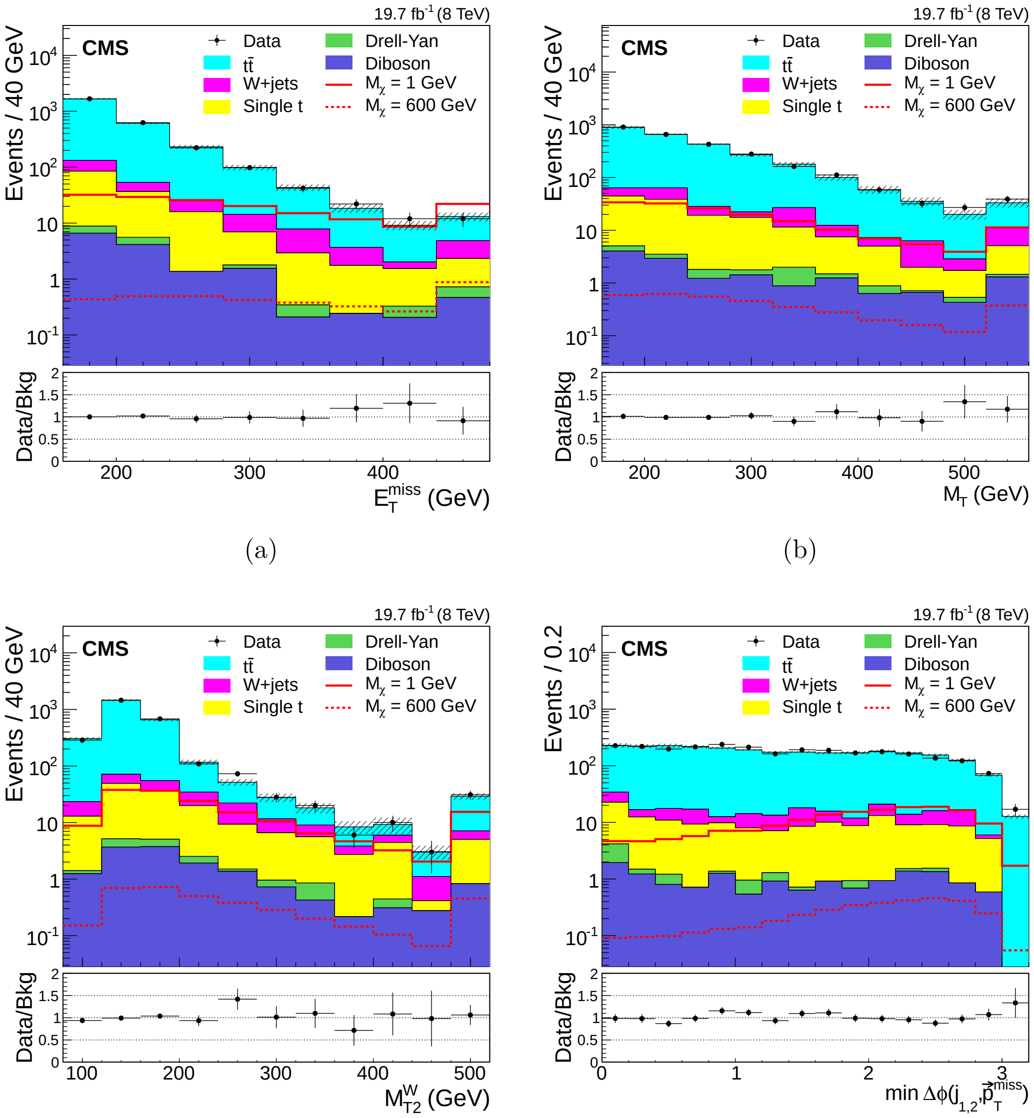

(a) (b)

(c) (d)

Figure 5.18: Distributions of E_T^{miss}, M_T, M_{T2}^W and $\Delta\phi(j_{1,2}, E_T^{miss})$ in the CRs enriched in $t\bar{t}$ events after the SFs for $t\bar{t}$ and W($l\nu$)+jets simulated samples. The solid histograms for the simulated SM backgrounds are summed cumulatively and rescaled to luminosity and the grey hatched band represents the total uncertainty in the background prediction. The data are represented by solid points on which the horizontal bar indicates the width of the bin and the vertical one the associated statical uncertainty. In the lower plots the ratio between data and the total SM background is presented with the associated statistical uncertainty. The last bin of the distributions includes the overflow. Two simulated signal models based on the production process of Figure 5.1(a) are also included for comparison.

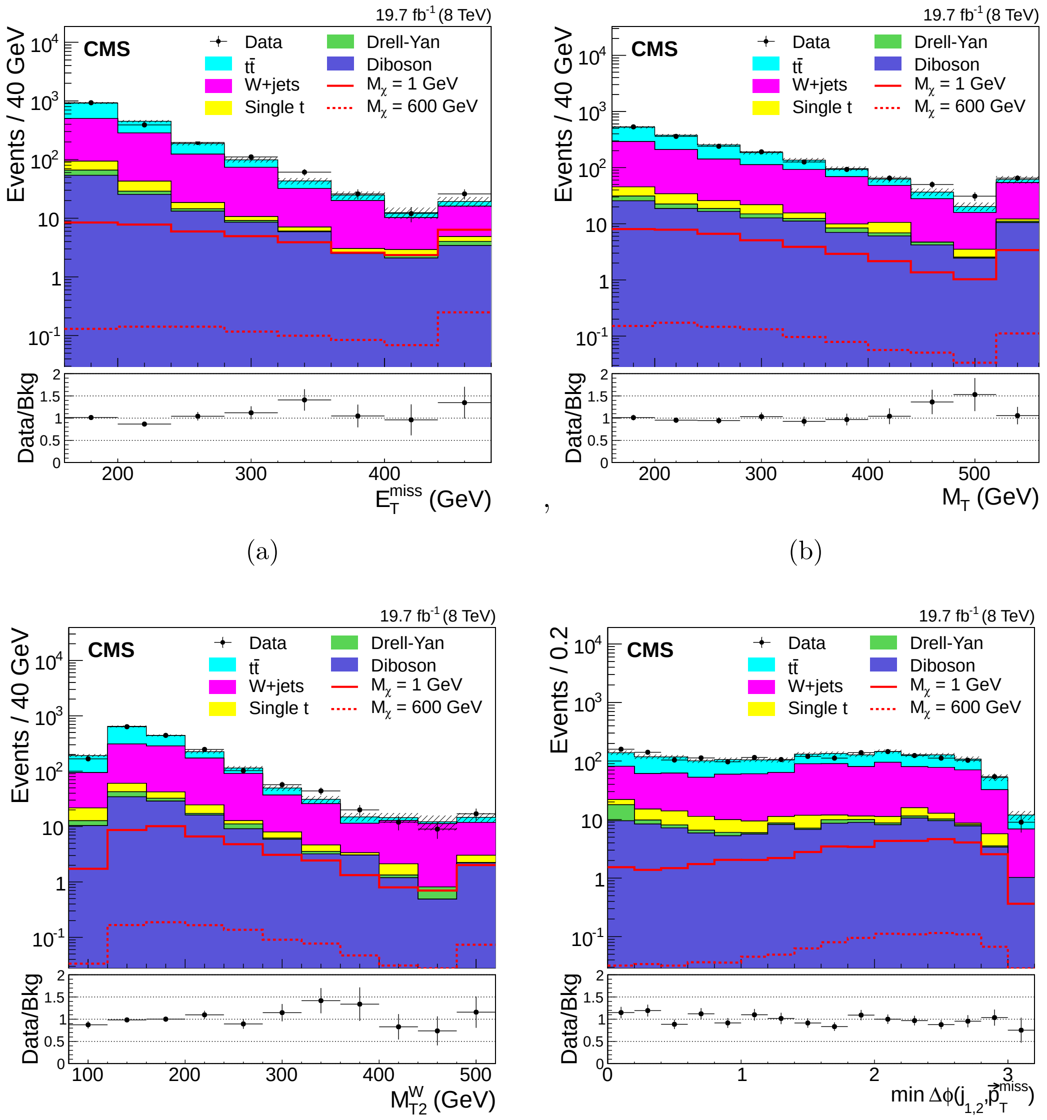

(a) (b)

(c) (d)

Figure 5.19: Distributions of E_T^{miss}, M_T, M_{T2}^W and $\Delta\phi(j_{1,2}, E_T^{miss})$ in the CRs enriched in W($l\nu$)+jets events after the SFs for $t\bar{t}$ and W($l\nu$)+jets simulated samples. The solid histograms for the simulated SM backgrounds are summed cumulatively and rescaled to luminosity and the grey hatched band represents the total uncertainty in the background prediction. The data are represented by solid points on which the horizontal bar indicates the width of the bin and the vertical one the associated statical uncertainty. In the lower plots the ratio between data and the total SM background is presented with the associated statistical uncertainty. The last bin of the distributions includes the overflow. Two simulated signal models based on the production process of Figure 5.1(a) are also included for comparison.

where $\tilde{\theta}$ represents the best estimate of the nuisance θ and the width of the distribution is characterized by κ. For small uncertainties, for which the Taylor expansion can be used, the relation of κ to the width σ of a Gaussian distribution is $1+\sigma = \kappa$. For larger uncertainties, a Gaussian *pdf* cannot be used for positive value observable, while the log-normal distribution is a better choice because it goes to zero at $\theta = 0$ guaranteeing the variable to remain positive [150].

Morphing technique

Shape uncertainties affects the spectrum shape but can also modify its overall normalization in the i bin. The total modification of the distribution can be modeled changing in the simulation the parameter j affected by the systematic to its most probable value plus (minus) its uncertainty. The obtained new spectrums referred to as ϵ_{ij}^{-} (ϵ_{ij}^{+}). The distribution obtained with the best estimate of the parameter j is indicated as ϵ_{ij}^{0}.

For different j values, a continuos estimate ϵ_{ji} of the distribution is obtained in each bin i from the ϵ_{ij}^{-}, ϵ_{ij}^{0} and ϵ_{ij}^{+} spectrums using a "morphing" technique [151]. A morphing parameter f nominally equal to zero and with an uncertainty of 1 is introduced. In each bin i a quadratic interpolation between the three distributions is performed and the value for the distribution in the bin i for $|f| < 1$ will be given by [151]:

$$\epsilon_{ji} = \frac{f(f-1)}{2}\epsilon_{ji}^{-} - (f-1)(f+1)\epsilon_{ji}^{0} + \frac{f(f+1)}{2}\epsilon_{ji}^{+}$$

Source of uncertainty in the analysis

The systematic uncertainties considered in the 13 TeV analysis are described in the following and summarized in Table 5.7. The names of the nuisances as used in the simultaneous fit procedure (Section 6.2) are specified in brackets.

The sources of uncertainties affecting the **normalization** are:

- *lepton identification and trigger* (lep); it includes uncertainties on the lepton reconstruction, identification and triggering efficiency. This uncertainty is evaluated from $Z(ll)$ samples, using a tag-and-probe technique, to range from 2% to 4% depending of the η and p_T of the lepton.

- *b-tagging and mistagging efficiencies* (btag and mistag); the uncertainties on the efficiency to tag or mistag a jet as coming from a b quark are measured in independent control samples [131] to range from 1% to 11% depending on the tagging flavour.

- *pileup modeling* (pu); it refers to uncertainties in the modeling of PU in simulation. They are estimated by varying the minimal bias cross section in the estimation of the number of PU interactions in data by ±5%, Section 5.2.5. The uncertainty on the background yields due to PU is estimated to be 2.0%.
- E_T^{miss} *trigger* (metTrigger); an uncertainty of 2% is associated to the correction factors for the trigger E_T^{miss} efficiency.
- *Luminosity* (lumi)*;* the integrated luminosity of the data sample has an associated uncertainty of 2.7% [152].
- *QCD normalization* (QCD_xsec); QCD processes, while negligible in the presented analysis, are characterized by tail effects in the E_T^{miss} distribution. An uncertainty of 100% is considered for the QCD backgrounds to cover these effects.

As **shape** uncertainties the following sources are considered:

- *jet energy scale* (symjes); the average jet response, JES, after the factorized approach presented in Section 4.2.5 is at 1 within 2% to 8% uncertainties depending on the jet η and p_T. This uncertainty is propagated to the four-momenta of all jets and to all observables, for example the E_T^{miss}. Normalization uncertainties due to JES are in the range $1-2\%$.
- *PDF uncertainties* (pdf_total); uncertainties associated with the PDF used to simulate the hard scattering process are assessed by reweighting the samples with the NNPDF3.0 [138] replicas [153]. A normalization uncertainties of $1-5\%$ is estimated depending on the sample considered.
- *V+jets heavy-flavour fraction* (WHF, ZHF); the uncertainty on the fraction of heavy flavour jet in V+jets processes is considered allowing the relative contribution of heavy and light flavour quarks to vary within 20% [154–157]. The associated normalization uncertainty varies from few % up to 10% depending on the SR or CR considered.
- *EWK and QCD k-factors* (ZEWK, WEWK; ZQCDFac, ZQCDRen, QCDFac and WQCDRen); the uncertainties on the EWK and QCD NLO/LO k-factors applied

to the V+jets samples are considered independently. In addition, the effect of factorization and renormalization scales on the QCD k-factor are considered separately. The uncertainty on the normalization is in the range $1 - 5\%$.

- *Top p_T reweighting* (topPtWeight); the uncertainty associated with the top p_T reweighting procedure presented in Section 5.2.1 is considered in the analysis. It is evaluated by either not applying the reweighting or applying it twice.
- *Factorization and renormalization scales μ_F and μ_R* (q_2); the theoretical uncertainties on the choice of the QCD factorization and renormalization scale parameters [158] are taken into account considering $t\bar{t}$ simulated samples in which the scales are halved or doubled. The associated normalization uncertainties are $3-4\%$ and $5-12\%$ for the factorization and renormalization scales, respectively.
- *Simulation statistics*; this source of uncertainty is related to the limited number of events simulated for each process. It is included in the analysis by allowing each bin of the E_T^{miss} distribution in SR and CRs to variate independently according to the statistical uncertainty of the simulation.

In the 8 TeV analysis, the SFs for $t\bar{t}$ and W+jets events are extracted from CRs. Using this procedure, part of the systematic uncertainties are covered by the calculated SFs, namely the integrated luminosity, lepton identification and trigger efficiencies.

The uncertainties associated with the SFs estimation are considered in the analysis. For the minor backgrounds subtracted from data, Section 5.3.4, a conservative uncertainty on their normalization of 50% is assigned. This systematic covers missing higher order corrections or mismodeling in the simulation of their kinematic properties. The change in the measured SFs is of 5% and 9% for the $t\bar{t}$ and W+jets backgrounds respectively. The stability of the data-driven background estimation is checked modifying the definitions of the CRs. For example new CRs are defined tightening the E_T^{miss} selection or adding requirements on the M_{T2}^W, and $\Delta\phi(j_{1,2}, E_T^{miss})$ variables with respect to the definitions of Section 5.3.4. These studies translates in an uncertainty of 40% on the W+jets SFs, while for the $t\bar{t}$ background negligible changes are observed.

Similar to the 13 TeV analysis, uncertainties on jet energy scale, b-tagging and mistagging efficiencies, pileup modeling, and on top p_T reweighting are considered. For the uncertainty associated with the PDF choice, the simulated samples are reweighted with CT10 [159], MWST2008 [160] and NNPDF2.3 [161] following the PDF4LHC recommendation [162, 163]. Jet energy resolution uncertainties are also included, while the

	13 TeV analysis uncertainties		
Source	Category	on background (%)	on signal (%)
lepton ID and trigger	normalization	$2-4\%$	2%
b-tagging, mistagging	normalization	$1-11\%$	$0.5-7\%$
pileup	normalization	2%	$0.5-7\%$
E_T^{miss} trigger	normalization	2%	2%
luminosity	normalization	2.7%	2.7%
QCD normalization	normalization	100%	-
jet energy scale	shape	$1-2\%$	$1-7\%$
PDF	shape	$1-5\%$	$8-15\%$
V+jets heavy flavour fraction	shape	$1-10\%$	-
top p_T reweighting	shape	-	-
μ_F *and* μ_R	shape	$3-12\%$	-
simulation statistics	shape	-	-

Table 5.7: List of systematic uncertainty sources for the 13 TeV analysis. The distribution used to model the uncertainty in the result extraction is specified. The associated contribution in % to the final background and signal estimation is included.

impact of μ_F *and* μ_R uncertainties is found to be negligible. The uncertainties considered for the 8 TeV analysis on the background prediction are summarized in Table 5.8.

For the DM signal the uncertainty on the luminosity, lepton identification and trigger, jet energy scale, b-tagging and mistagging efficiencies are considered.

The uncertainties on the modeling of the DM signal considered are: luminosity, lepton identification and trigger, jet energy scale, b-tagging and mistagging efficiencies. In the 8 TeV analysis, the jet energy resolution source is also taken into account, while in the 13 TeV search E_T^{miss} trigger, pileup, PDF and simulation statistics uncertainties are included. The uncertainties associated with the DM signal is presented in Table 5.7 and 5.8 for the 13 TeV and 8 TeV analyses, respectively. Their exact value depends on the production process and on the DM mass hypothesis.

	8 TeV analysis uncertainties	
Source	on background (%)	on signal (%)
lepton ID and trigger	-	$1-2\%$
b-tagging, mistagging	$1.0-1.8\%$	$1-4\%$
pileup	2.0%	-
luminosity	-	2.6%
jet energy scale	4.0%	$2-3\%$
PDF	2.6%	-
top p_T reweighting	3.9%	-
μ_F *and* μ_R	negligible	negligible
jet energy resolution	3.0%	$< 1\%$
50% normalization uncert. on other bkg in deriving SFs	10%	-
SF for W+jets (CR tests)	13%	-

Table 5.8: List of systematic uncertainty sources for the 8 TeV analysis. The associated contribution in % to the final background and signal estimation is included.

Chapter 6

Results and interpretation

The results of the analysis and their interpretation are presented in this chapter. First, the statistical methods used to extract the results are presented in Section 6.1. The data collected by CMS and observed in the SR are discussed in Section 6.2, together with the expected SM backgrounds.

The theoretical models used to describe the tt+DM processes are introduced in Section 6.3. These models are used to interpret the observed data and, if no excess is found above SM expectations, to constrain the parameters of the model as explained in Section 6.4.

6.1 Statistical methods

The statistical methods used to verify the validity of the model employed to describe signal processes and to constrain its parameters are outlined in this section. A more comprehensive overview on statistical methods can be found in [24, 150, 164].

6.1.1 Maximum Likelihood

The maximum likelihood is used as parameter estimation for the signal strength and the background normalization. A short overview will be presented following [24].

Let us assume to have a set $\boldsymbol{x}$ of measured quantities depending on a collection of parameters $\boldsymbol{\theta} = (\theta_1, .., \theta_N)$. The maximum likelihood estimator for $\boldsymbol{\theta}$ is defined as the value that maximize the likelihood function $L(\boldsymbol{\theta})$. It is generally common to maximize $ln\, L(N|q)$, which has a maximum for the same value of $\boldsymbol{\theta}$ that maximizes $L(\boldsymbol{\theta})$.

If a set of m statistically independent measurements $\boldsymbol{x} = (x_1, ..., x_m)$ is considered and each follows the same probability density function $f(x; \boldsymbol{\theta})$, then the likelihood can be expressed as:

$$L(\boldsymbol{\theta}) = \prod_i f(x_i; \boldsymbol{\theta}).$$

Assuming that the number of data n_i in the i^{th} measurement follows a Poisson distribution with mean λ_i, the likelihood takes the form:

$$L(\boldsymbol{\theta}) = \prod_i Poisson(n_i|\lambda) = \prod_i \frac{\lambda^{n_i}}{n_i!} e^{-\lambda_i}$$

The number of observed data will have potentially contributions from both background and signal events, i.e. $\lambda = \mu_s s + \mu_b b$ where s (b) is the expected signal (background) yield multiplied by a strength modifier μ_s (μ_b). The strength modifier μ can be considered as an extra parameter to be determined in the maximization of $L(\boldsymbol{\theta})$.

The likelihood used in the analysis can be expressed as:

$$L(\mu_s, \mu_b, \theta) = \underbrace{Poisson(n_{SR}|\mu_S s + \mu_b b, \theta)}_{\text{Signal region}} \cdot \underbrace{\prod_{j=1}^{\#CR} Poisson(n_{CR_j}|\mu_S s_j + \mu_b b_j, \theta) \cdot}_{\text{Control region}} \underbrace{G(\tilde{\theta}, \theta)}_{\text{Constraints on nuisances}} \quad (6.1)$$

where here θ represents the systematic uncertainties, which are treated as nuisance parameters in the maximization of the likelihood. In the same equation, n_{SR} and n_{CRj} are the number of observed data in the SR and in the CR j, respectively.

The first term of Equation 6.1 refers to the observed and expected number of events in the SR. The second term is related to the CR j, while the last term represents the constraints on the uncertainties θ. The strength modifiers μ_s and μ_b are considered both in SR and CRs. This allow to constrain the major backgrounds from the data observed in the CRs and to take into account potential contaminations from signal events in these regions.

The shape of the E_T^{miss} distribution is taken into account as additional information for the parameter estimation, which translate in an additional product in Equation 6.1 extended to all bins of the E_T^{miss} spectrum.

The maximum likelihood method is employed in the 8 TeV analysis to extract the data-to-simulation SFs from the CRs, Section 5.3.4. The likelihood employed for this estimation is similar to the one presented in Equation 6.1, except that the background normalizations are determined only from the CRs. Here, the signal contributions are found to be negligible and therefore are not considered in the likelihood.

Pulls: post-fit uncertainties

The results of the maximum likelihood fit for the nuisance θ^{fit} and its variance $\sigma(\theta^{fit})$ can be compared with our assumptions on these parameters. For this purpose the pull statistic is used, which is defined as [165]:

$$pull = \frac{\theta^{fit} - \theta}{\sigma(\theta^{fit})}$$

The pull is expected to behave as a Gaussian distribution with mean value zero and width one. If the calculated pull value is largely different from zero then a wrong assumption has been made on that specific systematic uncertainty. If the width is smaller (higher) than one, a under(over)-constraining from the fit is present for the nuisance variance.

6.1.2 Hypothesis test: profile likelihood

To extract information about the presence of signal processes in data, the parameter of interest is the signal strength μ_s. This factor is often written as the ratio of the measured cross section σ and the value predicted by the theory model σ_{th}, i.e. $\mu_s = \sigma/\sigma_{th}$. If the observed data are compatible with the only SM backgrounds hypothesis then $\mu_s = 0$. If instead the data accommodate the presence of signal events with their predicted cross section $\mu_s = 1$.

The agreement between observation and a tested hypothesis is quantified by a test statistic q_μ. A short overview on this topic will be presented following [166].

In this work, the Profile likelihood is used as a test statistic and is defined as:

$$q_\mu = -2ln\frac{L(data|\mu, \hat{\theta}_\mu)}{L(data|\hat{\mu}, \hat{\theta})}, \quad \hat{\mu} \leq \mu \tag{6.2}$$

where L is the likelihood function, the parameters $\hat{\mu}$ and $\hat{\theta}$ are the one which maximize L, and $\hat{\theta}_\mu$ is the nuisance parameter which maximizes L for a fixed signal strength μ.

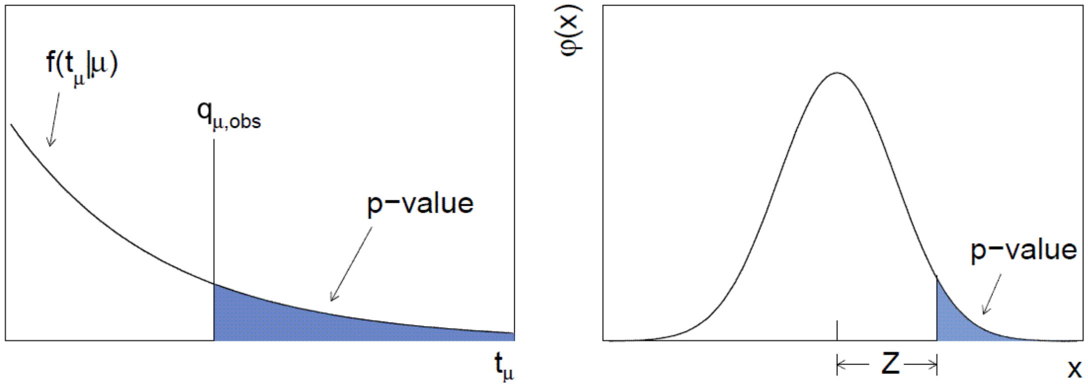

(a) (b)

Figure 6.1: Relation between the p-value and the observed value $q_{\mu,obs}$ of the probability density function $f(q_\mu \,|\, \mu)$ (a), and between p-value and the significance Z (b) [167].

The procedure of choosing a specific values of $\hat{\theta}$ for a given signal strength μ is often referred to as *profiling,* and $\hat{\theta}_\mu$ as the profiled value of θ [166].

A test statistic q_μ will present a particular probability density function $g(q_\mu \,|\, H)$ based on the hypothesis H under test. This distribution can be used to quantify the agreement between data and the only background hypothesis H_0 as:

$$p = \int_{t_{\mu,\,obs}}^{\infty} g(q_\mu \,|\, H_0), \tag{6.3}$$

where p is the so-called p-value and $q_{\mu,\,obs}$ is the test statistic observed in the experiment. Usually, the test statistic is defined in a way that lower values of p correspond to a worse agreement with H_0.

The p-value can also be expressed in terms of the significance Z. The latter is defined such that Z standard deviations upward fluctuation of a Gaussian random variable have an upper tail area equal to p [24], i.e.

$$Z = \Phi^{-1}(1 - p), \tag{6.4}$$

where Φ^{-1} is the inverse of the cumulative distribution of the single sided standard Gaussian. The relations of the p-value with $q_{\mu,\,obs}$ and with the significance Z are shown in Fig. 6.1. In high energy physics, a common choice is to set a significance of 5σ as requirement to claim a discovery, which corresponds to a p-value of 2.87×10^{-7}.

If the p-value calculated from the observed data cannot exclude the background only hypothesis, an upper limit on μ_s can be set. To calculate these limit we define the

CLs [168] ratio:

$$CL_s = \frac{p_\mu}{1 - p_0}$$

The 95 (90)% CL upper limit on μ_s is defined as the signal strength value μ_{up} that gives $CL_s(\mu_{up}) = 0.05(0.10)$.

6.2 Signal extraction

Events from tt+DM processes can be inferred as an excess of events in data with respect to SM expectations. Different approaches are used in the 13 TeV and 8 TeV analyses to search for possible excesses.

The results of the 13 TeV analysis are extracted using a binned maximum likelihood fit performed simultaneously to the E_T^{miss} distributions in the SRs and CRs (Section 5.3.3 and 5.3.4). The fit is performed for the single lepton and hadronic channels independently as well as for their combination.

An unconstrained nuisance μ_B is introduced in the fit for the dominant backgrounds ($t\bar{t}$, V+jets) to constrain their rates in the SR from the data observed in the CRs. These rate parameters are define separately for the single lepton and the hadronic channels. Potential signal contaminations are taken into account allowing the signal expectations to scale simultaneously in the SRs and CRs through a signal strength parameter.

The sources of systematic uncertainties are treated as nuisance parameters in the fit. Systematics affecting the normalization are modeled with a log-normal distribution. If they affect the shape of the E_T^{miss} distributions, and potentially also their overall normalization, a morphing technique is used instead, as discussed in more detail in Section 5.3.5.

The observed data yield and the post-fit expected background events are presented for the single lepton and hadronic channels in Table 6.1 and 6.3 respectively. The corresponding E_T^{miss} distributions are shown in Figure 6.2 for the single lepton and hadronic SRs and in Figure 6.3 and 6.4 for the associated CRs.

The pulls calculated for the nuisance parameters, except for the simulation statistics source, are shown in Figure 6.5. The relative pulls are close to zero, but few nuisances are corrected by negative or positive factors close to one. The variances are close to one for most of the nuisances, except for the uncertainty on the jet energy scale and

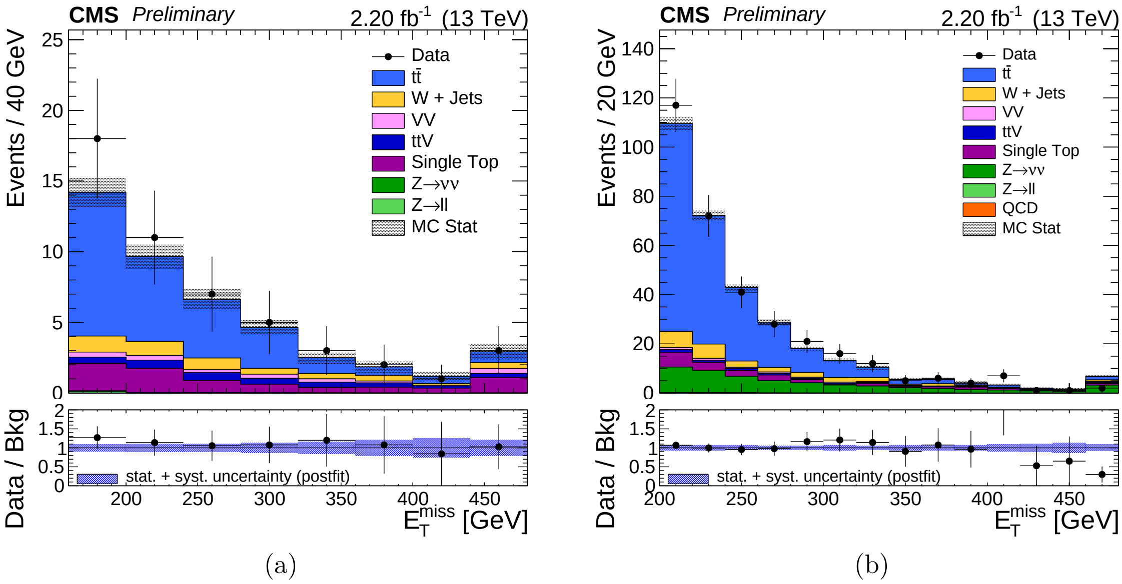

Figure 6.2: Post-fit E_T^{miss} distributions for the 13 TeV analysis in the single lepton (a) and hadronic (b) signal regions. The solid histograms for the simulated SM backgrounds are summed cumulatively and are shown after the simultaneous binned maximum likelihood across signal and control regions assuming zero signal contribution. The data are represented by solid points on which the horizontal bar indicates the width of the bin. In the lower plots the ratio between data and the total SM background is presented with the associated overall post-fit uncertainties statistical uncertainty shown by the blue band.

on the W+jets EWK k-factor. These uncertainties are over-constrained in the fit for the hadronic and the combined channels. Overall the nuisances perform as expected.

The results of the 8 TeV analysis are extracted from the comparison of the observed and expected number of events after the SR selection is applied. The major backgrounds ($t\bar{t}$, W+jets) normalization is obtained scaling the simulation by the SFs estimated in dedicated CRs, as explained in Section 5.3.4. Figure 6.6 shows the E_T^{miss} distribution obtained applying the SR selection except the requirement on the plotted variable and multiplying the $t\bar{t}$ and W+jets samples by the SFs. The number of observed events in the SR together with the background predictions are listed in Table 6.3.

As seen in Tables 6.1 to 6.3 and from the E_T^{miss} distribution in SR, no excess of events over the expected SM background is found. This result is independent of the particular model considered to describe the tt+DM processes. In the definition of the SRs as well, a generality is kept using only the main characteristic of the expected signal: higher E_T^{miss} and different topology with respect to the SM backgrounds.

The observed results, can now be used to constrain parameters of models describing the different tt+DM processes. The models used in this analysis are explained in the

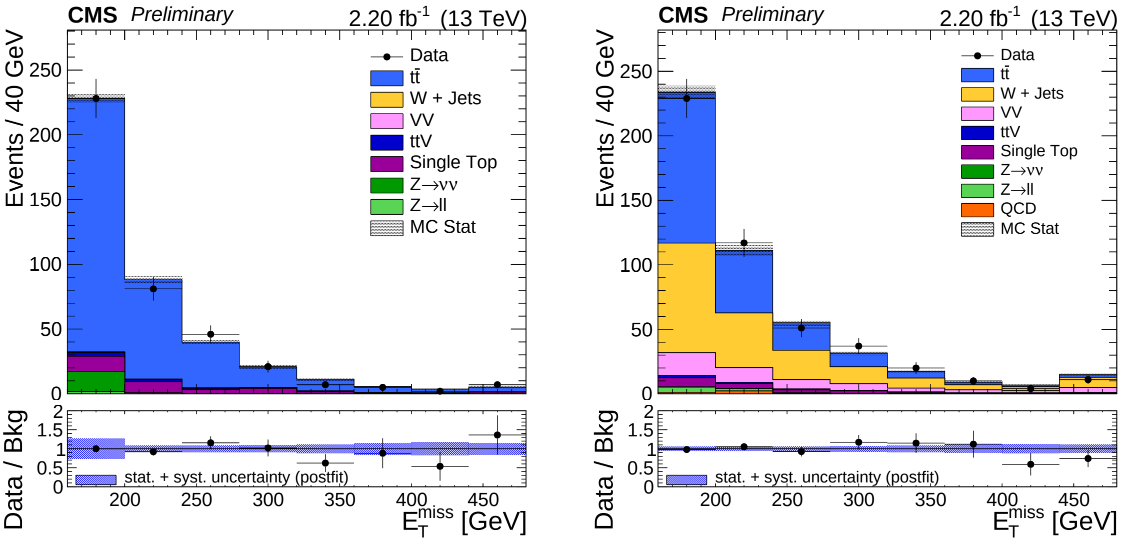

(a) (b)

Figure 6.3: Post-fit E_T^{miss} distributions for the 13 TeV analysis in the single lepton control regions enriched in $t\bar{t}(2l)$ (a) and W$(l\nu)$+jets (b) events. The solid histograms for the simulated SM backgrounds are summed cumulatively and are shown after the simultaneous binned maximum likelihood across signal and control regions assuming zero signal contribution. The data are represented by solid points on which the horizontal bar indicates the width of the bin. In the lower plots the ratio between data and the total SM background is presented with the associated overall post-fit uncertainties statistical uncertainty shown by the blue band.

	single lepton SR	$t\bar{t}(2l)$ *CR*	W$(l\nu)$+jets *CR*
$t\bar{t}$	26.25 ± 1.65	344.05 ± 20.51	207.98 ± 14.24
W+jets	4.68 ± 0.64	0.05 ± 0.01	185.65 ± 17.73
Z→ ll	0.12 ± 0.04	3.34 ± 0.44	7.46 ± 0.75
single top	7.38 ± 1.60	30.96 ± 4.50	17.66 ± 2.02
QCD	0.0 ± 0.0	0.0 ± 0.0	0.0 ± 0.0
Z→ $\nu\nu$	0.10 ± 0.09	0.0 ± 0.0	0.62 ± 0.13
ttV	3.10 ± 0.32	6.32 ± 0.94	4.49 ± 0.59
VV	1.96 ± 0.22	1.84 ± 0.24	52.43 ± 3.51
Backgrounds	43.59 ± 2.06	402.21 ± 60.89	479.65 ± 15.02
Data	50.00 ± 7.07	397.00 ± 19.92	479.00 ± 21.89

Table 6.1: Observed data yield and number of expected SM events after the fit procedure in the single lepton SR and CRs. The data presented were recorded at $\sqrt{s} = 13$ TeV and corresponds to an integrated luminosity of 2.2 fb^{-1}. The uncertainties associated with the expected SM yields are post-fit.

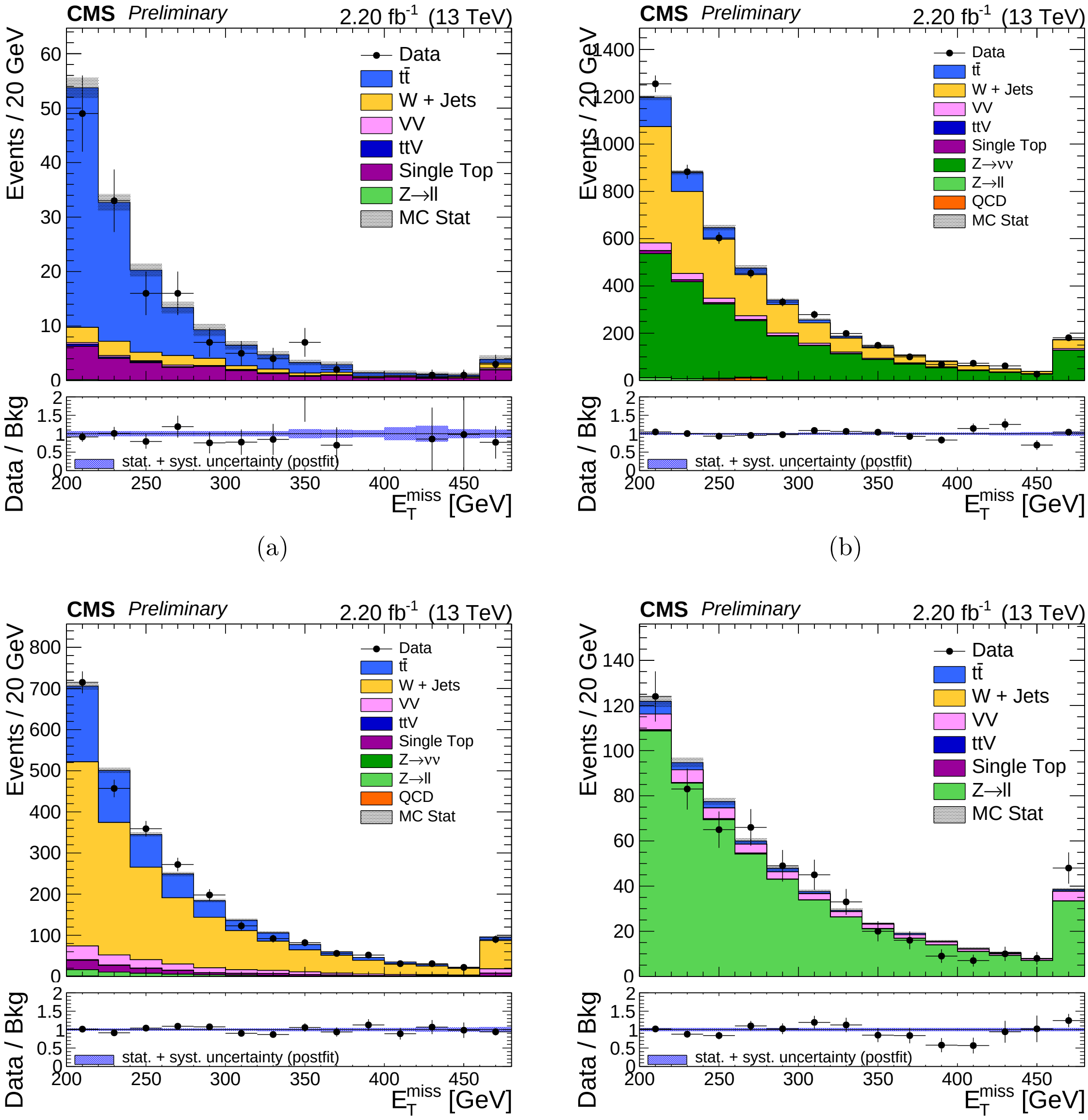

(a)

(b)

(c)

(d)

Figure 6.4: Post-fit E_T^{miss} distributions for the 13 TeV analysis in the hadronic lepton control regions enriched in $t\bar{t}(1l)$ (a), V+jets (b), W($l\nu$)+jets (c) and Z($\nu\nu$)+jets (d) events. The solid histograms for the simulated SM backgrounds are summed cumulatively and are shown after the simultaneous binned maximum likelihood across signal and control regions assuming zero signal contribution. The data are represented by solid points on which the horizontal bar indicates the width of the bin. In the lower plots the ratio between data and the total SM background is presented with the associated overall post-fit uncertainties statistical uncertainty shown by the blue band.

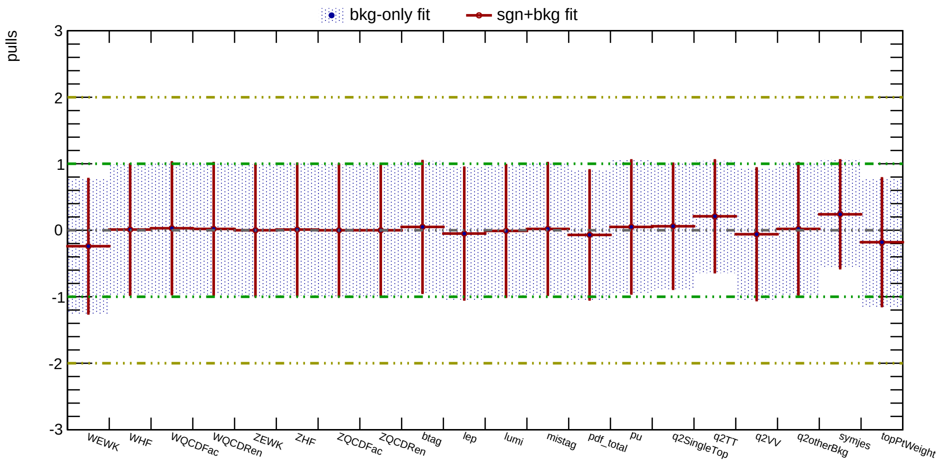

(a)

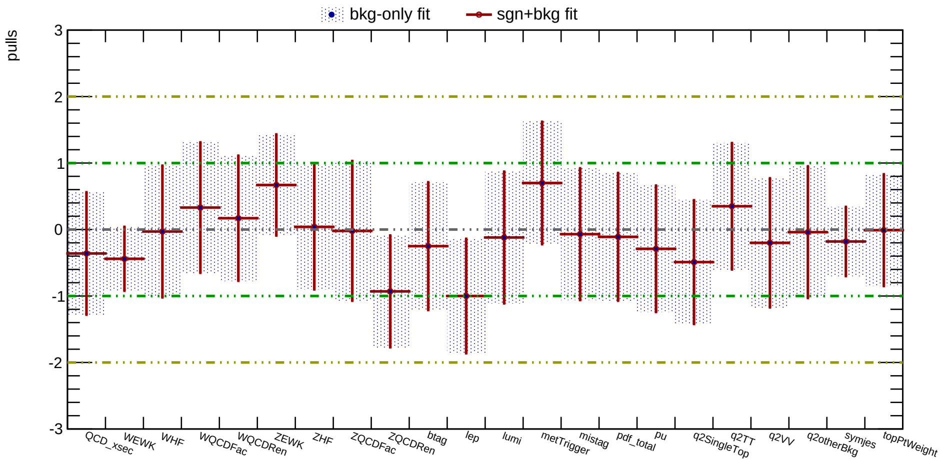

(b)

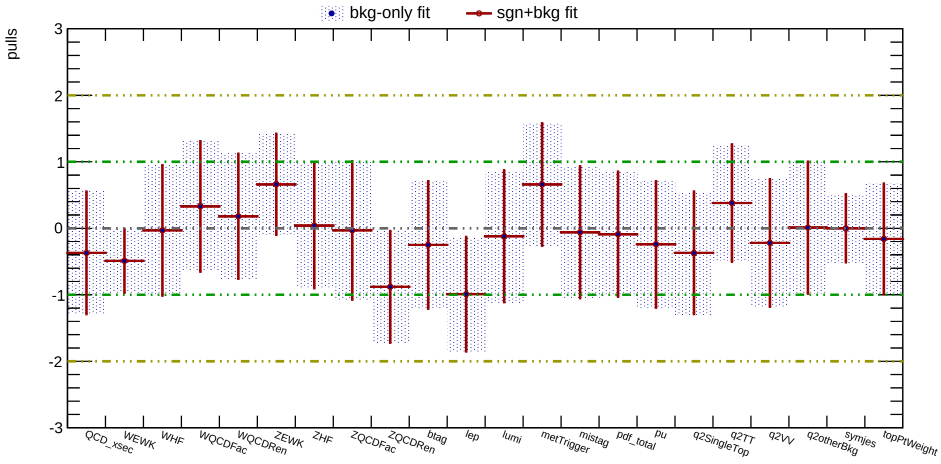

(c)

Figure 6.5: Pulls distributions for normalization and shape uncertainties as defined in Section 5.3.5 and included in the fit as nuisance parameters for the single lepton, hadronic channels and their combination. The *simulation statistics* source of uncertainty is not included in the distribution for simplicity.

	hadronic SR	$t\bar{t}(1l)$ *CR*	V+jets *CR*	W($l\nu$)+jets *(*no b jets) CR	Z($\nu\nu$)+jets *CR*
$t\bar{t}$	213.98 ± 10.57	111.09 ± 5.25	334.20 ± 17.65	584.14 ± 26.42	19.21 ± 1.13
W+jets	24.92 ± 1.63	14.06 ± 0.81	1700.24 ± 38.69	1705.75 ± 34.03	0.02 ± 0.00
Z→ ll	0.44 ± 0.06	0.37 ± 0.05	31.36 ± 1.95	52.04 ± 2.29	533.51 ± 7.90
single top	20.36 ± 1.12	26.77 ± 1.81	37.98 ± 1.93	91.11 ± 6.67	0.87 ± 0.12
QCD	0.10 ± 0.04	0.0 ± 0.0	16.42 ± 6.59	2.13 ± 0.80	0.0 ± 0.0
Z→ $\nu\nu$	52.61 ± 2.37	0.0 ± 0.0	2371.30 ± 32.72	0.09 ± 0.01	0.0 ± 0.0
ttV	6.26 ± 0.52	1.53 ± 0.16	6.27 ± 0.57	6.10 ± 0.68	1.83 ± 0.16
VV	5.17 ± 0.32	1.95 ± 0.13	143.31 ± 9.35	152.04 ± 9.39	40.96 ± 2.20
Backgrounds	323.85 ± 9.61	155.77 ± 4.87	4641.08 ± 37.11	2593.40 ± 30.10	596.40 ± 7.52
Data	333.00 ± 18.25	144.00 ± 12.00	4665.00 ± 68.30	2580.00 ± 50.79	583.00 ± 24.15

Table 6.2: Observed data yield and number of expected SM events after the fit procedure in the hadronic SR and CRs. The data presented were recorded at $\sqrt{s} = 13$ TeV and corresponds to an integrated luminosity of 2.2 fb^{-1}. The uncertainties associated with the expected SM yields are post-fit.

	SR (±stat ±syst)
$t\bar{t}$	$8.2 \pm 0.6 \pm 1.9$
W+jets	$5.2 \pm 1.8 \pm 2.1$
Drell–Yan	$0.3 \pm 0.3 \pm 0.1$
single top	$2.3 \pm 1.1 \pm 1.1$
Diboson	$0.5 \pm 0.2 \pm 0.2$
Backgrounds	$16.4 \pm 2.2 \pm 2.9$
Data	18

Table 6.3: Observed data yield and number of expected SM events in SR after the $t\bar{t}$ and W+jets SFs are applied. The data presented were recorded at $\sqrt{s} = 8$ TeV and corresponds to an integrated luminosity of 2.2 fb^{-1}. The uncertainties associated with the expected SM yields are also presented.

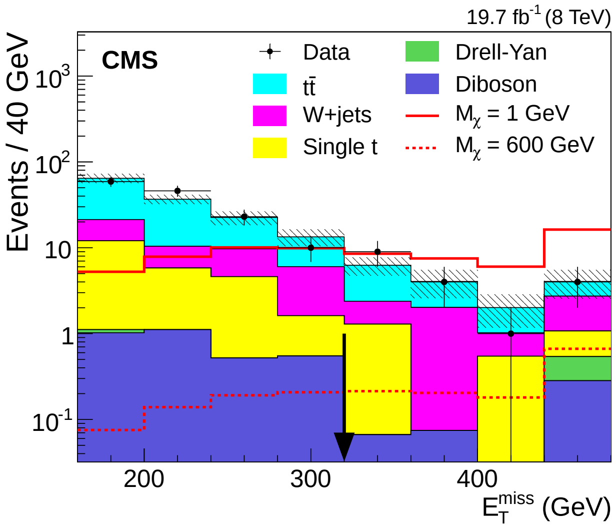

Figure 6.6: E_T^{miss} distributions for the 8 TeV analysis applying the SR selection except the requirement on the plotted variable, which is indicated by the black arrow. The solid histograms for the simulated SM backgrounds are summed cumulatively and are shown after the $t\bar{t}$ and W+jets SFs are applied. The data are represented by solid points on which the horizontal bar indicates the width of the bin. The grey hatched band represents the associated total uncertainty.

following section.

6.3 Dark matter phenomenology

The details of the interactions between the SM and the DM particles depend on the model assumed to describe these processes: contact interactions or more complete theories can be considered.

In this analysis, models assuming minimal flavor violation [169–172] are considered. Under this assumption, the couplings between Dirac fermionic DM and ordinary matter have the same structure as in the SM. As a consequence, when the mediator of the interaction is a spin-0 particle it has a Yukawa type coupling to fermions. The discovery potential for scalar interactions is therefore highly improved when investigating processes where the DM couples to more massive third generation quarks [173], in particular top quarks.

6.3.1 Effective field theories

In the maverick scenario [174], DM is the only new particles produced at the energy reached in *pp* collisions at the LHC. The mediator is not directly produced and the

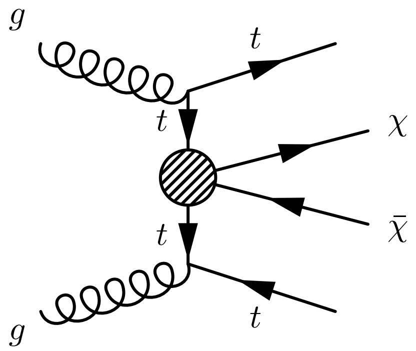

Figure 6.7: Feynman diagrams describing the dominant mechanism for the production of DM particles in association with a pair of top quarks assuming a contact interaction.

interaction is parametrized through effective operators.

In this analysis, the DM is assumed to be a Dirac fermion χ and to be produced through a scalar interaction described by the EFT Lagrangian [173]:

$$L_{int} = \sum_q \frac{m_q}{M_*^3} \bar{q} q \bar{\chi} \chi \tag{6.5}$$

where the sum is extended over all quark types q. From Eq. 6.5, it is deduced that the m_q term suppresses couplings to light quarks and favour couplings to top quarks.

Figure 6.7 shows the dominant mechanism for the production of DM particles in association with two top quarks via the scalar interactions.

Limitations

The EFT approach is valid if the energy at which the interaction takes place is small with respect to the energy scale of the mediator. If such condition is not satisfied the mediator has to be considered explicitly in the process. This condition can also be expressed requiring that the momentum transfer Q_{tr} in the process is smaller than the energy scale M_*. This implies that the results obtained from EFTs will be less precise as Q_{tr} tends to M_*. The validity conditions depend on M_*, which is completely defined only by the details of the new physics process approximated by the EFT.

The following discussion on the validity of EFT results is based on [175]. Another presentation of its limitation can be found in [176].

As an example, let's consider an heavy scalar mediator of mass M and coupling g_χ and g_t to DM particles and top quarks, respectively. The EFT approximation corresponds to retaining only the lowest order operator of the propagator expansion:

$$\begin{aligned}\frac{g_\chi g_t}{Q_{tr}^2 - M^2} &= -\frac{g_\chi g_t}{M^2}\left(1 + \frac{Q_{tr}^2}{M^2} + \mathcal{O}\frac{Q_{tr}^4}{M^4}\right) \\ &\approx -\frac{g_\chi g_t}{M^2} & \text{for } Q_{tr}^2 << M^2\end{aligned}$$

The lowest order term, $g_\chi g_t/M^2$, has therefore to match the operator of the EFT Lagrangian, i.e.:

$$\frac{m_q}{M_*^3} = \frac{g_\chi g_t}{M^2}. \tag{6.6}$$

The condition of the perturbativity of the couplings and the kinematics impose respectively: $\sqrt{g_\chi g_t} < 4\pi$ and $M > 2m_\chi$. Including these constraints in Eq. 6.6 a *minimum requirement* on M_* for the EFT to be valid is obtained:

$$\sqrt{\frac{M_*^3}{m_q}} > \frac{m_\chi}{2\pi}. \tag{6.7}$$

If the more general condition $Q_{tr} < M$ is considered a more stringent condition on M_* for the validity of the results is imposed,

$$Q_{tr} < M$$

from Eq. 6.6 follows:

$$Q_{tr} < 4\pi\sqrt{M_*^3/m_t}$$

$$\sqrt{\frac{M_*^3}{m_q}} > \frac{M_{\chi\bar{\chi}}}{4\pi}. \tag{6.8}$$

where the Q_{tr} is estimated as the invariant mass $M_{\chi\bar{\chi}}$ of the two DM particles.

Signal predicted cross sections

The unknown masses of the DM particle and of the mediator are sampled for different hypotheses. The cross sections at LO for the EFT DM samples used in the 8 TeV analysis are listed in Table 6.4.

Samples (masses in GeV)	cross section (pb^{-1}) [$M_* = 100$ GeV]
$M_\chi = 1$	0.193
$M_\chi = 10$	0.189
$M_\chi = 50$	0.148
$M_\chi = 100$	0.104
$M_\chi = 200$	0.0528
$M_\chi = 600$	0.00267
$M_\chi = 1000$	0.000115

Table 6.4: Cross section at LO for the EFT DM samples used in the 8 TeV analysis.

6.3.2 Simplified models

The higher energies reached by the LHC in the run started in 2015, reduce the region of validity of the EFT. For this reason models where the mediator is considered explicitly are introduced.

In this analysis, a simplified model where the DM χ is assumed to be a Dirac fermion and the interaction is mediated by a massive electrically neutral scalar Φ or a pseudoscalar A particle is considered. The interactions are described by the following Lagrangians [60, 177]:

$$\mathcal{L}_\phi \supset g_\chi \phi \bar{\chi}\chi + \frac{\phi}{\sqrt{2}} \sum_{f=fermions} (g_v y_f \bar{f} f) \tag{6.9}$$

$$\mathcal{L}_A \supset i g_\chi A \bar{\chi}\gamma^5\chi + \frac{iA}{\sqrt{2}} \sum_{f=fermions} (g_v y_f \bar{f}\gamma^5 f) \tag{6.10}$$

where g_χ and g_v are the couplings of the mediator to the DM particles and fermions respectively, and $y_f = \sqrt{2}m_f/v$ are the Yukawa couplings where v is the Higgs field vacuum expectation value. The set of free parameters of such simplified model is $(m_\chi,\ m_\varphi,\ g_\chi,\ g_v)$, where m_φ is the mass of the scalar or pseudoscalar mediator φ. In this work, $g_\chi = g_v = 1$ is considered for all fermions and the width is set to its minimal value which is given by [60, 177]:

$$\begin{aligned}\Gamma_\varphi =& \frac{m_\varphi}{8\pi}\left(1 - \frac{4m_\chi^2}{m_\varphi^2}\right)^{n/2} \\ &+ \sum_{f=fermions} \frac{y_f^2 m_\varphi}{16\pi}\left(1 - \frac{4m_f^2}{m_\varphi^2}\right)^{n/2}\end{aligned} \tag{6.11}$$

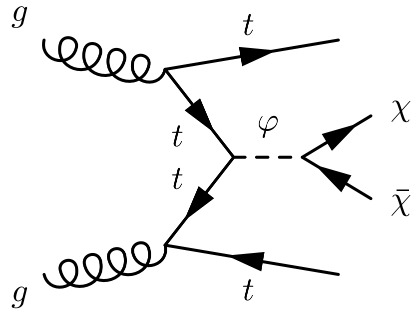

Figure 6.8: Feynman diagrams describing the dominant mechanism for the production of DM particles in association with a pair of top quarks assuming an explicit scalar or pseudoscalar mediator φ.

where $n = 3$ for scalars and $n = 1$ for pseudoscalars interactions, respectively.

For the energy accessible with the data collected in 2015, the choice of couplings and mediator width used does not affect the kinematic of the final state but only the predicted cross sections [60].

The dominant production mechanism for the production of tt+DM via scalar or pseudoscalar interaction is shown in Figure 6.8.

Signal production

To understand which signal models are important for DM searches at $\sqrt{s} = 13$ TeV, a DM Forum [60] formed by members of the CMS and ATLAS collaborations and of the theory community has been established. The model parameters are scanned to identify benchmark points such that the different kinematic features of DM events are sufficiently represented.

The final E_T^{miss} distribution is related to the mediator p_T spectrum and it changes with m_φ, but it does not depend on m_χ in the on-shell regime. This is shown in Figure 6.9 for the scalar and pseudoscalar hypotheses.

In Table 6.5 the LO cross sections for the simplified model samples used in the 13 TeV analysis are presented.

6.4 Limits on production cross-section

As shown in Tables 6.1 to 6.3, no excess of events over the expected SM background is observed in both analyses. Therefore, 95% CL upper limits on the signal strength for the 13 TeV analysis and 90% CL upper limits on the production cross section for the 8

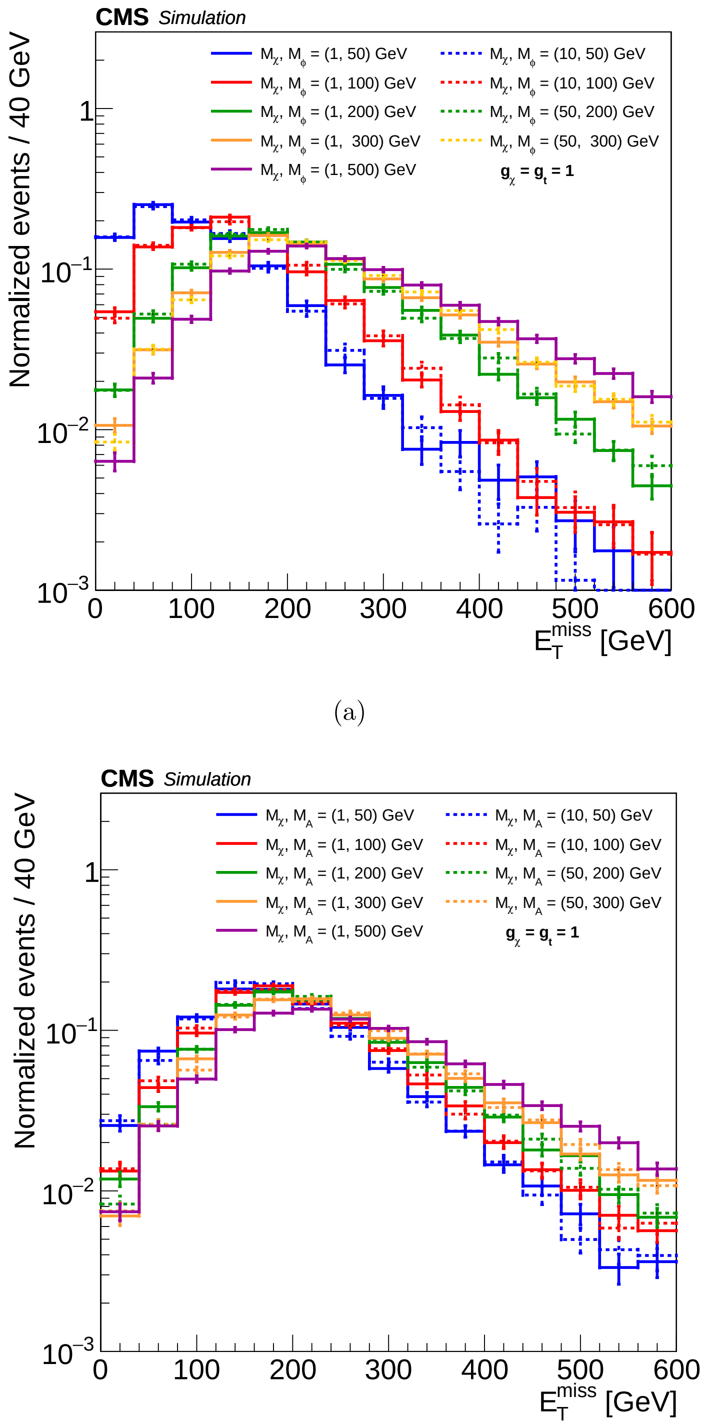

(a)

(b)

Figure 6.9: E_T^{miss} simulated distributions for different m_φ and m_χ hypothesis for the scalar (a) and pseudoscalar (b) scenarios. The distributions are shown without applying any selection.

Samples (masses in GeV)	cross section (pb^{-1})	Samples (masses in GeV)	cross section (pb^{-1})
$M_\phi = 10,\ M_\chi = 1$	19.59	$M_A = 10,\ M_\chi = 1$	0.4409
$M_\phi = 20,\ M_\chi = 1$	10.48	$M_A = 20,\ M_\chi = 1$	0.3992
$M_\phi = 50,\ M_\chi = 1$	2.941	$M_A = 50,\ M_\chi = 1$	0.3032
$M_\phi = 100,\ M_\chi = 1$	0.672	$M_A = 100,\ M_\chi = 1$	0.1909
$M_\phi = 200,\ M_\chi = 1$	$9.33 \cdot 10^{-2}$	$M_A = 200,\ M_\chi = 1$	$8.36 \cdot 10^{-2}$
$M_\phi = 300,\ M_\chi = 1$	$2.95 \cdot 10^{-2}$	$M_A = 300,\ M_\chi = 1$	$3.999 \cdot 10^{-2}$
$M_\phi = 500,\ M_\chi = 1$	$5.18 \cdot 10^{-3}$	$M_A = 500,\ M_\chi = 1$	$5.41 \cdot 10^{-3}$
$M_\phi = 10,\ M_\chi = 10$	$9.49 \cdot 10^{-2}$	$M_A = 10,\ M_\chi = 10$	$1.499 \cdot 10^{-2}$
$M_\phi = 50,\ M_\chi = 10$	2.942	$M_A = 50,\ M_\chi = 10$	0.303
$M_\phi = 100,\ M_\chi = 10$	$0.673 \cdot 10^{-2}$	$M_A = 100,\ M_\chi = 10$	0.1901
$M_\phi = 50,\ M_\chi = 50$	$2.33 \cdot 10^{-3}$	$M_A = 50,\ M_\chi = 50$	$2.979 \cdot 10^{-3}$
$M_\phi = 200,\ M_\chi = 50$	$9.22 \cdot 10^{-2}$	$M_A = 200,\ M_\chi = 50$	$8.38 \cdot 10^{-2}$
$M_\phi = 300,\ M_\chi = 50$	$2.90 \cdot 10^{-2}$	$M_A = 300,\ M_\chi = 50$	$3.989 \cdot 10^{-2}$
$M_\phi = 200,\ M_\chi = 150$	$1.300 \cdot 10^{-4}$	$M_A = 200,\ M_\chi = 150$	$4.12 \cdot 10^{-4}$
$M_\phi = 500,\ M_\chi = 150$	$3.75 \cdot 10^{-3}$	$M_A = 500,\ M_\chi = 150$	$4.61 \cdot 10^{-3}$

Table 6.5: Cross section at LO for the simplified model DM samples used in the 13 TeV analysis.

TeV are set. The choice of 90% CL for the 8 TeV analysis allows an easier comparison with the related results from direct and indirect DM experiments.

6.4.1 Effective field theories

In Table 6.6 the expected number of signal events for different DM hypotheses and $M_* = 100$ GeV are listed. The signal efficiency, expected and observed limits on the tt+DM production cross section are also presented. The efficiencies for the signal are below 3% because of the tight requirement $E_T^{miss} > 320$ GeV used to identify the SR. From Table 6.6, it follows that cross sections larger than 55 to 20 fb are excluded at 90% CL for a DM particle with mass in the range 1-1000 GeV.

Upper limits on the tt+DM production cross section can be translated in lower limits for the parameter M_* of the associated EFT. The lower limits on M_* are shown for different DM mass hypotheses in Figure 6.10.

The validity conditions for the EFT results to be valid are taken into account. The minimal requirement, corresponding to Equation 6.7, is shown in Figure 6.10 by the upper edge of the grey hatched area. The fraction R corresponding to 80% and 50% of simulated events satisfying the tighter condition of Equation 6.8 are represented by the coloured lines for two different hypothesis on $\sqrt{g_\chi g_t}$, namely $\sqrt{g_\chi g_t} = 4\pi$ and $\sqrt{g_\chi g_t} = 2\pi$. If M_* is fixed to the value obtained by the lower limits contours, 86%

(46%) of the simulated signal events satisfy Equation 6.8 for $\sqrt{g_\chi g_t} = 4\pi$ (2π) and $m_\chi = 1$ GeV.

M_χ (GeV)	Yield (±stat ±syst)	Signal efficiency (%) (±stat ±syst)	$\sigma^{\text{lim}}{}_{\text{exp}}$ (fb)	$\sigma^{\text{lim}}_{\text{obs}}$ (fb)
1	$38.3 \pm 0.7 \pm 2.1$	$1.01 \pm 0.02 \pm 0.05$	47^{+21}_{-13}	55
10	$37.8 \pm 0.7 \pm 2.1$	$1.01 \pm 0.02 \pm 0.05$	46^{+21}_{-13}	54
50	$35.1 \pm 0.6 \pm 1.9$	$1.20 \pm 0.02 \pm 0.06$	39^{+18}_{-11}	45
100	$30.1 \pm 0.4 \pm 1.7$	$1.46 \pm 0.02 \pm 0.07$	32^{+14}_{-9}	37
200	$18.0 \pm 0.2 \pm 1.0$	$1.73 \pm 0.02 \pm 0.08$	27^{+12}_{-8}	32
600	$1.26 \pm 0.02 \pm 0.07$	$2.40 \pm 0.03 \pm 0.11$	19^{+9}_{-6}	23
1000	$0.062 \pm 0.001 \pm 0.003$	$2.76 \pm 0.04 \pm 0.13$	17^{+8}_{-5}	20

Table 6.6: Observed data yield and number of expected SM events in SR after the $t\bar{t}$ and W+jets SFs are applied. The data presented were recorded at $\sqrt{s} = 8$ TeV and corresponds to an integrated luminosity of 2.2 fb^{-1}. The uncertainties associated with the expected SM yields are also presented.

The limits obtained for M_* on the production cross section can also be presented in terms of DM-nucleon scattering cross section $\sigma_{(DM-nucl.)}$ using the formula [58]:

$$\sigma_{(DM-nucl.)} = 1.6 \cdot 10^{-37} \left(\frac{\mu_\chi}{1\text{GeV}}\right)^2 \left(\frac{20\text{GeV}}{M_*}\right)^6 \text{cm}^2$$

where μ_χ is the reduced mass of the DM-nucleon system.

This allows a comparison with results from direct and indirect searches for spin independent interactions, as shown in Figure 6.11. Under the hypothesis that only the scalar interaction is responsible for the DM-nucleon scattering, more stringent limits are obtained in the mass region $m_\chi < 6$ GeV from the results of the presented analysis with respect to the direct searches. DM-nucleon cross sections larger than $1 - 2 \cdot 10^{-42}\text{cm}^2$ are excluded in the mentioned region.

6.4.2 Simplified models

In Table 6.7 the expected signal yields in the single lepton and hadronic SRs are listed for different hypotheses on the mediator mass and $m_\chi = 1$ GeV, as well as on the interaction type.

The signal efficiency in SR for a pseudoscalar or a scalar mediator are shown in Figure 6.12. The efficiencies are below or close to 1% for $m_\chi < 50$ GeV and $M_\varphi < 50$ GeV because of the E_T^{miss} requirement used to identify the hadronic and single lepton SRs.

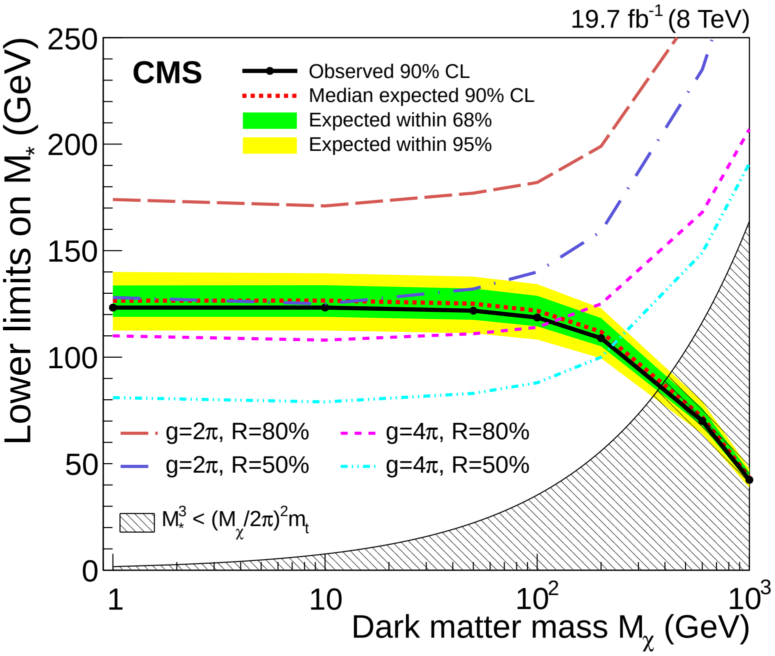

Figure 6.10: Observed and expected exclusion limits in the plane of m_χ and M_*, with the region below the solid curve excluded at a 90% CL. The background-only expectations are represented by their median (dashed ref line) and by the 68% and 95% CL bands. The minimal requirement on the EFT validity (Equation 6.7) is shown by the upper edge of the grey hatched area. The fraction R corresponding to 80% and 50% of simulated events satisfying the tighter condition of Equation 6.8 are represented by the coloured lines for two different hypothesis on $\sqrt{g_\chi g_t}$, namely$\sqrt{g_\chi g_t} = 4\pi$ and $\sqrt{g_\chi g_t} = 2\pi$.

Samples	Yields	
(masses in GeV)	single lepton SR	hadronic SR
$M_\phi = 10,\ M_\chi = 1$	9.1 ± 4.3	20 ± 12
$M_\phi = 100,\ M_\chi = 1$	4.64 ± 0.56	10.0 ± 3.0
$M_A = 100,\ M_\chi = 1$	4.36 ± 0.29	8.5 ± 1.4

Table 6.7: Expected signal yields with $2.2 fb^{-1}$ of data in the SR of the hadronic and single lepton channels. The reported errors include only statistical uncertainties.

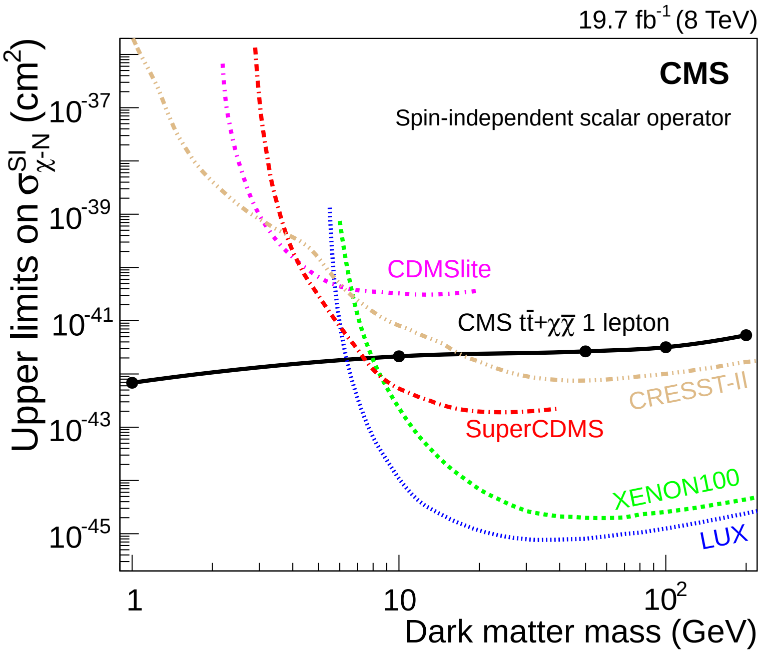

Figure 6.11: The 90% CL upper limits on the DM-nucleon cross sections are presented as a function of the dark matter mass for spin-independent scattering. The 90% CL limits from selected experiments [178–182] with published results by the time of the 8 TeV analysis result are shown for comparison.

m_ϕ, m_χ (GeV)	Obs.	Exp.	$[-1\sigma,\ +1\sigma]$	$[-2\sigma,\ +2\sigma]$	m_A, m_χ (GeV)	Obs.	Exp.	$[-1\sigma,\ +1\sigma]$	$[-2\sigma,\ +2\sigma]$
10, 1	2.7	1.9	[1.1, 3.5]	[0.7, 5.7]	10, 1	3.9	3.4	[2.3, 5.3]	[1.6, 8.0]
20, 1	1.8	1.6	[1.0, 2.6]	[0.7, 4.2]	20, 1	3.4	2.9	[2.0, 4.5]	[1.4, 6.6]
50, 1	1.8	2.0	[1.3, 3.2]	[0.94, 5.1]	50, 1	3.2	2.8	[1.9, 4.2]	[1.4, 6.2]
100, 1	5.3	4.1	[2.7, 6.4]	[1.9, 9.8]	100, 1	3.9	3.9	[2.6, 5.8]	[1.9, 8.7]
200, 1	8.4	7.5	[5.1, 11]	[3.7, 16]	200, 1	6.4	6.0	[4.1, 9.2]	[3.0, 14]
300, 1	14	14	[9.3, 21]	[6.7, 30]	300, 1	10	10	[6.9, 15]	[5.0, 23]
500, 1	54	57	[39, 88]	[28, 130]	500, 1	54	55	[37, 84]	[27, 130]
10, 10	69	60	[40, 97]	[28, 150]	10, 10	75	62	[42, 95]	[31, 140]
50, 10	11	3.3	[2.1, 5.4]	[1.5, 8.8]	50, 10	4.4	3.5	[2.4, 5.2]	[1.7, 7.6]
100, 10	4.7	3.8	[2.6, 5.8]	[1.9, 8.6]	100, 10	-	-	[–, –]	[–, –]
50, 50	180	170	[120, 260]	[84, 380]	50, 50	370	350	[240, 540]	[170, 810]
200, 50	8.2	7.4	[5.0, 11]	[3.6, 16]	200, 50	6.2	5.5	[3.7, 8.2]	[2.7, 12]
300, 50	16	15	[10, 23]	[7.3, 34]	300, 50	9.7	9.5	[6.5, 14]	[4.7, 21]
200, 150	-	-	[–, –]	[–, –]	200, 150	720	750	[500, 1200]	[360, 1800]
500, 150	-	-	[–, –]	[–, –]	500, 150	57	60	[41, 92]	[29, 140]

Table 6.8: Expected and observed upper limits at 95% CL on μ_s as a function of scalar (pseudoscalar) mediator and DM masses in the single lepton channel combined.

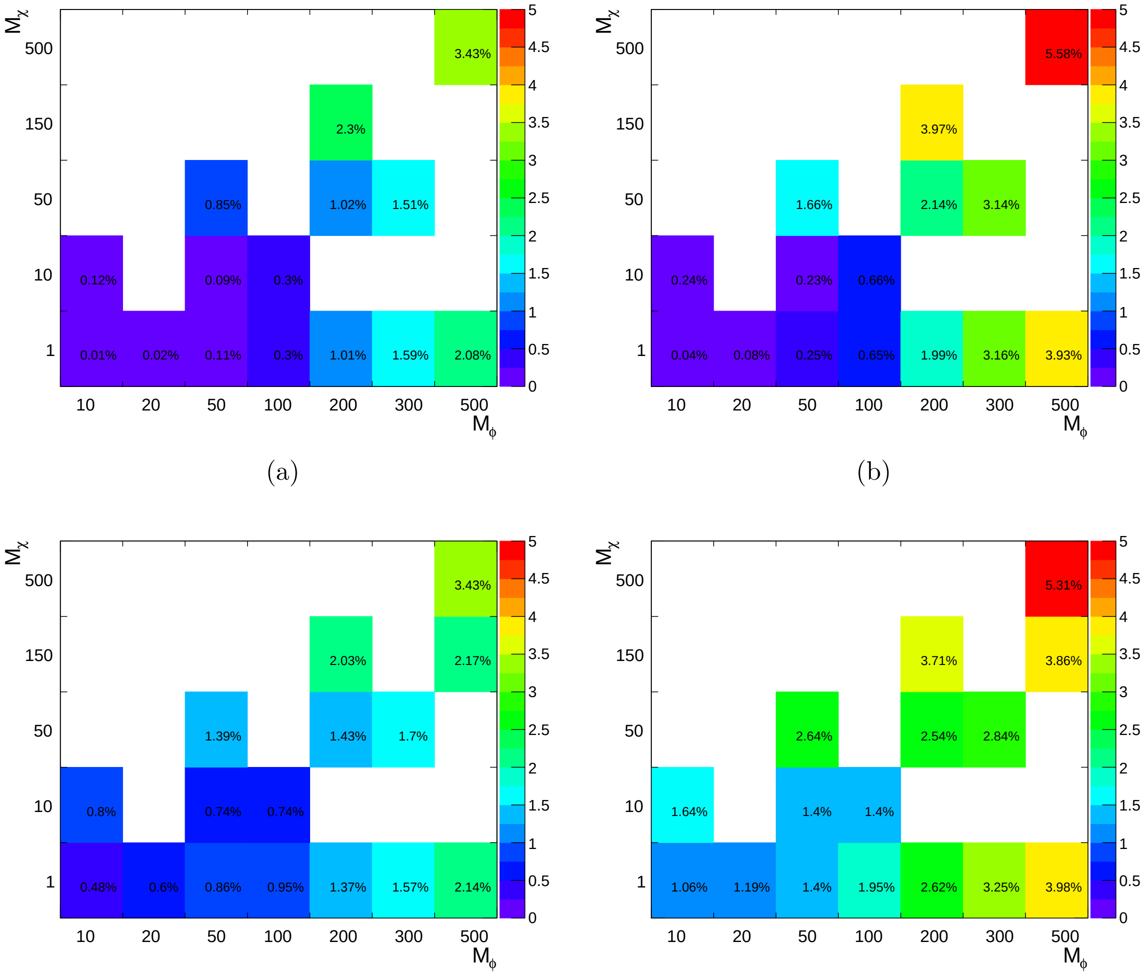

(a) (b)

(c) (d)

Figure 6.12: Signal efficiency as evaluated in the single lepton (a, b) and in the hadronic SR (c, d) for the scalar (a, c) and pseudoscalar (b, d) mediator hypothesis.

m_ϕ, m_χ (GeV)	Obs.	Exp.	$[-1\sigma,\ +1\sigma]$	$[-2\sigma,\ +2\sigma]$	m_A, m_χ (GeV)	Obs.	Exp.	$[-1\sigma,\ +1\sigma]$	$[-2\sigma,\ +2\sigma]$
10, 1	2.0	1.7	[1.1, 2.8]	[0.79, 4.5]	10, 1	4.0	3.9	[2.6, 6.0]	[1.9, 9.1]
20, 1	3.0	2.2	[1.4, 3.6]	[0.98, 5.6]	20, 1	3.5	4.2	[2.9, 6.5]	[2.1, 9.7]
50, 1	4.4	2.8	[1.9, 4.4]	[1.3, 6.6]	50, 1	3.9	4.5	[3.1, 6.7]	[2.2, 9.8]
100, 1	5.6	5.3	[3.6, 8.2]	[2.6, 12]	100, 1	3.9	4.5	[3.1, 6.8]	[2.2, 10]
200, 1	7.0	9.0	[6.1, 13]	[4.5, 20]	200, 1	5.7	6.7	[4.5, 10]	[3.2, 15]
300, 1	10	14	[9.6, 21]	[6.9, 32]	300, 1	7.4	9.5	[6.5, 15]	[4.7, 22]
500, 1	40	55	[37, 85]	[27, 130]	500, 1	41	56	[38, 87]	[27, 130]
10, 10	100	93	[61, 150]	[44, 230]	10, 10	78	76	[52, 110]	[37, 170]
50, 10	2.9	2.6	[1.7, 4.2]	[1.2, 6.7]	50, 10	4.1	4.1	[2.8, 6.3]	[2.0, 9.3]
100, 10	6.7	5.7	[4.0, 8.5]	[2.9, 12]	100, 10	-	-	[−, −]	[−, −]
50, 50	310	400	[270, 610]	[190, 910]	50, 50	-	-	[−, −]	[−, −]
200, 50	7.9	8.8	[6.1, 13]	[4.4, 19]	200, 50	5.8	6.8	[4.6, 10]	[3.3, 16]
300, 50	9.1	14	[9.2, 21]	[6.6, 31]	300, 50	9.4	12	[7.9, 18]	[5.7, 27]
200, 150	-	-	[−, −]	[−, −]	200, 150	650	850	[570, 1300]	[410, 2000]

Table 6.9: Expected and observed upper limits at 95% CL on μ_s as a function of scalar (pseudoscalar) mediator and DM masses in the hadronic channel combined.

m_ϕ, m_χ (GeV)	Obs.	Exp.	$[-1\sigma,\ +1\sigma]$	$[-2\sigma,\ +2\sigma]$	m_A, m_χ (GeV)	Obs.	Exp.	$[-1\sigma,\ +1\sigma]$	$[-2\sigma,\ +2\sigma]$
10, 1	1.2	1.1	[0.69, 1.8]	[0.48, 2.9]	10, 1	2.9	2.4	[1.6, 3.6]	[1.2, 5.3]
20, 1	1.7	1.2	[0.77, 1.9]	[0.55, 2.9]	20, 1	2.5	2.3	[1.5, 3.4]	[1.1, 5.0]
50, 1	2.0	1.5	[1.0, 2.3]	[0.74, 3.5]	50, 1	2.5	2.2	[1.6, 3.3]	[1.1, 4.8]
100, 1	3.8	2.9	[2.0, 4.4]	[1.4, 6.5]	100, 1	2.8	2.8	[1.9, 4.1]	[1.4, 6.0]
200, 1	5.5	5.5	[3.8, 8.1]	[2.7, 12]	200, 1	4.3	4.2	[2.9, 6.4]	[2.1, 9.4]
300, 1	8.2	9.4	[6.4, 14]	[4.7, 20]	300, 1	6.0	6.6	[4.5, 10.0]	[3.3, 15]
500, 1	32	38	[26, 58]	[19, 86]	500, 1	32	37	[25, 57]	[18, 85]
10, 10	56	48	[32, 73]	[23, 110]	10, 10	57	45	[31, 67]	[23, 98]
50, 10	4.6	1.9	[1.2, 2.9]	[0.89, 4.5]	50, 10	3.3	2.6	[1.8, 3.8]	[1.3, 5.5]
100, 10	4.2	3.0	[2.1, 4.4]	[1.5, 6.4]	100, 10	-	-	[−, −]	[−, −]
50, 50	230	250	[170, 370]	[120, 550]	50, 50	-	-	[−, −]	[−, −]
200, 50	6.0	5.4	[3.7, 8.0]	[2.7, 12]	200, 50	4.4	4.0	[2.8, 6.0]	[2.0, 8.7]
300, 50	7.9	9.6	[6.6, 14]	[4.8, 21]	300, 50	6.7	7.0	[4.8, 11]	[3.5, 15]
200, 150	1200	1400	[950, 2100]	[690, 3200]	200, 150	470	530	[360, 820]	[260, 1200]

Table 6.10

Expected and observed 95% CL limits on μ_s are computed for the single lepton and hadronic channels separately and also for their combination. In Tables 6.8 to 6.10 the upper limits for various m_χ and M_φ values are listed. The limits obtained for the combination channel are shown graphically in Figure 6.13 assuming $m_\chi = 1$ GeV.

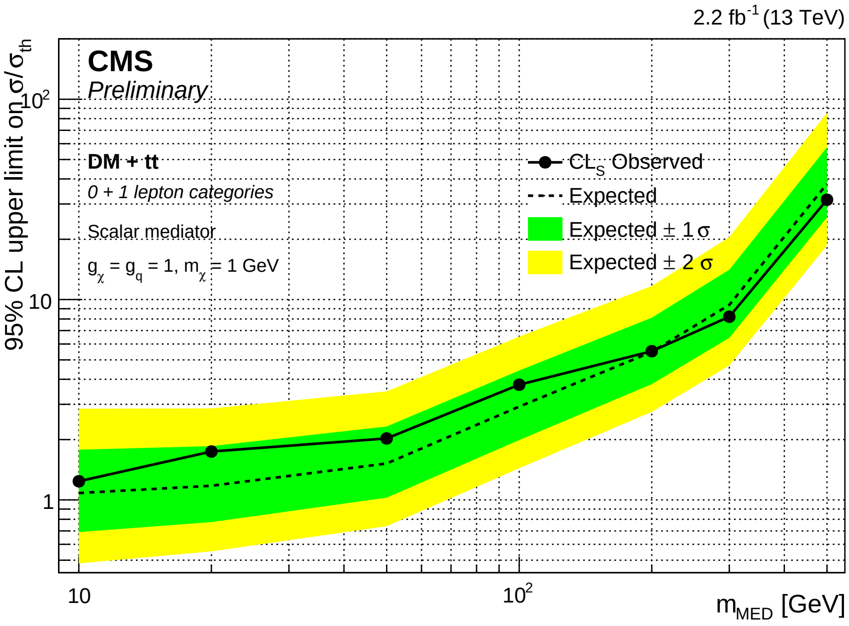

(a)

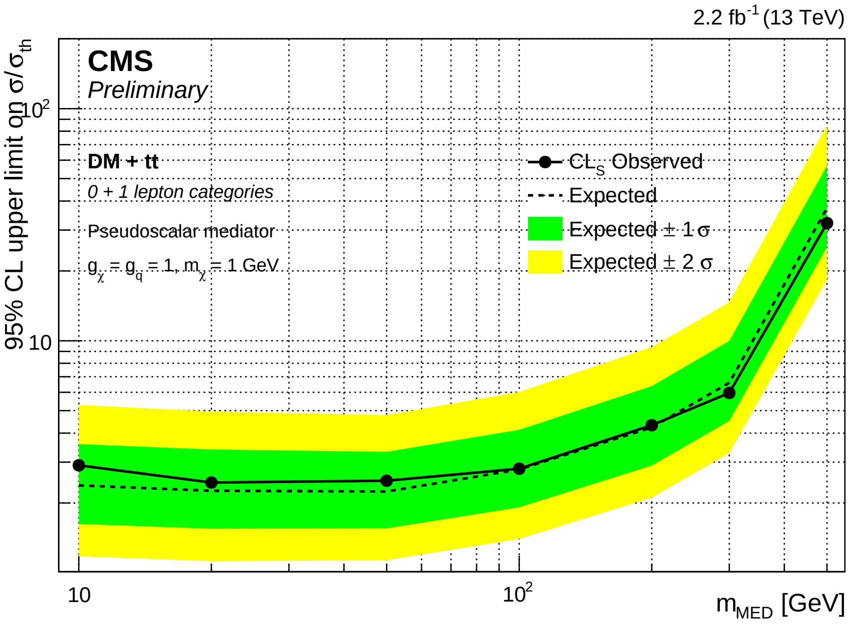

(b)

Figure 6.13: Expected and observed 95% CL upper limit on μ_s as a function of scalar (a) and pseudoscalar (b) mediator mass with single lepton and hadronic channels combined. A DM mass of 1 GeV is assumed.

Chapter 7

Dark matter at colliders: new prospects from single top quark

The simplified model used to describe tt+DM events (Section 6.3.2) also predicts processes in which the DM particles are produced in association with a single top quark ($t/\bar{t}$+DM). The dominant production mechanisms for $t/\bar{t}$+DM events via a scalar or a pseudoscalar mediator φ are shown in Figure 7.1. Similarly to the SM case, the production of the single top is obtained through processes mediated by virtual t-channel or s-channel W bosons, Figure 7.1(a) and (b) respectively, or through associated production with a W boson, Figure 7.1(c) and (d).

The $t/\bar{t}$+DM process has not been investigated yet at colliders. Similar signatures has been studied only via a flavour changing interaction or via the production of a new resonant particle that decays into a single top quark and a DM particle [183–185].

In the following sections, the sensitivity of the $t/\bar{t}$+DM channel to DM produced in scalar and pseudoscalar interactions is assessed. First the simulation setup used for these studies is presented, Section 7.1, and validated against the SR yields obtained from the tt+DM 13 TeV analysis. The kinematic features of $t/\bar{t}$+DM events are then presented in Section 7.2. In Section 7.3, the improvements on the signal strength limits obtained considering the $t/\bar{t}$+DM process in addition to tt+DM are presented.

7.1 Simulation of dark matter processes

In this study, DM events are simulated with Madgraph [140] at LO without additional partons in the hard scattering process. The showering and hadronization is then performed using the Pythia v6.428 [186] software.

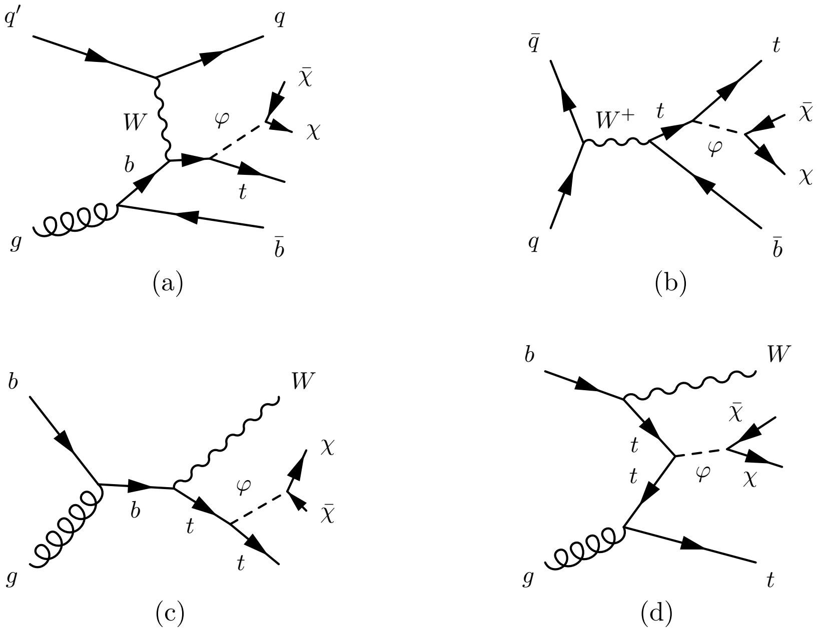

Figure 7.1: Feynman diagrams describing the associated production of DM particles with a single top quarks assuming an explicit scalar (ϕ) or pseudoscalar (A) mediator.

Simulated sample for tt+DM and $t/\bar{t}$+DM with the single top quark produced in association with a W boson (tW-channel) are generated in the 5-flavour scheme (Section 4.1.1). Events for $t/\bar{t}$+DM processes mediated by a virtual s-channel or t-channel W bosons are generated in the 4-flavour scheme. In the simulation of the hard scattering process, 200000 events are generated for tt+DM, s-channel and tW-channels $t/\bar{t}$+DM. This number is increased to 500000 for the t-channel $t/\bar{t}$+DM.

The related cross sections at generator level are calculated in the 5-flavour scheme for all processes. The results are presented in Table 7.1 for different hypotheses on the mediator and DM masses and graphically in Figure 7.2 for $m_\chi = 1$ GeV. It can be seen that the $t/\bar{t}$+DM cross sections range from about 20% to 140% of the tt+DM values, depending on the signal model assumed.

After the event generation, the response of the CMS detector is simulated using Delphes v3.3.3 [186] and the pileup conditions of the 2015 data-taking are reproduce generating on average 11 additional pp interactions.

To simulate the CMS performances on the reconstruction and identification of stable particles, jets are obtained using the $anti-k_T$ algorithm [126] with $R = 0.4$. For the Delphes simulation, the b-tagging efficiency is set to 60% and the mis-tagging probability to 35% and 1% for c- and light-jets, respectively. For electrons and muons the reconstruction and identification efficiencies are set to the values taken from [122]

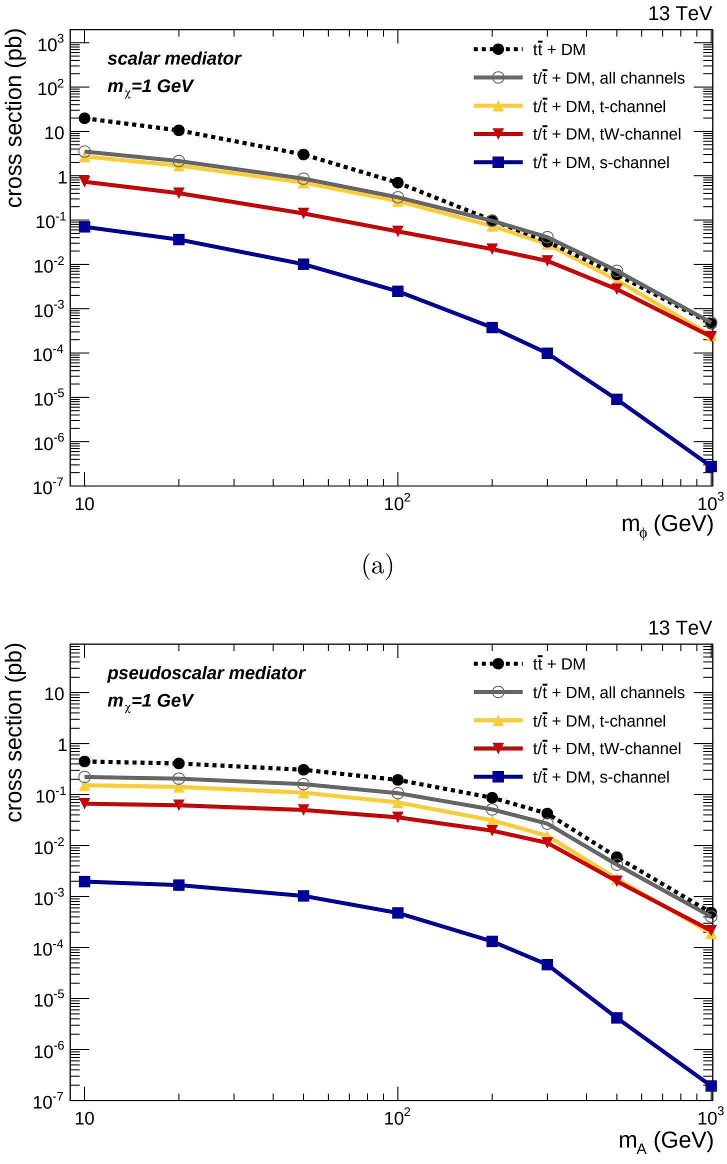

(a)

(b)

Figure 7.2: Cross sections of the $t/\bar{t}$+DM and tt+DM samples for different mediator masses and $m_\chi = 1$ GeV, for the scalar (a) or pseudoscalar (b) hypothesis. For the t+DM processes the cross sections are specified for the inclusive production as well as for each production mode (t-, s-, and tW-channels).

and [118] to reproduce the CMS response.

The selection of the single lepton and hadronic SRs, presented in Section 5.3.3, are applied to the tt+DM simulated samples and the final yields are compared with the signal yields obtained with the CMS analysis framework, as shown in Table 7.2. The two signal expectations are in good agreement within their statistical uncertainties, therefore the simulation described in this section (*private simulation* in the following) is validated.

7.2 Signal kinematic

The normalized spectra of the number of jets, b jets, and leptons for $t/\bar{t}$+DM and tt+DM processes are presented in Figure 7.3. It can be inferred that a dedicated selection for $t/\bar{t}$+DM processes should target lower jet and b jet multiplicities with respect to the selection used for the tt+DM analysis. For example, a requirement of ≥ 1 b-tagged jets individuate a phase space enriched in $t/\bar{t}$+DM events, which would also highly reduce one of the major backgrounds for the considered DM signal, i.e. tt processes. This phase space is not currently investigated in DM searches. For the purpose of the presented studies, the phase space defined by the tt+DM 13 TeV analysis SRs is nevertheless used to asses the sensitivity of the proposed $t/\bar{t}$+DM signal.

Despite the disadvantageous requirements on the jet and b jets multiplicities, the contributions from $t/\bar{t}$+DM events in 13 TeV analysis SRs is still high ($> 30\%$) with respect to tt+DM because of the E_T^{miss} requirement. In fact, the jet p_T and E_T^{miss} spectra for $t/\bar{t}$+DM peak at higher values with respect to tt+DM events if $M_\varphi \geq 100$ GeV. This is shown in Figure 7.4 assuming $M_\varphi = 500$ GeV and $m_\chi = 1$ GeV. The presented distributions are obtained after the requirements on the number of jets, b jets, and leptons used for the 13 TeV preselection, Section 5.3.2. For lower M_φ values the two spectra peak at the same value.

The number of expected events in the 13 TeV analysis SRs for the simulated $t/\bar{t}$+DM and tt+DM samples are presented in Table 7.3 and graphically in Figure 7.5. The related signal efficiencies are shown in Figures 7.6, 7.7 and 7.8, 7.9 for the single lepton and hadronic SRs respectively.

Although the $t/\bar{t}$+DM cross sections are generally smaller with respect to tt+DM, the kinematics of DM plus single top quark events yield sizable selection efficiency and yields in the SR. This is due to a combined effect of parton distribution functions and mass of the particles produced in the collisions. For example, when the initial partons

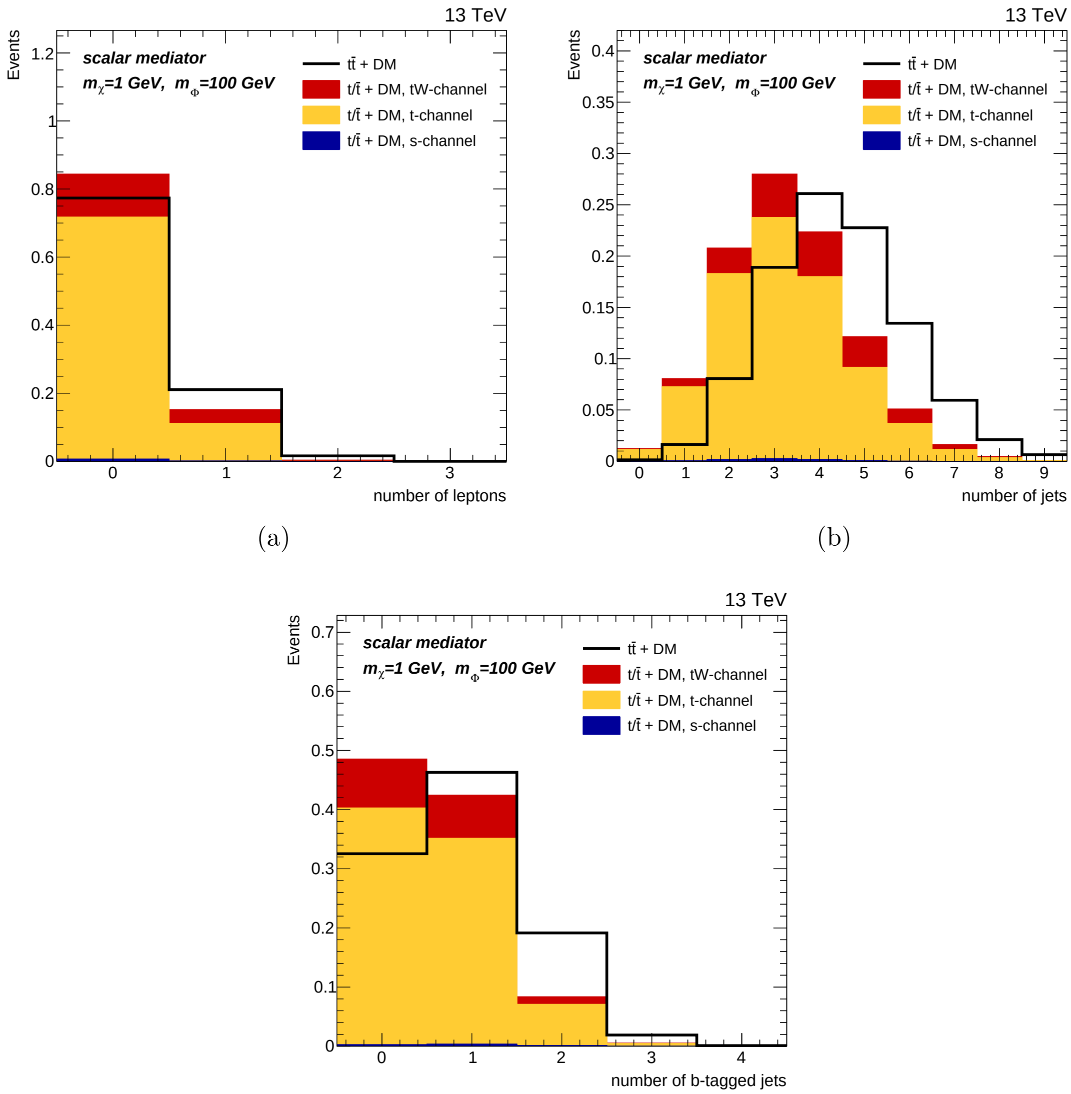

(a) (b)

(c)

Figure 7.3: Normalized distributions of the number of reconstructed leptons (a), jets (b), and b jets (c) with no selection applied for $m_\chi = 1$ GeV and $m_\phi = 100$ GeV. The solid black line shows the tt+DM process, while the solid histograms are stacked and show the contribution of the $t/\bar{t}$+DM processes (tW-channel, t-channel, and s-channel) weighted by the corresponding cross section.

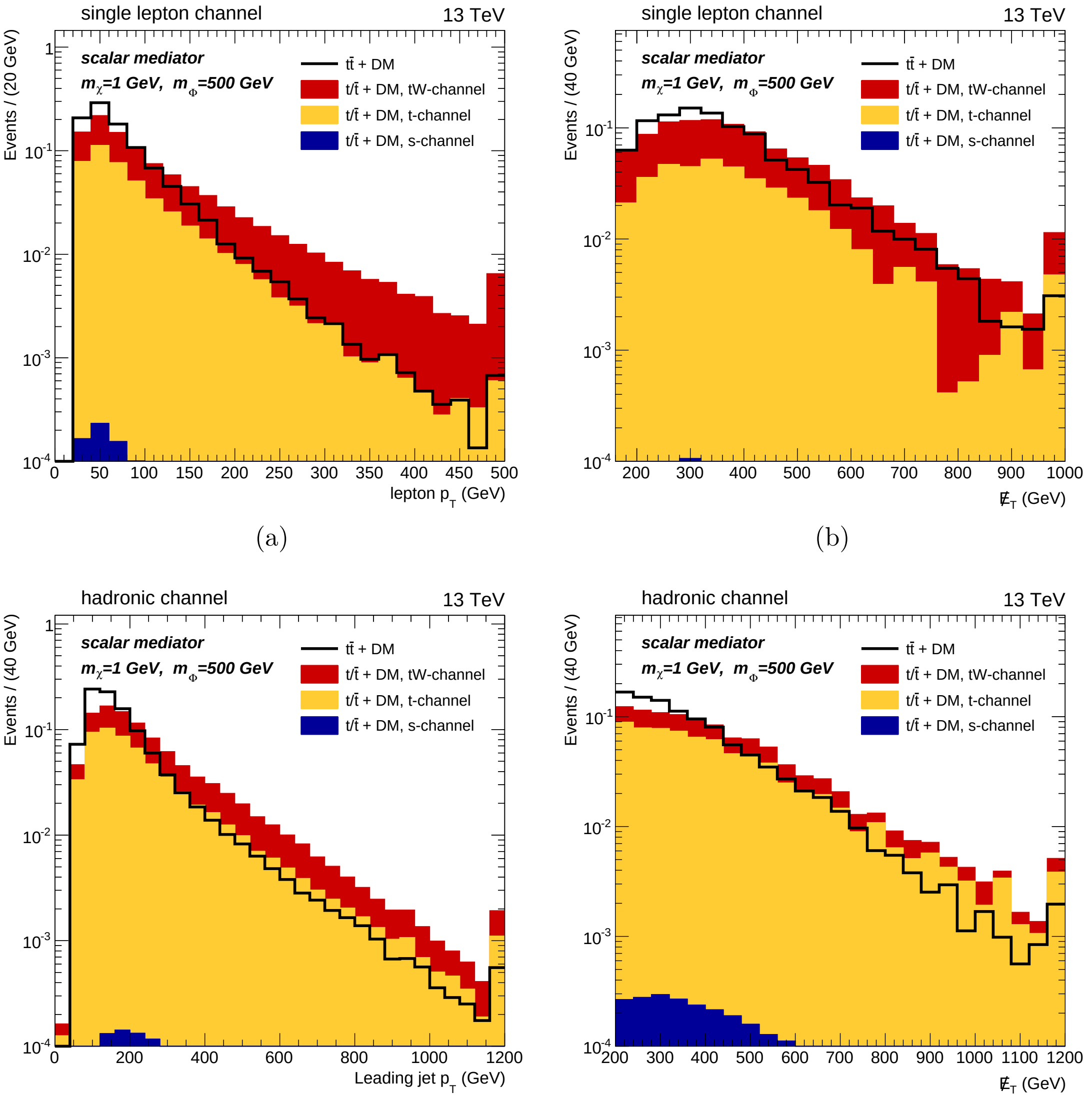

(a) (b)

(c) (d)

Figure 7.4: Normalized distributions of the number of reconstructed leptons (a), jets (b), and b jets (c) with no selection applied for m_χ = 1 GeV and m_ϕ = 100 GeV. The solid black line shows the tt+DM process, while the solid histograms are stacked and show the contribution of the $t/\bar{t}$+DM processes (tW-channel, t-channel, and s-channel) weighted by the corresponding cross section.

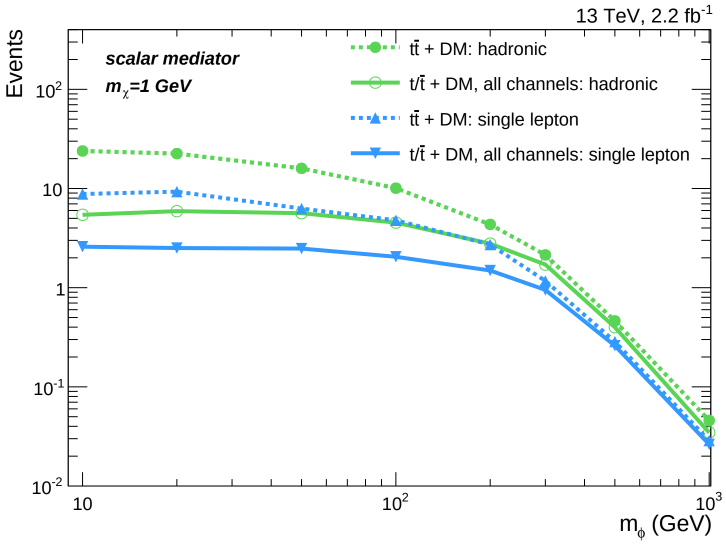

(a)

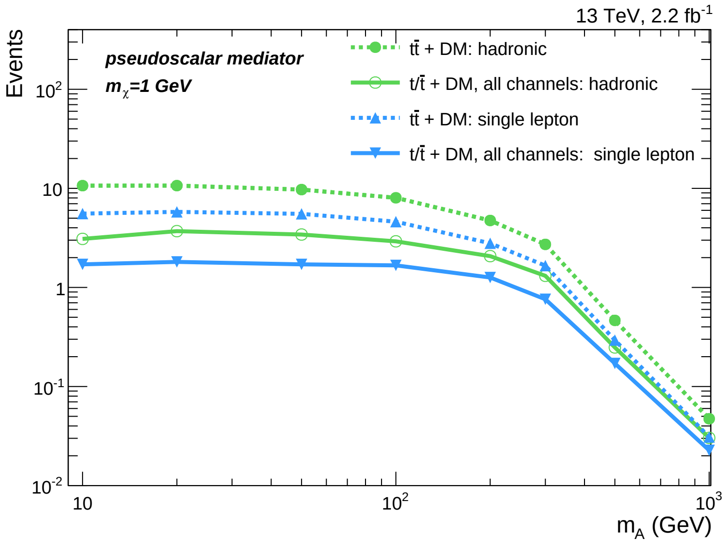

(b)

Figure 7.5: Expected signal events for scalar (a) and pseudoscalar (b) mediators for different M_φ mass hypotheses and $m_\chi = 1$ GeV obtained with the private simulation. The numerical values are referred to an integrated luminosity of 2.2 fb^{-1}, and are separated by process (tt+DM or the sum of $t/\bar{t}$+DM production channels) and final state (hadronic or single lepton).

carry higher energy fractions, the parton distribution functions present larger values for light quarks than for gluon [24]. Therefore, higher center-of-mass energies are achieved with larger probability in $t/\bar{t}$+DM t-channel processes than in tt+DM, translating in more energetic distributions for the p_T of the top quark in $t/\bar{t}$+DM t-channel events. The kinematic of $t/\bar{t}$+DM tW-channel processes is instead favoured by the lower energy required to produce a W boson instead of a top quark.

7.3 Limits improvements

The sensitivity of $t/\bar{t}$+DM processes is estimated calculating the improvements on the μ_s upper limits including $t/\bar{t}$+DM in addition to the tt+DM process.

The results are computed as CLs [168] upper limit, Section 6.1.2, on the signal strength. The number of expected and observed events in the single lepton and hadronic SRs are considered to extract the results. The observed data and the SM backgrounds yields, together with their relative uncertainties, are taken from Section 5.3.5. The number of expected $t/\bar{t}$+DM and tt+DM signal events are taken from the private simulation.

In Table 7.4, the expected and observed upper limits are listed. In Figure 7.10, scalar and pseudoscalar results are shown graphically for the combination of the single lepton and hadronic channels. The limits are presented as a function of M_φ assuming a DM particle of $m_\chi = 1$ GeV .

For low mediator masses ($M_\varphi < 100$ GeV) the results for the tt+DM process alone are 20% higher with respect to the 13 TeV analysis upper limits, Section 6.4.2. For these mediator masses the signal E_T^{miss} distribution is quite similar to that of the SM backgrounds. Therefore, small differences in the results are observed if the additional information from the shape of the distribution is included. For higher mediator masses the results from the 13 TeV analysis are about 50% better because the fit takes advantage from the E_T^{miss} distribution shape.

Considering the private simulation samples, it is observed that the inclusion of the $t/\bar{t}$+DM signal yields a relative improvement in the limit that ranges from 320% up to 90% depending on the mediator mass.

These results are also projected to the data collected by the CMS experiment during the year 2016, i.e. $\sim 35\text{fb}^{-1}$, and the integrated luminosity of 300fb^{-1} that should be available in 2023. For these studies, the uncertainties are assumed to scale as $\sqrt{\mathcal{L}}$. The predicted upper limits are presented in Figure 7.11. These results show that with the predicted luminosities, mediator masses up to 200 or 400 GeV, depending on the

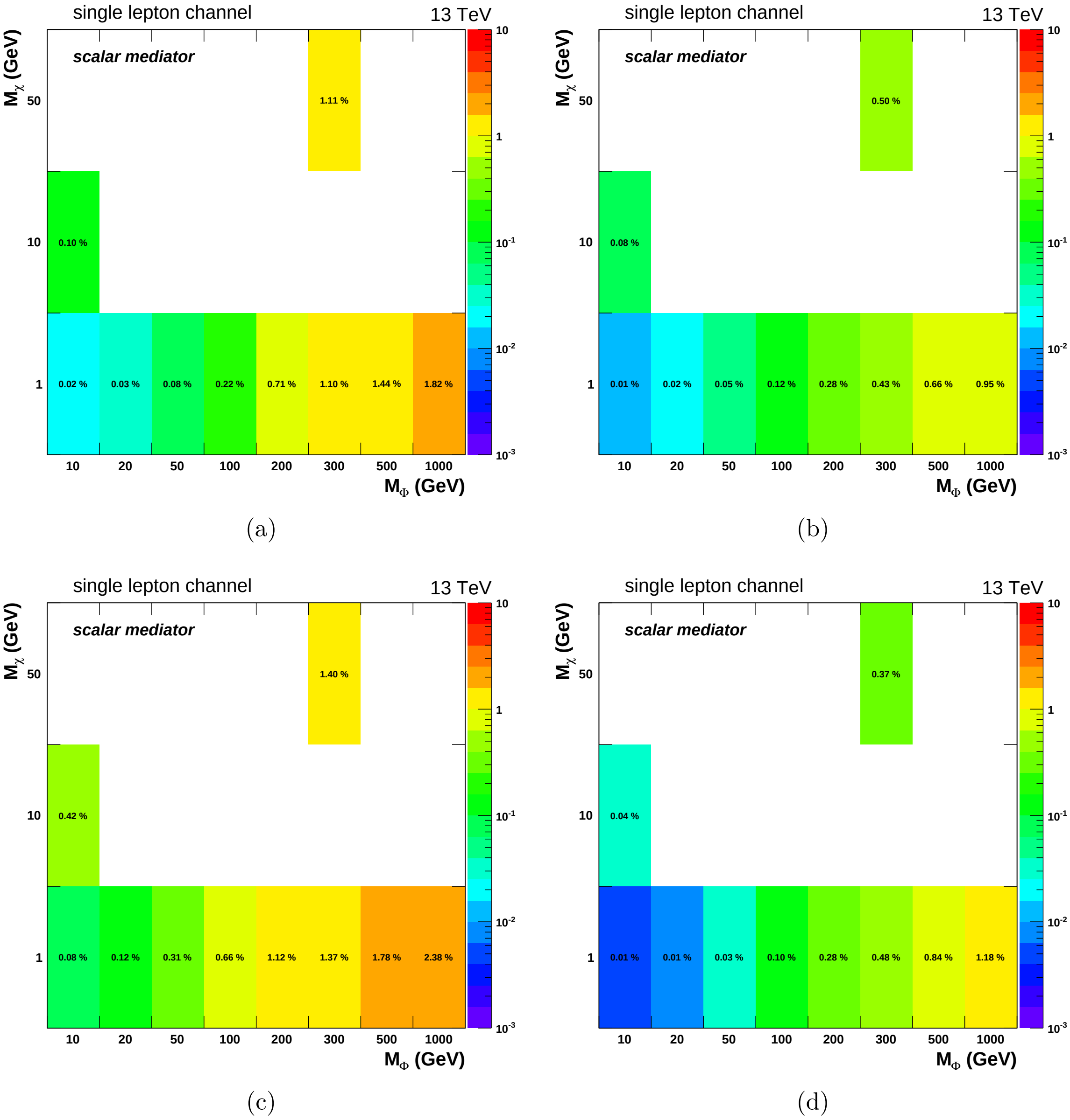

(a) (b)

(c) (d)

Figure 7.6: Signal efficiency as evaluated in the single lepton SR for the scalar mediator hypothesis for tt+DM (a) and t+DM t- (b), tW- (c), s-channels (d).

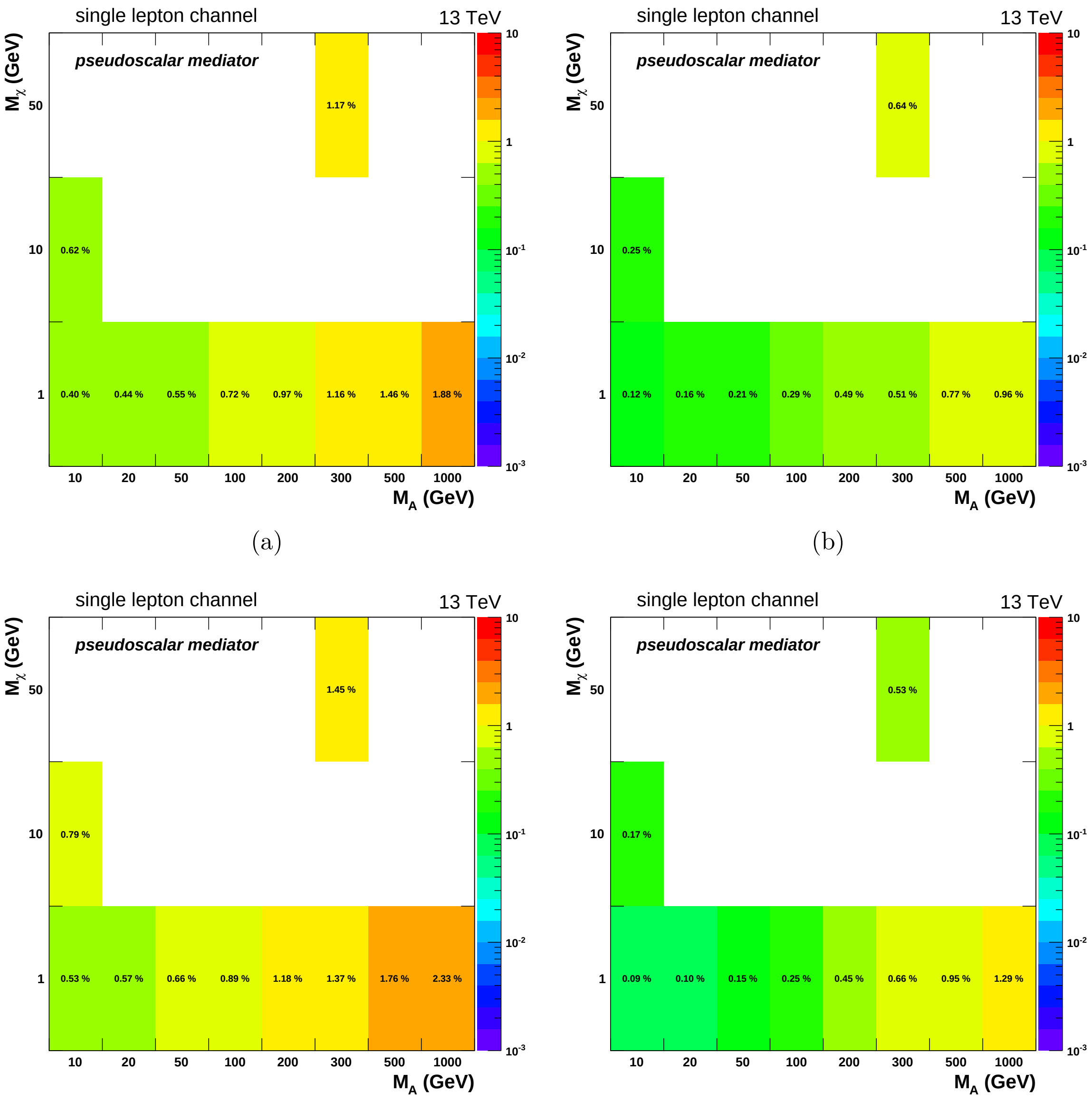

(a) (b)

(c) (d)

Figure 7.7: Signal efficiency as evaluated in the single lepton SR for the pseudoscalar mediator hypothesis for tt+DM (a) and t+DM t- (b), tW- (c), s-channels (d).

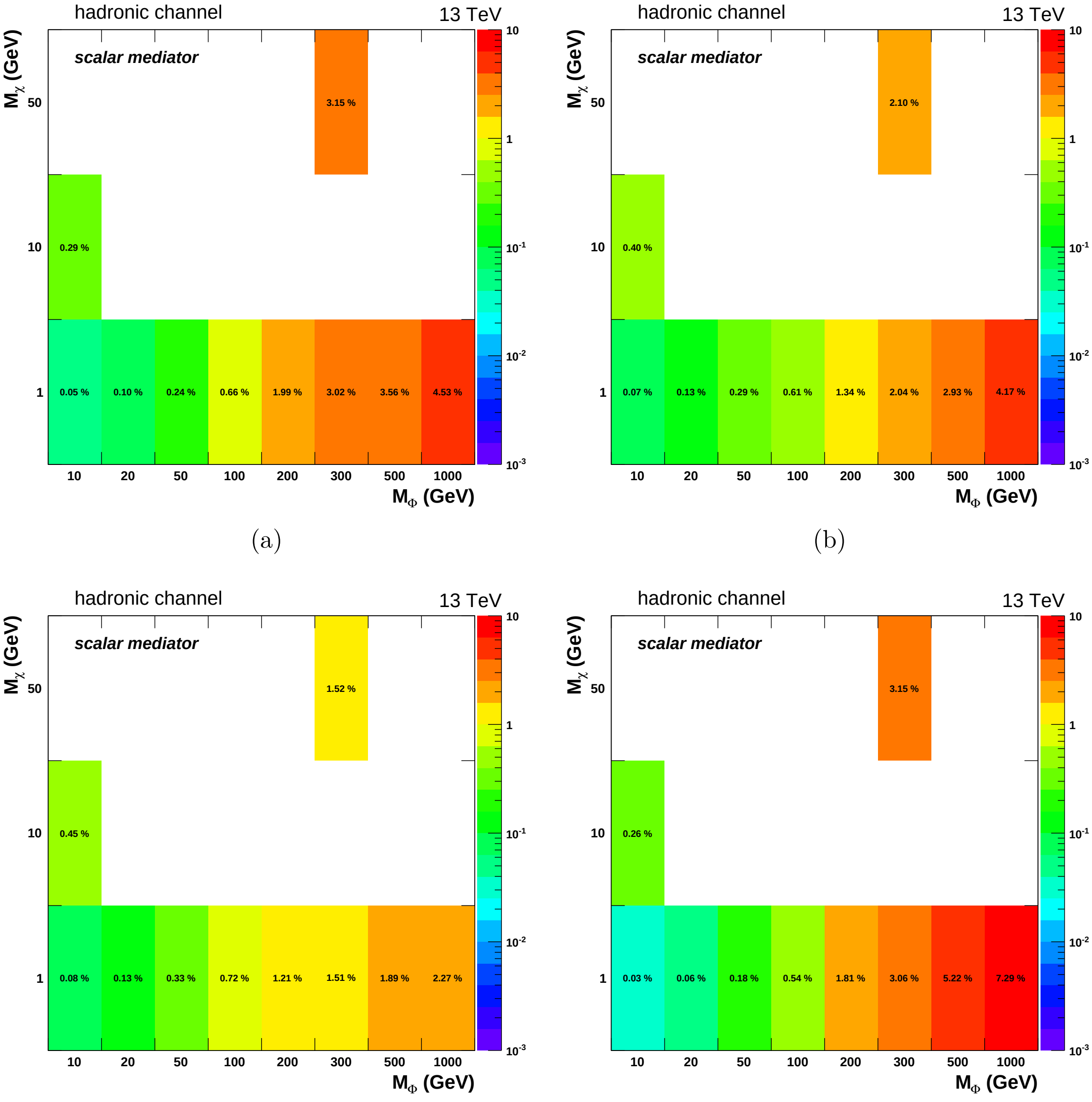

(a)

(b)

(c)

(d)

Figure 7.8: Signal efficiency as evaluated in the hadronic SR for the scalar mediator hypothesis for tt+DM (a) and t+DM t- (b), tW- (c), s-channels (d).

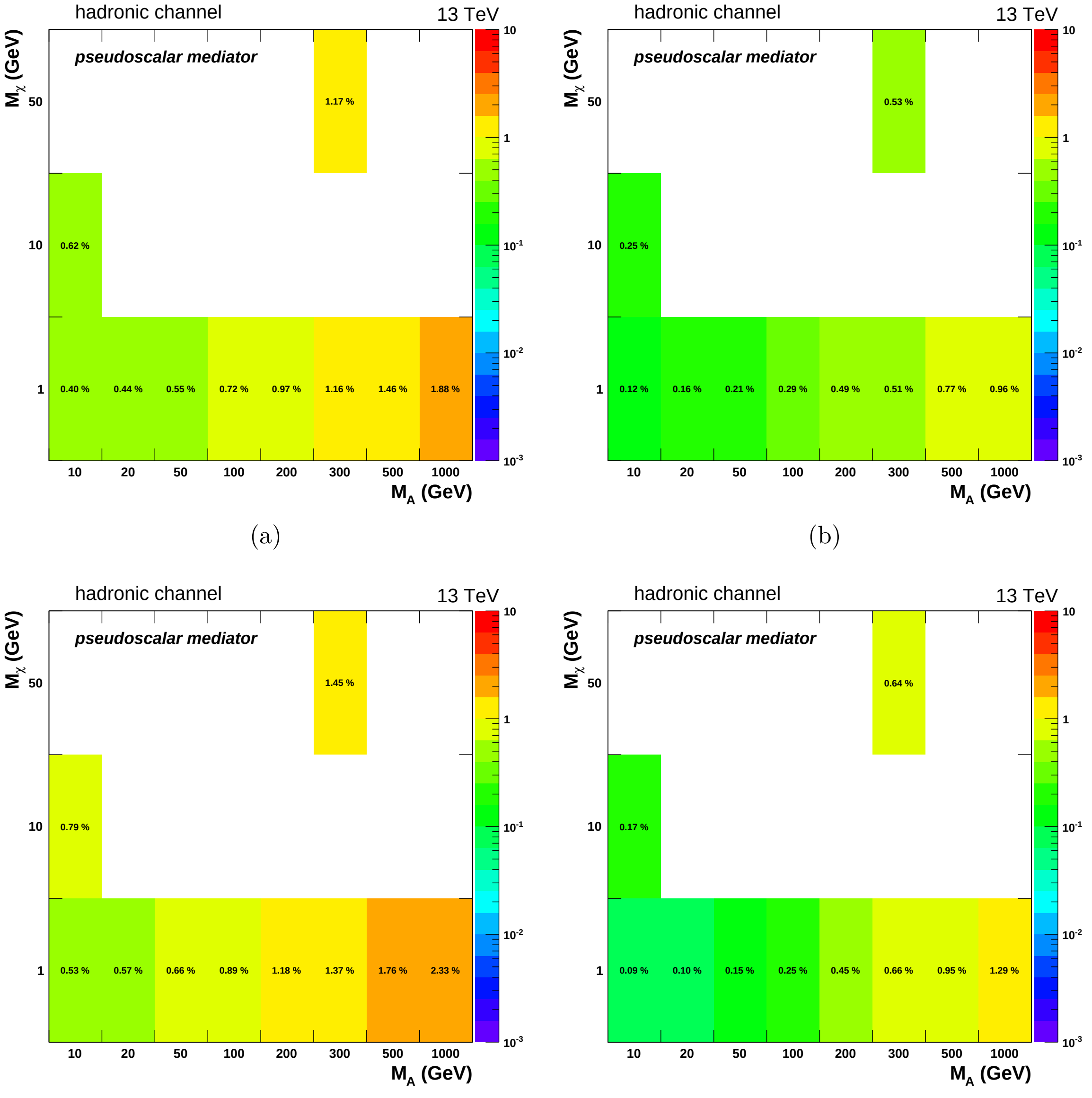

(a) (b) (c) (d)

Figure 7.9: Signal efficiency as evaluated in the hadronic SR for the pseudoscalar mediator hypothesis for tt+DM (a) and t+DM t- (b), tW- (c), s-channels (d).

luminosity considered, are within reach assuming $m_\chi = 1$ GeV and DM production cross sections as predicted from the theory model.

The presented studies show the important contribution of $t/\bar{t}$+DM processes for DM searches under the hypothesis of scalar or pseudoscalar interactions. Even higher improvements are foreseen for the associated production of DM with a single top developing an optimized selection targeting these processes.

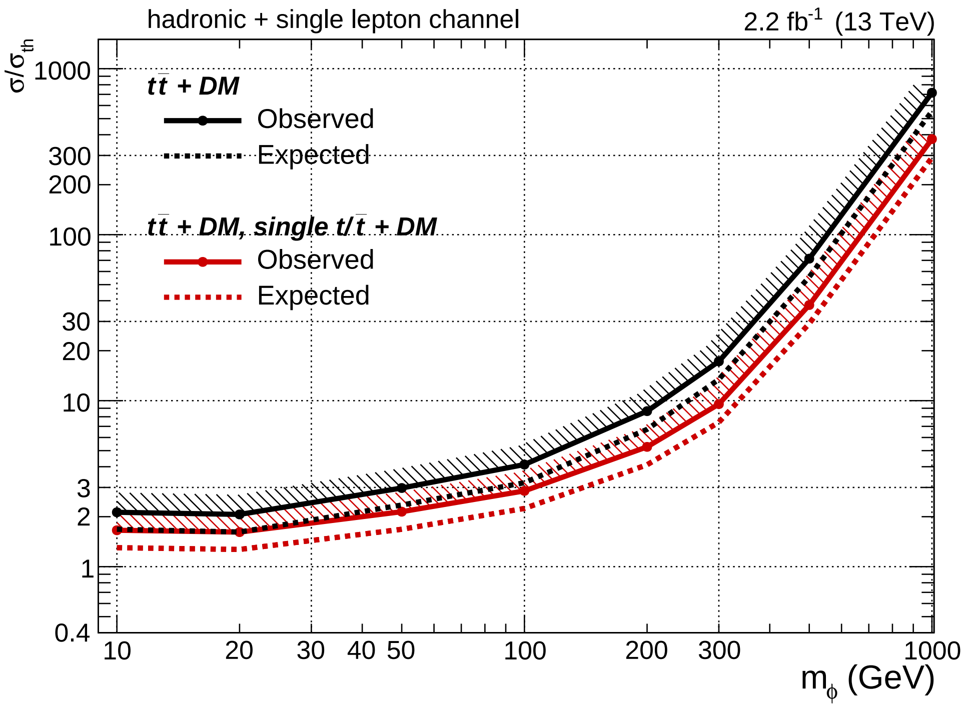

(a)

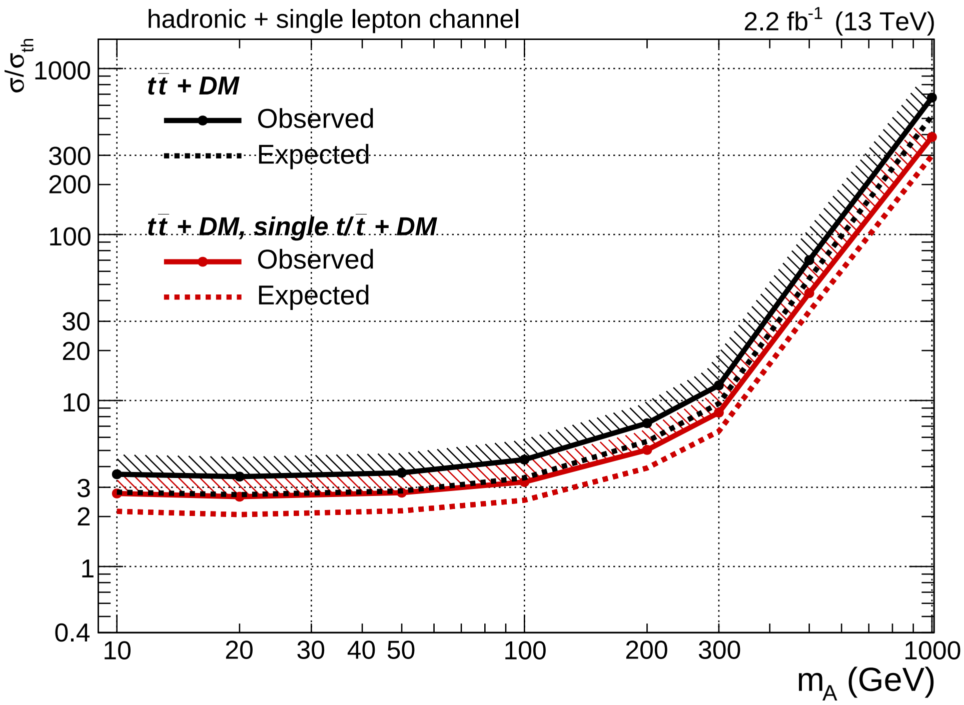

(b)

Figure 7.10: Expected and observed limits comparison between the tt+DM considered alone (black line) or together with the $t/\bar{t}$+DM process (red line). The limits are presented for the scalar (a) and pseudoscalar (b) mediator hypothesis. The region above the limit lines, indicated by the shaded areas, represents the excluded parameter space.

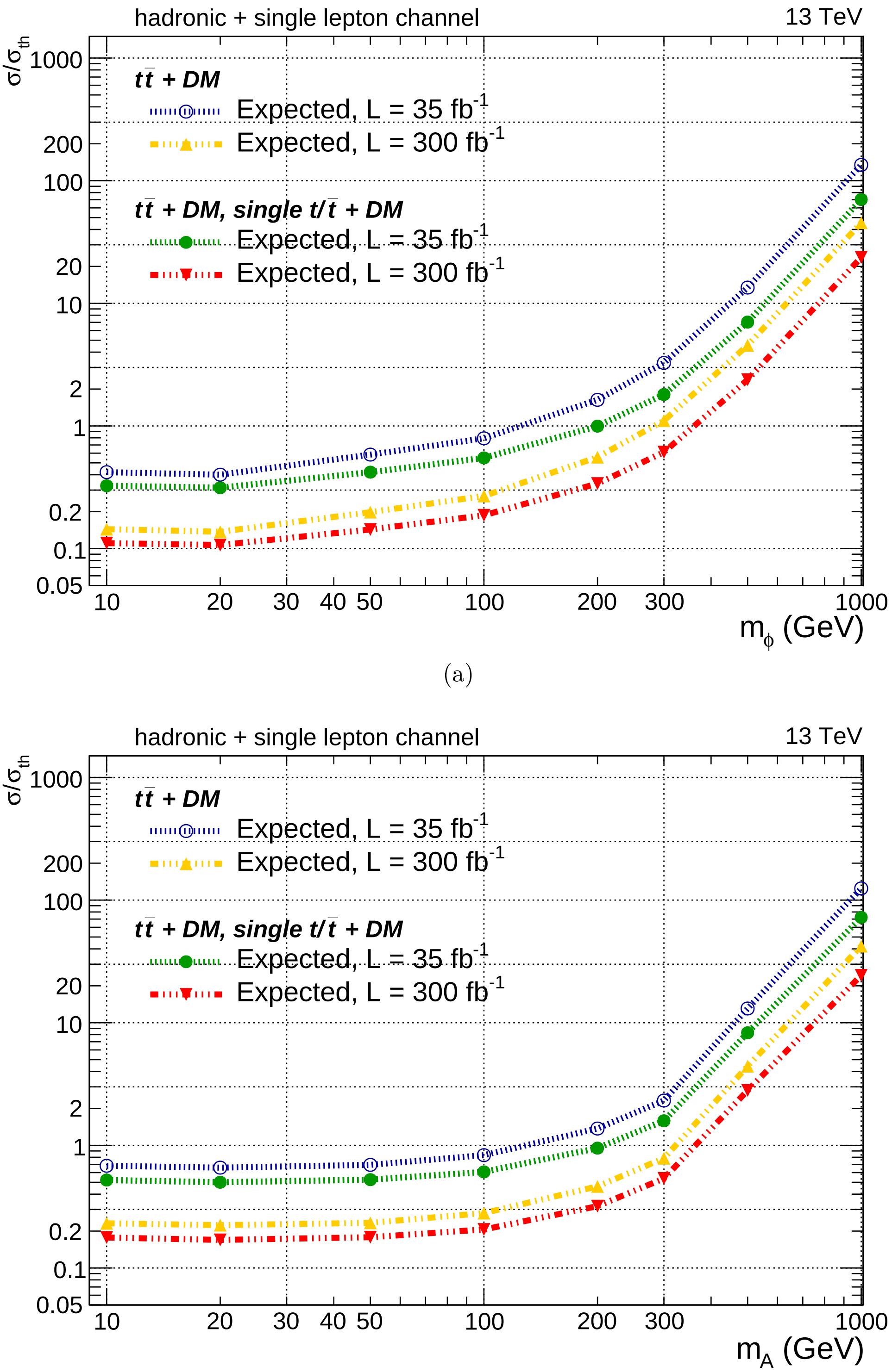

(a)

(b)

Figure 7.11: Expected and observed limits comparison between the tt+DM considered alone (blue and yellow lines) or together with the $t/\bar{t}$+DM process (green and red lines). The limits are presented for the scalar (a) and pseudoscalar (b) mediator hypothesis considering two integrated luminosity scenarios, namely 35fb^{-1} and 300fb^{-1}. The region above the limit lines, indicated by the shaded areas, represents the excluded parameter space.

	$M_\chi,\ M_\varphi$ (GeV)	tt+DM (pb)	$t/\bar{t}$+DM (pb)			
			t-channel	tW-channel	s-channel	total t+DM
scalar	$m_\chi = 1,\ m_\Phi = 10$	19.76 ± 0.01	$(27.18 \pm 0.05) \cdot 10^{-1}$	$(73.25 \pm 0.06) \cdot 10^{-2}$	$(7.03 \pm 0.01) \cdot 10^{-2}$	$(35.20 \pm 0.05) \cdot 10^{-1}$
	$m_\chi = 1,\ m_\Phi = 20$	(10.55 ± 0.01)	$(17.03 \pm 0.03) \cdot 10^{-1}$	$(40.44 \pm 0.03) \cdot 10^{-2}$	$(36.29 \pm 0.06) \cdot 10^{-3}$	$(21.43 \pm 0.03) \cdot 10^{-1}$
	$m_\chi = 1,\ m_\Phi = 50$	$(30.06 \pm 0.02) \cdot 10^{-1}$	$(7.00 \pm 0.01) \cdot 10^{-1}$	$(14.09 \pm 0.01) \cdot 10^{-2}$	$(10.10 \pm 0.02) \cdot 10^{-3}$	$(8.51 \pm 0.01) \cdot 10^{-1}$
	$m_\chi = 1,\ m_\Phi = 100$	$(69.60 \pm 0.04) \cdot 10^{-2}$	$(26.83 \pm 0.04) \cdot 10^{-2}$	$(55.49 \pm 0.04) \cdot 10^{-3}$	$(24.74 \pm 0.03) \cdot 10^{-4}$	$(32.62 \pm 0.04) \cdot 10^{-2}$
	$m_\chi = 1,\ m_\Phi = 200$	$(99.16 \pm 0.07) \cdot 10^{-3}$	$(7.37 \pm 0.01) \cdot 10^{-2}$	$(22.15 \pm 0.02) \cdot 10^{-3}$	$(37.6 \pm 0.05) \cdot 10^{-5}$	$(9.62 \pm 0.01) \cdot 10^{-2}$
	$m_\chi = 1,\ m_\Phi = 300$	$(32.21 \pm 0.02) \cdot 10^{-3}$	$(28.88 \pm 0.05) \cdot 10^{-3}$	$(12.04 \pm 0.01) \cdot 10^{-3}$	$(9.87 \pm 0.02) \cdot 10^{-5}$	$(41.02 \pm 0.005) \cdot 10^{-3}$
	$m_\chi = 1,\ m_\Phi = 500$	$(59.00 \pm 0.06) \cdot 10^{-4}$	$(43.85 \pm 0.08) \cdot 10^{-4}$	$(27.61 \pm 0.02) \cdot 10^{-4}$	$(9.01 \pm 0.01) \cdot 10^{-6}$	$(71.55 \pm 0.08) \cdot 10^{-4}$
	$m_\chi = 1,\ m_\Phi = 1000$	$(46.03 \pm 0.05) \cdot 10^{-5}$	$(24.99 \pm 0.03) \cdot 10^{-5}$	$(23.46 \pm 0.02) \cdot 10^{-5}$	$(27.64 \pm 0.04) \cdot 10^{-8}$	$(48.48 \pm 0.04) \cdot 10^{-5}$
	$m_\chi = 10,\ m_\Phi = 10$	$(96.42 \pm 0.07) \cdot 10^{-3}$	$(23.13 \pm 0.04) \cdot 10^{-3}$	$(50.44 \pm 0.04) \cdot 10^{-4}$	$(32.83 \pm 0.07) \cdot 10^{-5}$	$(28.51 \pm 0.04) \cdot 10^{-3}$
	$m_\chi = 50,\ m_\Phi = 300$	$(31.86 \pm 0.03) \cdot 10^{-3}$	$(28.73 \pm 0.04) \cdot 10^{-3}$	$(120.34 \pm 0.09) \cdot 10-4$	$(9.74 \pm 0.02) \cdot 10^{-5}$	$(40.86 \pm 0.04) \cdot 10^{-3}$
pseudoscalar	$m_\chi = 1,\ m_A = 10$	$(44.63 \pm 0.03) \cdot 10^{-2}$	$(15.34 \pm 0.02) \cdot 10^{-2}$	$(66.36 \pm 0.04) \cdot 10^{-3}$	$(19.69 \pm 0.04) \cdot 10^{-4}$	$(22.19 \pm 0.02) \cdot 10^{-2}$
	$m_\chi = 1,\ m_A = 20$	$(40.80 \pm 0.03) \cdot 10^{-2}$	$(14.19 \pm 0.02) \cdot 10^{-2}$	$(61.82 \pm 0.04) \cdot 10^{-3}$	$(16.78 \pm 0.03) \cdot 10^{-4}$	$(20.53 \pm 0.02) \cdot 10^{-2}$
	$m_\chi = 1,\ m_A = 50$	$(30.72 \pm 0.03) \cdot 10^{-2}$	$(10.94 \pm 0.02) \cdot 10^{-2}$	$(50.00 \pm 0.04) \cdot 10^{-3}$	$(10.30 \pm 0.02) \cdot 10^{-4}$	$(16.04 \pm 0.02) \cdot 10^{-2}$
	$m_\chi = 1,\ m_A = 100$	$(19.41 \pm 0.02) \cdot 10^{-2}$	$(7.04 \pm 0.01) \cdot 10^{-2}$	$(35.79 \pm 0.03) \cdot 10^{-3}$	$(47.79 \pm 0.09) \cdot 10^{-5}$	$(10.66 \pm 0.01) \cdot 10^{-2}$
	$m_\chi = 1,\ m_A = 200$	$(86.78 \pm 0.08) \cdot 10^{-3}$	$(31.39 \pm 0.05) \cdot 10^{-3}$	$(19.65 \pm 0.02) \cdot 10^{-3}$	$(13.20 \pm 0.02) \cdot 10^{-5}$	$(51.17 \pm 0.05) \cdot 10^{-3}$
	$m_\chi = 1,\ m_A = 300$	$(42.50 \pm 0.04) \cdot 10^{-3}$	$(15.55 \pm 0.02) \cdot 10^{-3}$	$(11.33 \pm 0.01) \cdot 10^{-3}$	$(46.28 \pm 0.08) \cdot 10^{-6}$	$(26.92 \pm 0.03) \cdot 10^{-3}$
	$m_\chi = 1,\ m_A = 500$	$(59.43 \pm 0.06) \cdot 10^{-4}$	$(22.27 \pm 0.04) \cdot 10^{-4}$	$(19.96 \pm 0.02) \cdot 10^{-4}$	$(41.72 \pm 0.07) \cdot 10^{-7}$	$(42.27 \pm 0.05) \cdot 10^{-4}$
	$m_\chi = 1,\ m_A = 1000$	$(48.33 \pm 0.05) \cdot 10^{-5}$	$(19.09 \pm 0.03) \cdot 10^{-5}$	$(21.44 \pm 0.02) \cdot 10^{-5}$	$(19.31 \pm 0.03) \cdot 10^{-8}$	$(40.56 \pm 0.03) \cdot 10^{-5}$
	$m_\chi = 10,\ m_A = 10$	$(15.28 \pm 0.02) \cdot 10^{-3}$	$(5.45 \pm 0.01) \cdot 10^{-3}$	$(26.74 \pm 0.02) \cdot 10^{-4}$	$(47.17 \pm 0.09) \cdot 10^{-6}$	$(8.17 \pm 0.01) \cdot 10^{-3}$
	$m_\chi = 50,\ m_A = 300$	$(42.43 \pm 0.04) \cdot 10^{-3}$	$(15.54 \pm 0.03) \cdot 10^{-3}$	$(11.34 \pm 0.01) \cdot 10^{-3}$	$(46.19 \pm 0.08) \cdot 10^{-6}$	$(26.93 \pm 0.03) \cdot 10^{-3}$

Table 7.1: Cross sections of the $t/\bar{t}$+DM and tt+DM samples for different mediator and DM masses and for the scalar and pseudoscalar hypotheses. For the $t/\bar{t}$+DM processes the cross sections are specified for the inclusive production as well as for each production mode (t-, s-, and tW-channels).

$M_\chi,\ M_\varphi$ (GeV)	hadronic		single lepton	
	CMS	DELPHES	CMS	DELPHES
$M_\chi = 1,\ M_\phi = 10$	20 ± 12	23.9 ± 2.3	9.1 ± 4.3	8.8 ± 1.8
$M_\chi = 1,\ M_\phi = 100$	10.0 ± 3.0	10.1 ± 0.42	4.64 ± 0.56	4.78 ± 0.38
$M_\chi = 1,\ M_A = 100$	8.5 ± 1.4	8.03 ± 0.13	4.36 ± 0.29	4.61 ± 0.13

Table 7.2: Comparison of the tt+DM yields obtained by the 13 TeV analysis (Section 6.4.2) and with the private simulation after the single lepton and hadronic SR selections. The numbers refer to the integrated luminosity collected by CMS in 2015 of 2.2 fb^{-1}. The uncertainty reported is statistical only.

	$M_\chi,\ M_\varphi$ (GeV)	tt+DM		$t/\bar{t}$+DM	
		hadronic	single lepton	hadronic	single lepton
scalar	$M_\chi = 1,\ M_\Phi = 10$	23.9 ± 2.3	8.8 ± 1.8	5.43 ± 0.45	2.59 ± 0.33
	$M_\chi = 1,\ M_\Phi = 20$	22.5 ± 1.6	9.3 ± 1.4	5.91 ± 0.48	2.51 ± 0.33
	$M_\chi = 1,\ M_\Phi = 50$	15.96 ± 0.90	6.28 ± 0.73	5.64 ± 0.23	2.48 ± 0.17
	$M_\chi = 1,\ M_\Phi = 100$	10.08 ± 0.42	4.78 ± 0.38	4.53 ± 0.17	2.05 ± 0.12
	$M_\chi = 1,\ M_\Phi = 200$	$4.34 \pm 0.07)$	2.72 ± 0.07	2.78 ± 0.07	1.49 ± 0.05
	$M_\chi = 1,\ M_\Phi = 300$	$2.14 \pm 0.03)$	1.17 ± 0.03	1.71 ± 0.03	0.95 ± 0.02
	$M_\chi = 1,\ M_\Phi = 500$	$(4.62 \pm 0.05) \cdot 10^{-1}$	$(2.86 \pm 0.06) \cdot 10^{-1}$	$(3.99 \pm 0.05) \cdot 10^{-1}$	$(2.60 \pm 0.05) \cdot 10^{-1}$
	$M_\chi = 1,\ M_\Phi = 1000$	$(4.58 \pm 0.05) \cdot 10^{-2}$	$(2.87 \pm 0.05) \cdot 10^{-2}$	$(3.46 \pm 0.04) \cdot 10^{-2}$	$(2.63 \pm 0.04) \cdot 10^{-2}$
	$M_\chi = 10,\ M_\Phi = 10$	0.61 ± 0.03	0.28 ± 0.02	$(2.56 \pm 0.09) \cdot 10^{-1}$	$(2.84 \pm 0.23) \cdot 10^{-1}$
	$M_\chi = 50,\ M_\Phi = 300$	2.21 ± 0.03	1.16 ± 0.03	1.74 ± 0.07	0.87 ± 0.04
pseudoscalar	$M_\chi = 1,\ M_A = 10$	10.65 ± 0.23	5.56 ± 0.22	3.09 ± 0.05	1.71 ± 0.05
	$M_\chi = 1,\ M_A = 20$	10.66 ± 0.22	5.79 ± 0.21	3.70 ± 0.11	1.81 ± 0.08
	$M_\chi = 1,\ M_A = 50$	9.72 ± 0.18	5.53 ± 0.18	3.42 ± 0.08	1.71 ± 0.06
	$M_\chi = 1,\ M_A = 100$	8.03 ± 0.13	4.61 ± 0.13	2.92 ± 0.06	1.67 ± 0.05
	$M_\chi = 1,\ M_A = 200$	4.74 ± 0.07	2.79 ± 0.07	2.07 ± 0.04	1.26 ± 0.03
	$M_\chi = 1,\ M_A = 300$	2.72 ± 0.04	1.66 ± 0.04	1.31 ± 0.02	0.76 ± 0.01
	$M_\chi = 1,\ M_A = 500$	$(4.65 \pm 0.06) \cdot 10^{-1}$	$(2.94 \pm 0.06) \cdot 10^{-1}$	$(2.48 \pm 0.03) \cdot 10^{-1}$	$(1.71 \pm 0.03) \cdot 10^{-1}$
	$M_\chi = 1,\ M_A = 1000$	$(4.73 \pm 0.05) \cdot 10^{-2}$	$(3.09 \pm 0.05) \cdot 10^{-2}$	$(3.03 \pm 0.03) \cdot 10^{-2}$	$(2.27 \pm 0.03) \cdot 10^{-2}$
	$M_\chi = 10,\ M_A = 10$	0.54 ± 0.01	0.31 ± 0.01	$(2.05 \pm 0.06) \cdot 10^{-1}$	$(1.11 \pm 0.05) \cdot 10^{-1}$
	$M_\chi = 50,\ M_A = 300$	2.78 ± 0.04	1.68 ± 0.037	1.25 ± 0.04	0.79 ± 0.03

Table 7.3: Expected signal events for scalar and pseudoscalar mediators for different $M_\chi,\ M_\varphi$ mass hypotheses obtained with the private simulation. The numerical values are referred to an integrated luminosity of 2.2 fb^{-1}, and are separated by process (tt+DM or the sum of $t/\bar{t}$+DM production channels) and final state (hadronic or single lepton).

	$M_\chi,\ M_\varphi$ (GeV)	tt +DM		tt, $t/\bar{t}$+DM	
		expected	observed	expected	observed
scalar	$M_\chi = 1,\ M_\Phi = 10$	1.7	2.1	1.3	1.7
	$M_\chi = 1,\ M_\Phi = 20$	1.6	2.1	1.3	1.6
	$M_\chi = 1,\ M_\Phi = 50$	2.4	3.0	1.7	2.1
	$M_\chi = 1,\ M_\Phi = 100$	3.2	4.1	2.2	2.9
	$M_\chi = 1,\ M_\Phi = 200$	6.7	8.6	4.1	5.3
	$M_\chi = 1,\ M_\Phi = 300$	13	17	7.4	9.5
	$M_\chi = 1,\ M_\Phi = 500$	56	72	29	38
	$M_\chi = 1,\ M_\Phi = 1000$	554	716	291	377
	$M_\chi = 10,\ M_\Phi = 10$	54	69	37	48
	$M_\chi = 50,\ M_\Phi = 300$	13	17	7.7	9.8
pseudoscalar	$M_\chi = 1,\ M_A = 10$	2.8	3.6	2.1	2.8
	$M_\chi = 1,\ M_A = 20$	2.7	3.5	2.1	2.6
	$M_\chi = 1,\ M_A = 50$	2.9	3.7	2.2	2.8
	$M_\chi = 1,\ M_A = 100$	3.4	4.4	2.5	3.2
	$M_\chi = 1,\ M_A = 200$	5.7	7.3	3.9	5.0
	$M_\chi = 1,\ M_A = 300$	9.6	12	6.5	8.5
	$M_\chi = 1,\ M_A = 500$	54	70	34	44
	$M_\chi = 1,\ M_A = 1000$	518	668	299	387
	$M_\chi = 10,\ M_A = 10$	50	65	37	48
	$M_\chi = 50,\ M_A = 300$	9.4	12	6.4	8.3

Table 7.4: Observed and expected exclusion limits on μ_s at 95% CL, relative to the integrated luminosity collected by CMS in 2015 ($L = 2.2$ fb^{-1}) for the combination of the single lepton and hadronic channels. The central column reports the excluded values for a tt +DM signal alone, and the left column for both the tt +DM and $t/\bar{t}$ +DM signal combined.

Chapter 8

Conclusions

Measurements leading to proof of the existence of dark matter (DM) are provided by cosmology and astrophysics. These experimental results are based on the sole gravitational interaction but provide constraints on the DM particle characteristics. Nevertheless, no information about the nature of DM is yet available. The standard model (SM) of particle physics does not include a description of this matter component within its framework, requiring therefore new physics theories to overcome this limitation.

An important opportunity to study DM non-gravitational interactions is provided by high energy proton-proton collisions at the LHC. Under the assumption that the DM interacts weakly with the SM sector, DM particles can be produced in such collisions. The challenging signature of DM at colliders is a missing momentum balanced by a visible SM particle. In this thesis, a search for the associated production of DM with a top quark pair has been presented. This type of processes is ideal to investigate interactions between DM and SM particles mediated by a spin-0 particle. In fact, assuming minimal flavor violation, the couplings of the interaction are of the Yukawa type, i.e. proportional to the mass of the quark that the DM couples to. As a consequence, scalar and pseudoscalar interactions are suppressed if quarks lighter than the top are considered in the production process.

In this thesis, the analysis targeting events where DM particles are produced in association with a top quark pair is performed using the data recorded by the CMS detector at two different center-of-mass energies of 8 and 13 TeV. The datasets correspond to integrated luminosities of 19.7 fb^{-1} and 2.2 fb^{-1}, respectively. The first analysis investigate final states where one top quark decays leptonically and the other hadronically. The analysis is performed in a similar way using the data collected in 2015 at a center-of-mass energy of 13 TeV. In this case, the analysis targets in addition events where both top quarks decay hadronically.

The analysis strategy is to define a signal region where DM events are enhanced with respect to the SM background. The selection identifying such region is based on simulation and exploit kinematic differences between DM signal and background events. The remaining major background contributions come from $t\bar{t}$ and V+jets events. These backgrounds are compared with the collected data in dedicated control regions in order to improve their description. For the 8 TeV analysis, data-to-simulation scaling factors are extracted from these regions and extrapolated to the region where DM events are excepted. In the 13 TeV analysis, the missing transverse energy distributions in the control and signal regions are fitted simultaneously in the signal extraction procedure. This technique is shown to improve the background estimation and to account for possible signal contamination in the control regions.

After the background estimation, the results of the 13 TeV analysis are extracted using a binned maximum likelihood fit, while for the 8 TeV analysis are extracted from the comparison of the observed and expected number of events in signal region. No excess of events above SM expectation is found in both data-sets and upper limits on the signal cross section are set.

In the 8 TeV analysis, the results are interpreted in terms of an effective field theory approach. The impact of the validity of the contact interaction assumption is included in the obtained results. Cross sections larger than 20 to 55 fb are excluded at 90% CL for DM mass hypotheses from 1 GeV to 1 TeV. The interaction scale of the corresponding effective field theory is excluded below 118 GeV for a DM mass of 100 GeV at 90% CL. The results are then translated to exclusion limits on the DM-nucleon scattering cross section and compared with direct detection experiments. Under the hypothesis that only the scalar interaction is responsible for the DM-nucleon scattering, more stringent limits are obtained in the DM mass region below 6 GeV from the presented CMS result.

A simplified model, which explicitly considers the mediator of the interaction, is used for the interpretation of the 13 TeV analysis results. Constraints are set on the production cross section as a function of the DM and mediator masses. No exclusion of mediator masses for unitary coupling is yet achieved from the combination of the hadronic and single lepton channel with the considered dataset.

The simplified model used to describe DM events in the 13 TeV analysis also predicts processes in which the DM particles are produced in association with a single top quark. The presented results, show the important contribution of these new processes for DM searches under the hypothesis of scalar or pseudoscalar interactions. Even higher improvements are foreseen for the associated production of DM with a single top developing an optimized selection targeting these processes.

Bibliography

[1] F. Zwicky, “Die Rotverschiebung von extragalaktischen Nebeln”, *Helvetica Physica Acta* **6** (1933) 110–127.

[2] V. C. Rubin and W. K. Ford, Jr., “Rotation of the Andromeda Nebula from a Spectroscopic Survey of Emission Regions”, *The Astrophysical Journal* **159** (1970) 379, `"http://dx.doi.org/10.1086/150317"`.

[3] D. e. a. Clowe, “A direct empirical proof of the existence of dark matter”, *Astrophys. J.* **648** (2006) L109–L113, `arXiv:astro-ph/0608407`.

[4] **Planck** Collaboration, P. A. R. Ade *et al.*, “Planck 2015 results. XIII. Cosmological parameters”, *Astron. Astrophys.* **594** (2016) A13, `arXiv:1502.01589`.

[5] S. L. Glashow, “Partial Symmetries of Weak Interactions”, *Nucl. Phys.* **22** (1961) 579–588.

[6] A. Salam and J. C. Ward, “Electromagnetic and weak interactions”, *Phys. Lett.* **13** (1964) 168–171.

[7] S. Weinberg, “A Model of Leptons”, *Phys. Rev. Lett.* **19** (1967) 1264–1266.

[8] S. Weinberg, “Effects of a neutral intermediate boson in semileptonic processes”, *Phys. Rev.* **D5** (1972) 1412–1417.

[9] L. Evans and P. Bryant, “LHC Machine”, *JINST* **3** (2008) S08001.

[10] **CMS** Collaboration, “The CMS experiment at the CERN LHC”, *JINST* **3** (2008) S08004, `http://dx.doi.org/10.1088/1748-0221/3/08/S08004`.

[11] **CMS** Collaboration, “Search for the production of dark matter in association with top-quark pairs in the single-lepton final state in proton-proton collisions at sqrt(s) = 8 TeV”, *JHEP* **06** (2015) 121, `arXiv:1504.03198`.

[12] **CMS** Collaboration, “Search for dark matter in association with a top quark pair at sqrt(s)=13 TeV”, Tech. Rep. CMS-PAS-EXO-16-005, CERN, Geneva, 2016. `"https://cds.cern.ch/record/2204933"`.

[13] F. Halzen and A. Martin, “Quarks and Leptons”, John Wiley & Sons, 1984.

[14] K. G. Begeman, A. H. Broeils, and R. H. Sanders, “Extended rotation curves of spiral galaxies: Dark haloes and modified dynamics”, *Mon. Not. Roy. Astron. Soc.* **249** (1991) 523.

[15] K. Freese, “Review of Observational Evidence for Dark Matter in the Universe and in upcoming searches for Dark Stars”, *EAS Publ. Ser.* **36** (2009) 113–126, `arXiv:0812.4005`.

[16] **SDSS** Collaboration, J. K. Adelman-McCarthy *et al.*, “The Fourth Data Release of the Sloan Digital Sky Survey”, *Astrophys. J. Suppl.* **162** (2006) 38–48, `arXiv:astro-ph/0507711`.

[17] NASA, “1e 0657-56: Nasa finds direct proof of dark matter”. `http://chandra.harvard.edu/photo/2006/1e0657/index.html`.

[18] W. Hu, N. Sugiyama, and J. Silk, “The Physics of microwave background anisotropies”, *Nature* **386** (1997) 37–43, `arXiv:astro-ph/9604166`.

[19] W. Hu and S. Dodelson, “Cosmic microwave background anisotropies”, *Ann. Rev. Astron. Astrophys.* **40** (2002) 171–216, `arXiv:astro-ph/0110414`.

[20] S. Seager, D. D. Sasselov, and D. Scott, “How exactly did the universe become neutral?”, *Astrophys. J. Suppl.* **128** (2000) 407–430, `arXiv:astro-ph/9912182`.

[21] ESA, “Cosmic microwave brackground seen by planck”. `http://sci.esa.int/jump.cfm?oid=51553`.

[22] K. Garrett and G. Duda, “Dark Matter: A Primer”, *Adv. Astron.* **2011** (2011) 968283, `arXiv:1006.2483`.

[23] ESA, “Planck’s power spectrum of temperature fluctuations in the cosmic microwave background”. `http://sci.esa.int/jump.cfm?oid=51555`.

[24] **Particle Data Group** Collaboration, C. Patrignani *et al.*, “Review of Particle Physics”, *Chin. Phys.* **C40** (2016), no. 10, 100001.

[25] N. Cabibbo, “Unitary Symmetry and Leptonic Decays”, *Phys. Rev. Lett.* **10** (1963) 531–533, [,648(1963)].

[26] M. Kobayashi and T. Maskawa, “CP Violation in the Renormalizable Theory of Weak Interaction”, *Prog. Theor. Phys.* **49** (1973) 652–657.

[27] P. W. Higgs, “Broken Symmetries and the Masses of Gauge Bosons”, *Phys. Rev. Lett.* **13** (1964) 508–509.

[28] F. Englert and R. Brout, “Broken Symmetry and the Mass of Gauge Vector Mesons”, *Phys. Rev. Lett.* **13** (1964) 321–323.

[29] T. W. B. Kibble, “Symmetry breaking in nonAbelian gauge theories”, *Phys. Rev.* **155** (1967) 1554–1561.

[30] **ATLAS** Collaboration, “Observation of a new particle in the search for the Standard Model Higgs boson with the ATLAS detector at the LHC”, *Phys. Lett.* **B716** (2012)a 1–29, `arXiv:1207.7214`.

[31] **CMS** Collaboration, “Observation of a new boson at a mass of 125 GeV with the CMS experiment at the LHC”, *Phys. Lett.* **B716** (2012)b 30–61, `arXiv:1207.7235`.

[32] G. Altarelli, “The Standard electroweak theory and beyond”, in “Phenomenology of gauge interactions. Proceedings, Summer School, Zuoz, Switzerland, August 13-19, 2000”, pp. 1–59. 2000. `arXiv:hep-ph/0011078`.

[33] G. F. Giudice, “Naturalness after LHC8”, *PoS* **EPS-HEP2013** (2013) 163, `arXiv:1307.7879`.

[34] P. J. E. Peebles, “The origin of galaxies and clusters of galaxies”, *Science* **224** (1984) 1385–1391, `"http://adsabs.harvard.edu/abs/1984Sci...224.1385P"`.

[35] G. Bertone, D. Hooper, and J. Silk, “Particle dark matter: Evidence, candidates and constraints”, *Phys. Rept.* **405** (2005) 279–390, `arXiv:hep-ph/0404175`.

[36] D. Hooper, “Particle Dark Matter”, in “Proceedings of Theoretical Advanced Study Institute in Elementary Particle Physics on The dawn of the LHC era (TASI 2008): Boulder, USA, June 2-27, 2008”, pp. 709–764. 2010. `arXiv:0901.4090`. `"http://lss.fnal.gov/cgi-bin/find_paper.pl?conf-09-025"`,

[37] S. P. Martin, “A Supersymmetry primer”, `arXiv:hep-ph/9709356`, [Adv. Ser. Direct. High Energy Phys.18,1(1998)].

[38] F. Arneodo, “Dark Matter Searches”, in “Proceedings, 32nd International Symposium on Physics in Collision (PIC 2012): Strbske Pleso, Slovakia, September 12-15, 2012”, pp. 275–286. 2013. `arXiv:1301.0441`. `"https://inspirehep.net/record/1209245/files/arXiv:1301.0441.pdf"`,

[39] J. L. Feng, “Dark Matter Candidates from Particle Physics and Methods of Detection”, *Ann. Rev. Astron. Astrophys.* **48** (2010) 495–545, `arXiv:1003.0904`.

[40] G. Bertone, “Particle Dark Matter”, Cambridge University Press, 2010.

[41] S. Lowette, “Accelerator searches for new physics in the context of dark matter”, *J. Phys. Conf. Ser.* **718** (2016), no. 2, 022011.

[42] **SuperCDMS** Collaboration, R. Agnese *et al.*, “New Results from the Search for Low-Mass Weakly Interacting Massive Particles with the CDMS Low Ionization Threshold Experiment”, *Phys. Rev. Lett.* **116** (2016), no. 7, 071301, `arXiv:1509.02448`.

[43] **CoGeNT** Collaboration, C. E. Aalseth *et al.*, “CoGeNT: A Search for Low-Mass Dark Matter using p-type Point Contact Germanium Detectors”, *Phys. Rev.* **D88** (2013) 012002, `arXiv:1208.5737`.

[44] **CRESST** Collaboration, G. Angloher *et al.*, “Results on light dark matter particles with a low-threshold CRESST-II detector”, *Eur. Phys. J.* **C76** (2016), no. 1, 25, `arXiv:1509.01515`.

[45] D. S. Akerib *et al.*, “Results from a search for dark matter in the complete LUX exposure”, `arXiv:1608.07648`.

[46] **XENON100** Collaboration, E. Aprile *et al.*, “XENON100 Dark Matter Results from a Combination of 477 Live Days”, `arXiv:1609.06154`.

[47] **COUPP** Collaboration, E. Behnke *et al.*, “Direct Measurement of the Bubble Nucleation Energy Threshold in a CF3I Bubble Chamber”, *Phys. Rev.* **D88** (2013) 021101, `arXiv:1304.6001`.

[48] **IceCube** Collaboration, M. G. Aartsen *et al.*, "Constraints on ultra-high-energy cosmic ray sources from a search for neutrinos above 10 PeV with IceCube", `arXiv:1607.05886`.

[49] **PICASSO** Collaboration, S. Archambault *et al.*, "Constraints on Low-Mass WIMP Interactions on ^{19}F from PICASSO", *Phys. Lett.* **B711** (2012) 153–161, `arXiv:1202.1240`.

[50] **The SIMPLE Collaboration** Collaboration, "Final Analysis and Results of the Phase II SIMPLE Dark Matter Search", *Phys. Rev. Lett.* **108** (2012) 201302, `arXiv:1106.3014`.

[51] **Super-Kamiokande** Collaboration, T. Tanaka *et al.*, "An Indirect Search for WIMPs in the Sun using 3109.6 days of upward-going muons in Super-Kamiokande", *Astrophys. J.* **742** (2011) 78, `arXiv:1108.3384`.

[52] NASA, "Uncovering a gamma-ray excess at the galactic center". `http://svs.gsfc.nasa.gov/vis/a010000/a011500/a011513/heatmap_no_labels_large.jpg`.

[53] **Fermi-LAT** Collaboration, M. Ackermann *et al.*, "Dark matter constraints from observations of 25 Milky Way satellite galaxies with the Fermi Large Area Telescope", *Phys. Rev.* **D89** (2014) 042001, `arXiv:1310.0828`.

[54] T. Daylan, D. P. Finkbeiner, D. Hooper, T. Linden, S. K. N. Portillo, N. L. Rodd, and T. R. Slatyer, "The characterization of the gamma-ray signal from the central Milky Way: A case for annihilating dark matter", *Phys. Dark Univ.* **12** (2016) 1–23, `arXiv:1402.6703`.

[55] **Fermi-LAT** Collaboration, M. Ackermann *et al.*, "Measurement of separate cosmic-ray electron and positron spectra with the Fermi Large Area Telescope", *Phys. Rev. Lett.* **108** (2012) 011103, `arXiv:1109.0521`.

[56] **PAMELA** Collaboration, O. Adriani *et al.*, "An anomalous positron abundance in cosmic rays with energies 1.5-100 GeV", *Nature* **458** (2009) 607–609, `arXiv:0810.4995`.

[57] **AMS** Collaboration, M. Aguilar *et al.*, "Electron and Positron Fluxes in Primary Cosmic Rays Measured with the Alpha Magnetic Spectrometer on the International Space Station", *Phys. Rev. Lett.* **113** (2014) 121102.

[58] J. Goodman, M. Ibe, A. Rajaraman, W. Shepherd, T. M. P. Tait, and H.-B. Yu, "Constraints on Dark Matter from Colliders", *Phys. Rev.* **D82** (2010) 116010, `arXiv:1008.1783`.

[59] J. Goodman, M. Ibe, A. Rajaraman, W. Shepherd, T. M. P. Tait, and H.-B. Yu, "Constraints on Light Majorana dark Matter from Colliders", *Phys. Lett.* **B695** (2011) 185–188, `arXiv:1005.1286`.

[60] D. Abercrombie *et al.*, "Dark Matter Benchmark Models for Early LHC Run-2 Searches: Report of the ATLAS/CMS Dark Matter Forum", `arXiv:1507.00966`.

[61] **ATLAS** Collaboration, "The atlas experiment at the cern large hadron collider", *Journal of Instrumentation* **3** (2008), no. 08, S08003, `http://stacks.iop.org/1748-0221/3/i=08/a=S08003`.

[62] **ATLAS** Collaboration, M. Aaboud *et al.*, "Search for new phenomena in final states with an energetic jet and large missing transverse momentum in pp collisions at $\sqrt{s} = 13$ TeV using the ATLAS detector", *Phys. Rev.* **D94** (2016), no. 3, 032005, `arXiv:1604.07773`.

[63] **CMS** Collaboration, “Search for dark matter, extra dimensions, and unparticles in monojet events in proton–proton collisions at $\sqrt{s} = 8$ TeV”, *Eur. Phys. J.* **C75** (2015)a, no. 5, 235, `arXiv:1408.3583`.

[64] **ATLAS** Collaboration, “Search for new phenomena in final states with an energetic jet and large missing transverse momentum in pp collisions at $\sqrt{s}$ =8 TeV with the ATLAS detector”, *Eur. Phys. J.* **C75** (2015)b, no. 7, 299, `arXiv:1502.01518`, [Erratum: Eur. Phys. J.C75,no.9,408(2015)].

[65] **ATLAS** Collaboration, “Search for dark matter candidates and large extra dimensions in events with a jet and missing transverse momentum with the ATLAS detector”, 2012.

[66] **ATLAS** Collaboration, “Search for new phenomena with the monojet and missing transverse momentum signature using the ATLAS detector in $\sqrt{s} = 7$ TeV proton-proton collisions”, *Phys. Lett.* **B705** (2011) 294–312, `arXiv:1106.5327`.

[67] **CMS** Collaboration, S. Chatrchyan *et al.*, “Search for dark matter and large extra dimensions in monojet events in *pp* collisions at $\sqrt{s} = 7$ TeV”, *JHEP* **09** (2012) 094, `arXiv:1206.5663`.

[68] **CMS** Collaboration, “Search for dark matter particles in proton-proton collisions at $\sqrt{s} = 8$ TeV using the razor variables”, *JHEP* **12** (2016) 088, `arXiv:1603.08914`.

[69] **CMS** Collaboration, “Search for physics beyond the standard model in final states with a lepton and missing transverse energy in proton-proton collisions at $\sqrt{(s)} = 8$ TeV”, *Phys. Rev.* **D91** (2015), no. 9, 092005, `arXiv:1408.2745`.

[70] **ATLAS** Collaboration, “Search for dark matter in events with a Z boson and missing transverse momentum in pp collisions at $\sqrt{s}$=8 TeV with the ATLAS detector”, *Phys. Rev.* **D90** (2014)a, no. 1, 012004, `arXiv:1404.0051`.

[71] **ATLAS** Collaboration, “Search for dark matter in events with a hadronically decaying W or Z boson and missing transverse momentum in *pp* collisions at $\sqrt{s} = 8$ TeV with the ATLAS detector”, *Phys. Rev. Lett.* **112** (2014)b, no. 4, 041802, `arXiv:1309.4017`.

[72] **ATLAS** Collaboration, “Search for new particles in events with one lepton and missing transverse momentum in *pp* collisions at $\sqrt{s} = 8$ TeV with the ATLAS detector”, *JHEP* **09** (2014)c 037, `arXiv:1407.7494`.

[73] **CMS** Collaboration, “Search for dark matter in proton-proton collisions at 8 TeV with missing transverse momentum and vector boson tagged jets”, *JHEP* **12** (2016) 083, `arXiv:1607.05764`.

[74] **CMS** Collaboration, “Search for Dark Matter produced in association with bottom quarks”, Tech. Rep. CMS-PAS-B2G-15-007, CERN, Geneva, 2016a.

[75] **ATLAS** Collaboration, “Search for Dark Matter production associated with bottom quarks with 13.3 fb^{-1} of pp collisions at $\sqrt{(s)} = 13$ TeV with the ATLAS detector at the LHC”, Tech. Rep. ATLAS-CONF-2016-086, CERN, Geneva, Aug 2016b.

[76] **ATLAS** Collaboration, “Search for dark matter in events with heavy quarks and missing transverse momentum in *pp* collisions with the ATLAS detector”, *Eur. Phys. J.* **C75** (2015), no. 2, 92, `arXiv:1410.4031`.

[77] **Snowmass 2013 Cosmic Frontier Working Groups 1–4** Collaboration, D. Bauer *et al.*, "Dark Matter in the Coming Decade: Complementary Paths to Discovery and Beyond", *Phys. Dark Univ.* **7-8** (2015) 16–23, `arXiv:1305.1605`.

[78] **ALICE** Collaboration, "The ALICE experiment at the CERN LHC", *JINST* **3** (2008) S08002.

[79] **LHCb** Collaboration, "The LHCb Detector at the LHC", *JINST* **3** (2008) S08005.

[80] CERN, "Cern accelerator complex". `http://te-epc-lpc.web.cern.ch/te-epc-lpc/machines/pagesources/Cern-Accelerator-Complex.jpg`.

[81] **CMS** Collaboration, "Public cms data quality information". `https://twiki.cern.ch/twiki/bin/view/CMSPublic/DataQuality#2010_Proton_Proton_Collisions`.

[82] **CMS** Collaboration, "2015 proton-proton 13 tev collisions: Luminosity versus day". a. `http://cms-service-lumi.web.cern.ch/cms-service-lumi/publicplots/int_lumi_per_day_cumulative_pp_2015.pdf`.

[83] **CMS** Collaboration, "2012 proton-proton collisions: Luminosity versus day". b. `http://cms-service-lumi.web.cern.ch/cms-service-lumi/publicplots/int_lumi_per_day_cumulative_pp_2012.png`.

[84] **CMS** Collaboration, T. Dorigo, "Recent Results of the CMS Experiment", *EPJ Web Conf.* **70** (2014) 00021, `arXiv:1210.6809`.

[85] **CMS** Collaboration, O. Kodolova and M. Murray, "Heavy Ion Physics Program in CMS Experiment", *Nucl. Phys.* **A830** (2009) 97C–104C, `arXiv:0907.4492`, `"10.1016/j.nuclphysa.2009.09.014"`.

[86] **CMS** Collaboration, "CMS Physics: Technical Design Report Volume 1: Detector Performance and Software", tech. rep., Geneva, 2006. `"https://cds.cern.ch/record/922757"`.

[87] **CMS** Collaboration, "CMS technical design report, volume II: Physics performance", *J. Phys.* **G34** (2007), no. 6, 995–1579.

[88] C. Grupen and B. Schwartz, "Particle detectors", Cambridge, UK: Cambridge Univ. Pr. (2008) 651 p, 2008.

[89] **CMS** Collaboration, "The CMS magnet project: Technical Design Report", CERN, Geneva, 1997.

[90] **CMS** Collaboration, "The CMS tracker system project: Technical Design Report", tech. rep., Geneva, 1997. `"https://cds.cern.ch/record/368412"`.

[91] **CMS** Collaboration, "The CMS tracker: addendum to the Technical Design Report", tech. rep., Geneva, 2000. `"https://cds.cern.ch/record/490194"`.

[92] M. Weber, "The CMS tracker", Tech. Rep. CMS-CR-2004-046, CERN, Geneva, Oct 2004. `https://cds.cern.ch/record/800402`.

[93] **CMS** Collaboration, "The CMS electromagnetic calorimeter project: Technical Design Report", tech. rep., Geneva, 1997. `https://cds.cern.ch/record/349375`.

[94] **CMS** Collaboration, “CMS Physics: Technical Design Report Volume 1: Detector Performance and Software”, CERN, Geneva, 2006.

[95] **CMS** Collaboration, “The CMS hadron calorimeter project: Technical Design Report”, tech. rep., Geneva, 1997. `"https://cds.cern.ch/record/357153"`.

[96] **CMS** Collaboration, “Performance of the CMS Hadron Calorimeter with Cosmic Ray Muons and LHC Beam Data”, *JINST* **5** (2010) T03012, `arXiv:0911.4991`, `http://dx.doi.org/10.1088/1748-0221/5/03/T03012`.

[97] **CMS** Collaboration, “The CMS muon project: Technical Design Report”, tech. rep., Geneva, 1997. `https://cds.cern.ch/record/343814`.

[98] **CMS** Collaboration, M. S. Kim, “CMS reconstruction improvement for the muon tracking by the RPC chambers”, *PoS* **RPC2012** (2012) 045, `arXiv:1209.2646`, JINST8,T03001 (2013).

[99] **CMS** Collaboration, “CMS TriDAS project: Technical Design Report, Volume 1: The Trigger Systems”, tech. rep. `"http://cds.cern.ch/record/706847"`.

[100] **CMS** Collaboration, “CMS The TriDAS Project: Technical Design Report, Volume 2: Data Acquisition and High-Level Trigger. CMS trigger and data-acquisition project”, tech. rep., Geneva, 2002. `"http://cds.cern.ch/record/578006"`.

[101] C. e. a. Eck, “LHC computing Grid: Technical Design Report”, tech. rep., Geneva, 2005.

[102] G. Altarelli and M. L. Mangano, eds., *1999 CERN Workshop on standard model physics (and more) at the LHC, CERN, Geneva, Switzerland, 25-26 May: Proceedings.* 2000. `"http://doc.cern.ch/cernrep/2000/2000-004/2000-004.html"`,

[103] T. Sjostrand, S. Mrenna, and P. Z. Skands, “PYTHIA 6.4 Physics and Manual”, *JHEP* **05** (2006) 026, `arXiv:hep-ph/0603175`, `"10.1088/1126-6708/2006/05/026"`.

[104] G. Sterman *et al.*, “Handbook of perturbative qcd”, *Rev. Mod. Phys.* **67** Jan (1995) 157–248, `"http://link.aps.org/doi/10.1103/RevModPhys.67.157"`.

[105] G. Altarelli and G. Parisi, “Asymptotic Freedom in Parton Language”, *Nucl. Phys.* **B126** (1977) 298–318.

[106] A. Buckley *et al.*, “General-purpose event generators for LHC physics”, *Phys. Rept.* **504** (2011) 145–233, `arXiv:1101.2599`.

[107] S. Agostinelli *et al.*, “Geant4—a simulation toolkit”, *Nuclear Instruments and Methods in Physics Research Section A: Accelerators, Spectrometers, Detectors and Associated Equipment* **506** (2003), no. 3, 250 – 303, `"http://www.sciencedirect.com/science/article/pii/S0168900203013688"`.

[108] A. Ribon, “Detector simulation”, 2012. `"https://indico.cern.ch/getFile.py/access?resId=0&materialId=slides&confId=190218"`.

[109] **CMS** Collaboration, “Particle-Flow Event Reconstruction in CMS and Performance for Jets, Taus, and MET”, Tech. Rep. CMS-PAS-PFT-09-001, CERN, 2009. Geneva, Apr 2009. `https://cds.cern.ch/record/1194487`.

[110] **CMS** Collaboration, “Description and performance of track and primary-vertex reconstruction with the CMS tracker”, *JINST* **9** (2014), no. 10, P10009, `arXiv:1405.6569`, `http://dx.doi.org/10.1088/1748-0221/9/10/P10009`.

[111] P. Billoir, “Progressive track recognition with a Kalman like fitting procedure”, *Comput. Phys. Commun.* **57** (1989) 390–394, `http://dx.doi.org/10.1016/0010-4655(89)90249-X`.

[112] R. Fruhwirth, “Application of Kalman filtering to track and vertex fitting”, *Nucl. Instrum. Meth.* **A262** (1987) 444–450, `http://dx.doi.org/10.1016/0168-9002(87)90887-4`.

[113] P. Billoir and S. Qian, “Simultaneous pattern recognition and track fitting by the Kalman filtering method”, *Nucl. Instrum. Meth.* **A294** (1990) 219–228, `http://dx.doi.org/10.1016/0168-9002(90)91835-Y`.

[114] K. Rose, “Deterministic annealing for clustering, compression, classification, regression, and related optimization problems”, in “Proceedings of the IEEE”, pp. 2210–2239. 1998.

[115] R. Frühwirth, W. Waltenberger, and P. Vanlaer, “Adaptive Vertex Fitting”, Tech. Rep. CMS-NOTE-2007-008, CERN, Geneva, Mar 2007. `https://cds.cern.ch/record/1027031`.

[116] **CMS** Collaboration, “Average pileup in 2012”. `http://cms-service-lumi.web.cern.ch/cms-service-lumi/publicplots/pileup_pp_2012.pdf`.

[117] M. Cacciari and G. P. Salam, “Pileup subtraction using jet areas”, *Phys. Lett.* **B659** (2008) 119–126, `arXiv:0707.1378`, `http://dx.doi.org/10.1016/j.physletb.2007.09.077`.

[118] **CMS** Collaboration, “Performance of CMS muon reconstruction in pp collision events at $\sqrt{s} = 7$ TeV”, *JINST* **7** (2012) P10002, `arXiv:1206.4071`, `http://dx.doi.org/10.1088/1748-0221/7/10/P10002`.

[119] **CMS** Collaboration, “Performance of CMS Muon Reconstruction in Cosmic-Ray Events”, *JINST* **5** (2010) T03022, `arXiv:0911.4994`.

[120] **CMS** Collaboration, “CMS physics: Technical design report”, 2006.

[121] **CMS** Collaboration, “Muon Reconstruction and Identification Improvements for Run-2 and First Results with 2015 Run Data”, tech. rep., Jul 2015. `https://cds.cern.ch/record/2037372`.

[122] **CMS** Collaboration, “*Performance of Electron Reconstruction and Selection with the CMS Detector in Proton-Proton Collisions at $\sqrt{s} = 8$ TeV*”, *JINST* **10** (2015), no. 06, P06005, `arXiv:1502.02701`, `http://dx.doi.org/10.1088/1748-0221/10/06/P06005`.

[123] W. Adam, R. Frühwirth, A. Strandlie, and T. Todorov, “Reconstruction of electrons with the gaussian-sum filter in the cms tracker at the lhc”, *Journal of Physics G: Nuclear and Particle Physics* **31** (2005), no. 9, N9, `"http://stacks.iop.org/0954-3899/31/i=9/a=N01"`.

[124] **CMS** Collaboration, “Electron reconstruction and identification at sqrt(s) = 7 TeV”, Tech. Rep. CMS-PAS-EGM-10-004, CERN, Geneva, 2010. `https://cds.cern.ch/record/1299116`.

[125] **CMS** Collaboration, “Electron and Photon performance using data collected by CMS at $\sqrt{s}$ = 13 TeV and 25ns”, tech. rep., Dec 2015. `https://cds.cern.ch/record/2118397`.

[126] M. Cacciari, G. P. Salam, and G. Soyez, “The Anti-k(t) jet clustering algorithm”, *JHEP* **04** (2008) 063, `arXiv:0802.1189`, `http://dx.doi.org/10.1088/1126-6708/2008/04/063`.

[127] **CMS** Collaboration, “Determination of Jet Energy Calibration and Transverse Momentum Resolution in CMS”, *JINST* **6** (2011) P11002, `arXiv:1107.4277`, `http://dx.doi.org/10.1088/1748-0221/6/11/P11002`.

[128] **CMS** Collaboration, “Performance of jets at CMS”, *J. Phys.: Conf. Ser.* **587** (2015), no. 1, 012004. 6 p, `https://cds.cern.ch/record/2158943`.

[129] **CMS** Collaboration, “Jet energy scale and resolution performances with 13TeV data”, tech. rep., Jun 2016. `https://cds.cern.ch/record/2160347`.

[130] **CMS** Collaboration, “Identification of b-quark jets with the cms experiment”, *Journal of Instrumentation* **8** (2013), no. 04, P04013, `http://stacks.iop.org/1748-0221/8/i=04/a=P04013`.

[131] **CMS** Collaboration, “Identification of b quark jets at the CMS Experiment in the LHC Run 2”, Tech. Rep. CMS-PAS-BTV-15-001, CERN, Geneva, 2016. `http://cds.cern.ch/record/2138504`.

[132] **CMS** Collaboration, “Performance of b tagging at sqrt(s)=8 TeV in multijet, ttbar and boosted topology events”, Tech. Rep. CMS-PAS-BTV-13-001, CERN, Geneva, 2013. `"http://cds.cern.ch/record/1581306"`.

[133] **CMS** Collaboration, “Performance of MET reconstruction and pileup mitigation techniques in CMS”, *Nucl. Part. Phys. Proc.* **273-275** (2016) 2512–2514, `arXiv:1502.05207`.

[134] **CMS** Collaboration, “Multivariate Determination of the Missing Energy in the Transverse Plane (E_T^{miss}) at $\sqrt{s} = 13$ TeV”, Aug 2015, `"http://cds.cern.ch/record/2048696"`.

[135] **CMS** Collaboration, “Search for the Production of Dark Matter in Association with Top Quark Pairs in the Di-lepton Final State in pp collisions at $\sqrt{s} = 8$ TeV”, Tech. Rep. CMS-PAS-B2G-13-004, CERN, Geneva, 2014. `"http://cds.cern.ch/record/1697173"`.

[136] “Search for dark matter in association with a top quark pair at $\sqrt{s} = 13$ TeV in the dilepton channel”, Tech. Rep. CMS-PAS-EXO-16-028, CERN, Geneva, 2016. `"https://cds.cern.ch/record/2226566"`.

[137] C. Oleari, “The powheg box”, *Nuclear Physics B - Proceedings Supplements* **205** (2010) 36 – 41, `"http://www.sciencedirect.com/science/article/pii/S0920563210001994"`.

[138] R. D. e. a. Ball, “Parton distributions for the LHC run II”, *Journal of High Energy Physics* **2015** (2015), no. 4, 40, `"http://dx.doi.org/10.1007/JHEP04(2015)040"`.

[139] T. Sjöstrand, S. Mrenna, and P. Skands, “A brief introduction to {PYTHIA} 8.1”, *Computer Physics Communications* **178** (2008), no. 11, 852 – 867, `"http://www.sciencedirect.com/science/article/pii/S0010465508000441"`.

[140] J. e. a. Alwall, “The automated computation of tree-level and next-to-leading order differential cross sections, and their matching to parton shower simulations”, *Journal of High Energy Physics* **2014** (2014), no. 7, 79, `"http://dx.doi.org/10.1007/JHEP07(2014)079"`.

[141] M. L. Mangano, M. Moretti, F. Piccinini, and M. Treccani, “Matching matrix elements and shower evolution for top-quark production in hadronic collisions”, *JHEP* **01** (2007) 013, `arXiv:hep-ph/0611129`.

[142] R. Frederix and S. Frixione, “Merging meets matching in MC@NLO”, *JHEP* **12** (2012) 061, `arXiv:1209.6215`.

[143] J. Pumplin, D. R. Stump, J. Huston, H. L. Lai, P. M. Nadolsky, and W. K. Tung, “New generation of parton distributions with uncertainties from global QCD analysis”, *JHEP* **07** (2002) 012, `arXiv:hep-ph/0201195`.

[144] **CMS** Collaboration, “Cms cross section measurements”. `https://twiki.cern.ch/twiki/pub/CMSPublic/PhysicsResultsCombined/SigmaNew_v0.pdf`.

[145] **CMS** Collaboration, S. Chatrchyan *et al.*, “Measurement of differential top-quark pair production cross sections in pp colisions at $\sqrt{s} = 7$ TeV”, *Eur. Phys. J.* **C73** (2013), no. 3, 2339, `arXiv:1211.2220`.

[146] **CMS** Collaboration, “Measurement of differential top-quark pair production cross sections in the lepton+jets channel in pp collisions at 8 TeV”, Tech. Rep. CMS-PAS-TOP-12-027, CERN, Geneva, 2013a. `"https://cds.cern.ch/record/1523611"`.

[147] **CMS** Collaboration, “Measurement of the differential ttbar cross section in the dilepton channel at 8 TeV”, Tech. Rep. CMS-PAS-TOP-12-028, CERN, Geneva, 2013b. `"https://cds.cern.ch/record/1523664"`.

[148] Y. Bai, H.-C. Cheng, J. Gallicchio, and J. Gu, “Stop the top background of the stop search”, *Journal of High Energy Physics* **2012** (2012), no. 7, 110, `"http://dx.doi.org/10.1007/JHEP07(2012)110"`.

[149] W. Verkerke and D. P. Kirkby, “The RooFit toolkit for data modeling”, *eConf* **C0303241** (2003) MOLT007, `arXiv:physics/0306116`, [,186(2003)].

[150] T. L. H. C. G. The ATLAS Collaboration, The CMS Collaboration, “Procedure for the LHC Higgs boson search combination in Summer 2011”, Tech. Rep. CMS-NOTE-2011-005. ATL-PHYS-PUB-2011-11, CERN, Geneva, Aug 2011. `"https://cds.cern.ch/record/1379837"`.

[151] J. S. Conway, “Incorporating Nuisance Parameters in Likelihoods for Multisource Spectra”, in “Proceedings, PHYSTAT 2011 Workshop on Statistical Issues Related to Discovery Claims in Search Experiments and Unfolding, CERN,Geneva, Switzerland 17-20 January 2011”, pp. 115–120. 2011. `arXiv:1103.0354`. `"https://inspirehep.net/record/891252/files/arXiv:1103.0354.pdf"`,

[152] **CMS** Collaboration, “CMS Luminosity Measurement for the 2015 Data Taking Period”, Tech. Rep. CMS-PAS-LUM-15-001, CERN, Geneva, 2016. `"https://cds.cern.ch/record/2138682"`.

[153] J. Butterworth *et al.*, “PDF4LHC recommendations for LHC Run II”, *J. Phys.* **G43** (2016) 023001, `arXiv:1510.03865`.

[154] **CMS** Collaboration, “Differential cross section measurements for the production of a W boson in association with jets in proton–proton collisions at $\sqrt{s} = 7$ TeV”, *Phys. Lett.* **B741** (2015) 12–37, `arXiv:1406.7533`.

[155] **CMS** Collaboration, S. Chatrchyan *et al.*, “Measurement of the production cross section for a W boson and two b jets in pp collisions at $\sqrt{s}$=7 TeV”, *Phys. Lett.* **B735** (2014) 204–225, `arXiv:1312.6608`.

[156] **CMS** Collaboration, “Measurements of jet multiplicity and differential production cross sections of $Z+$ jets events in proton-proton collisions at $\sqrt{s} = 7$ TeV”, *Phys. Rev.* **D91** (2015), no. 5, 052008, `arXiv:1408.3104`.

[157] **CMS** Collaboration, S. Chatrchyan *et al.*, “Measurement of the production cross sections for a Z boson and one or more b jets in pp collisions at sqrt(s) = 7 TeV”, *JHEP* **06** (2014) 120, `arXiv:1402.1521`.

[158] J. C. Collins, D. E. Soper, and G. F. Sterman, “Factorization of Hard Processes in QCD”, *Adv. Ser. Direct. High Energy Phys.* **5** (1989) 1–91, `arXiv:hep-ph/0409313`.

[159] J. e. a. Gao, “CT10 next-to-next-to-leading order global analysis of QCD”, *Phys. Rev.* **D89** (2014), no. 3, 033009, `arXiv:1302.6246`.

[160] A. D. Martin, W. J. Stirling, R. S. Thorne, and G. Watt, “Parton distributions for the LHC”, *Eur. Phys. J.* **C63** (2009) 189–285, `arXiv:0901.0002`.

[161] R. D. e. a. Ball, “Impact of Heavy Quark Masses on Parton Distributions and LHC Phenomenology”, *Nucl. Phys.* **B849** (2011) 296–363, `arXiv:1101.1300`.

[162] S. Alekhin *et al.*, “The PDF4LHC Working Group Interim Report”, `arXiv:1101.0536`.

[163] M. Botje *et al.*, “The PDF4LHC Working Group Interim Recommendations”, `arXiv:1101.0538`.

[164] G. Cowan, “Statistical data analysis”, Clarendon (Oxford), Oxford, 1998.

[165] T. M. Karbach and M. Schlupp, “Constraints on Yield Parameters in Extended Maximum Likelihood Fits”, `arXiv:1210.7141`.

[166] K. Cranmer, “Practical Statistics for the LHC”, in “Proceedings, 2011 European School of High-Energy Physics (ESHEP 2011): Cheile Gradistei, Romania, September 7-20, 2011”, pp. 267–308. 2015. `arXiv:1503.07622`. `"https://inspirehep.net/record/1356277/files/arXiv:1503.07622.pdf"`,

[167] G. Cowan, K. Cranmer, E. Gross, and O. Vitells, “Asymptotic formulae for likelihood-based tests of new physics”, *Eur. Phys. J.* **C71** (2011) 1554, `arXiv:1007.1727`.

[168] A. L. Read, “Presentation of search results: The CL(s) technique”, *J. Phys.* **G28** (2002) 2693–2704, [,11(2002)].

[169] R. S. Chivukula and H. Georgi, “Composite Technicolor Standard Model”, *Phys. Lett.* **B188** (1987) 99–104.

[170] L. J. Hall and L. Randall, “Weak-scale effective supersymmetry”, *Phys. Rev. Lett.* **65** Dec (1990) 2939–2942, `http://link.aps.org/doi/10.1103/PhysRevLett.65.2939`.

[171] A. J. Buras, P. Gambino, M. Gorbahn, S. Jager, and L. Silvestrini, “Universal unitarity triangle and physics beyond the standard model”, *Phys. Lett.* **B500** (2001) 161–167, `arXiv:hep-ph/0007085`.

[172] G. D’Ambrosio, G. F. Giudice, G. Isidori, and A. Strumia, “Minimal flavor violation: An Effective field theory approach”, *Nucl. Phys.* **B645** (2002) 155–187, `arXiv:hep-ph/0207036`.

[173] T. Lin, E. W. Kolb, and L.-T. Wang, “Probing dark matter couplings to top and bottom quarks at the LHC”, *Phys. Rev.* **D88** (2013), no. 6, 063510, `arXiv:1303.6638`.

[174] M. Beltran, D. Hooper, E. W. Kolb, Z. A. C. Krusberg, and T. M. P. Tait, “Maverick dark matter at colliders”, *JHEP* **09** (2010) 037, `arXiv:1002.4137`.

[175] G. Busoni, A. De Simone, E. Morgante, and A. Riotto, “On the Validity of the Effective Field Theory for Dark Matter Searches at the LHC”, *Phys. Lett.* **B728** (2014) 412–421, `arXiv:1307.2253`.

[176] O. Buchmueller, M. J. Dolan, and C. McCabe, “Beyond Effective Field Theory for Dark Matter Searches at the LHC”, *JHEP* **01** (2014) 025, `arXiv:1308.6799`.

[177] M. R. Buckley, D. Feld, and D. Goncalves, “Scalar Simplified Models for Dark Matter”, *Phys. Rev.* **D91** (2015) 015017, `arXiv:1410.6497`.

[178] **SuperCDMS** Collaboration, R. Agnese *et al.*, “Search for Low-Mass Weakly Interacting Massive Particles Using Voltage-Assisted Calorimetric Ionization Detection in the SuperCDMS Experiment”, *Phys. Rev. Lett.* **112** (2014), no. 4, 041302, `arXiv:1309.3259`.

[179] **LUX** Collaboration, D. S. Akerib *et al.*, “First results from the LUX dark matter experiment at the Sanford Underground Research Facility”, *Phys. Rev. Lett.* **112** (2014) 091303, `arXiv:1310.8214`.

[180] **XENON100** Collaboration, E. Aprile *et al.*, “Dark Matter Results from 225 Live Days of XENON100 Data”, *Phys. Rev. Lett.* **109** (2012) 181301, `arXiv:1207.5988`.

[181] **SuperCDMS** Collaboration, R. Agnese *et al.*, “Search for Low-Mass Weakly Interacting Massive Particles with SuperCDMS”, *Phys. Rev. Lett.* **112** (2014), no. 24, 241302, `arXiv:1402.7137`.

[182] **CRESST-II** Collaboration, G. Angloher *et al.*, “Results on low mass WIMPs using an upgraded CRESST-II detector”, *Eur. Phys. J.* **C74** (2014), no. 12, 3184, `arXiv:1407.3146`.

[183] **CMS** Collaboration, “Search for Monotop Signatures in Proton-Proton Collisions at $\sqrt{s} = 8$ TeV”, *Phys. Rev. Lett.* **114** (2015), no. 10, 101801, `arXiv:1410.1149`.

[184] **CMS** Collaboration, “Search for monotop in the muon channel in proton-proton collisions at $\sqrt{s} = 8$ TeV”, Tech. Rep. CMS-PAS-B2G-15-001, CERN, Geneva, 2016a. `"https://cds.cern.ch/record/2143260"`.

[185] **CMS** Collaboration, “Search for dark matter in association with a boosted top quark in the all hadronic final state”, Tech. Rep. CMS-PAS-EXO-16-017, CERN, Geneva, 2016b. `"http://cds.cern.ch/record/2160266"`.

[186] **DELPHES 3** Collaboration, J. de Favereau, C. Delaere, P. Demin, A. Giammanco, V. Lemaître, A. Mertens, and M. Selvaggi, “DELPHES 3, A modular framework for fast simulation of a generic collider experiment”, *JHEP* **02** (2014) 057, `arXiv:1307.6346`.

Curriculum Vitae

Personal Information

Name	Deborah Pinna
Date of Birth	23.07.1984
Place of Birth	Oristano, Italy
Nationality	Italian
Email Address	deborah.pinna@outlook.com

Education

Since May 2013	**Employed as PhD student**, at University of Zurich (UZH)
Sept. 2012 - April 2013	**Assistant (Hilfsassistent)** at ETH Zurich (Institute for Particle Physics IPP)
Feb. 2012 - Aug. 2012	**Exchange student** at ETH Zurich (Institute for Particle Physics IPP) for Master Thesis
June - Sept. 2012	**Summer Student** at European Organisation for Nuclear Research (CERN), Geneva Study of possible improvements of LHCb simulation using different Physics lists, LHCb experiment
2008 - 2012	**Master degree in Physics**, at University of Cagliari Thesis: Study of ZZ diboson production with CMS detector at $\sqrt{s} = 7$ TeV and 5fb^{-1} luminosity
2003 - 2008	**Bachelor degree in Physics**, at University of Cagliari Thesis: Molteplicita' di particelle cariche in collisioni In-In all' SPS del CERN

July 2001 - Aug. 2002	**Exchange student** in Jamaica with AFS Organization program: attending the 4th year of high school in a Jamaican school and living with a local host family
Sept. 1998 - June 2003	**Scientific-Technological high school degree**, Istituto Tecnico Industriale OTHOCA Oristano